Nuclear Medicine Review 2022, Vol. 25, No. 2, pages 73–148

Nuclear Medicine

R · E · V · I · E · W

merged with Problems of Nuclear Medicine

MEiN: 40 pkt

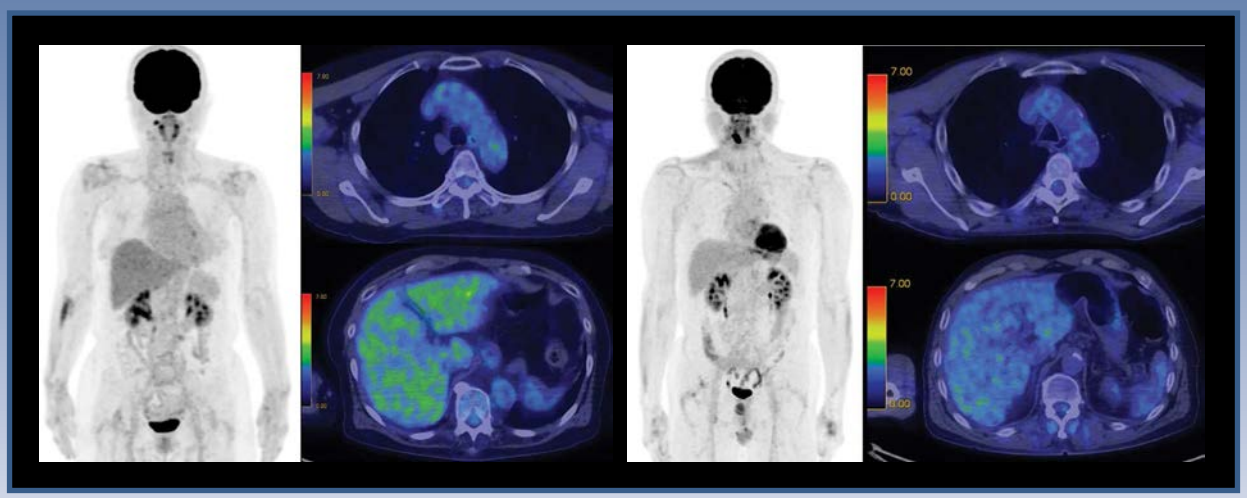

See page 98

ISSN 1506–9680

2022, Volume 25, Number 2

e-ISSN 1644–4345

Journal of Polish, Serbian, Hungarian, Bulgarian and Macedonian Societies of Nuclear Medicine

VIA MEDICA

www.journals.viamedica.pl/nuclear_medicine_review

Nuclear Medicine
R · E · V · I · E · W

merged with ***Problems of Nuclear Medicine****

Editorial Office

Wojskowy Instytut Medyczny
ul. Szaserów 128, 04–141 Warszawa
e-mail: nmr@viamedica.pl

Managing Editor

M. Nehrebecka (Gdańsk, Poland)

*Following the agreement concluded on 23 February 2011 between the Polish Society of Nuclear Medicine and Via Medica Sp. z o.o. the journal „Nuclear Medicine Review" has merged with „Problemy Medycyny Nuklearnej", a journal published since 1987.

Nuclear Medicine Review (ISSN 1506–9680, e-ISSN 1644–4345) is published twice a year by VM Media sp. z o.o., VM Group sp. k., Grupa Via Medica
ul. Świętokrzyska 73, 80–180 Gdańsk, Poland
tel: (+48 58) 320 94 94, fax: (+48 58) 320 94 60; e-mail: redakcja@viamedica.pl, marketing@viamedica.pl
http://www.viamedica.pl

Advertising: For details on media opportunities within this journal please contact the advertising sales department, ul. Świętokrzyska 73, 80–180 Gdańsk, Poland
tel: (+48 58) 320 94 94, e-mail: marketing@viamedica.pl

The Editors accept no responsibility for the advertisement contents.

Single issues requests should be send to e-mail: prenumerata@viamedica.pl. Electronic orders option available at: www.nmr.viamedica.pl

Indexation: Crossref, DOAJ (Directory of Open Access Journals), EMBASE, ESCI (Emerging Sources Citation Index), Index Copernicus (100.00), MEDLINE, Polish Medical Bibliography, Ministry of Science and Higher Education (40), Scopus, Ulrich's Periodicals Directory.

Editorial policies and author guidelines are published on journal website: www.journals.viamedica.pl/nuclear_medicine_review

Nuclear Medicine
R · E · V · I · E · W

merged with ***Problems of Nuclear Medicine****

2022, Volume 25, Number 2

Editorial V

Original articles

İlknur Kucukosmanoglu, Meryem Ilkay Eren Karanis, Yasar Unlu, Mustafa Erol
Correlation of [^{18}F]FDG PET activity with expressions of Ki-67 in non-small-cell lung cancer 73

Francesco Dondi, Domenico Albano, Francesco Bertagna, Raffaele Giubbini
[^{18}F]FDG PET/CT and CA-125 in the evaluation of ovarian cancer relapse or persistence: is there any correlation? 78

Shoaa G. Shetewi, Jaber Alyami, Bander S. Al Mutairi, Saeed M. Bafaraj
Sensitivity and specificity of nuclear medicines (DTPA and DMSA) with magnetic resonance imaging in diagnosing bone metastasis 85

Kate Hunter, Niamh Gavin, Colin McQuade, Brendan Hogan, John Feeney
Optimal timing of SPECT/CT to demonstrate parathyroid adenomas in ^{99m}Tc-sestamibi scintigraphy 89

Yoichi Otomi, Yuta Arai, Maki Otomo, Saho Irahara, Kaori Terazawa, Michiko Kubo, Takashi Abe, Takayoshi Shinya, Hideki Otsuka, Masafumi Harada
Increased physiological [^{18}F]FDG uptake in the liver and blood pool among patients with impaired renal function 95

Anamarija Jankulovska, Bojana Stoilovska Rizova, Nikolina Bozhinovska, Aleksandra Peshevska, Mile Tanturovski, Igor Aluloski, Sasho Stojcevski, Nevena Manevska, Sinisa Stojanoski, Daniela Miladinova
Preoperative detection of sentinel lymph node in patients with endometrial cancer — comparison of planar lymphoscintigraphy, spect and SPECT/CT 101

Sofia Markoula, Afroditi Tsoumani, Chainti Antonella Votti, Maria Beltsiou, Lampros Lakkas, Konstantinos Pappas, Ioannis Iakovou, Andreas Fotopoulos, Athanassios P Kyritsis, Chrissa Sioka
Myocardial perfusion imaging single photon emission computed tomography may detect silent myocardial ischemia in patient with epilepsy 105

Ahmed M. Shalash, Mai Amr ELahmadawy, Samia Y. Heikal, Ayman A. Amin, Ayda A. Youssef
Value of diffusion MRI versus [^{18}F]FDG PET/CT in detection of cervical nodal metastases in differentiated thyroid cancer patients 112

Review

Sonia J. Konsek-Komorowska, Mariola Peczkowska, Jaroslaw B. Cwikła
Myocardial perfusion imaging using single-photon emission computed tomography with cadmium-zinc-telluride technology 119

Clinical vignettes

Haluk B. Sayman, Kubra N. Toplutas, James Tunick, Omer Aras
^{99m}Tc-Vitamin C SPECT/CT imaging in SARS-CoV-2 associated pneumonia 127

Omer Aras, Cetin Demirdag, Harikrishna Kommidi, Richard Ting, Haluk B. Sayman
Radiopharmaceutical for detecting PSMA — positive metastatic colon cancer: Matched-pair comparison of ^{18}F-BF3-Cy3-ACUPA and ^{68}Ga-PSMA PET/MRI 129

Somaye Barashki, Hadis Mohammadzadeh Kosari, Emran Askari, Zahra Bakhshi Golestani, Mehran Hiradfar, Ramin Sadeghi
A crying liver: a scan pattern mimicking spontaneous perforation of the biliary ducts 131

Mehrosadat Alavi, Yalda Moafpourian
COVID-19 pneumonia detected by parathyroid scintigraphy 134

Ghasemali Divband, Seyed Hootan Alavi, Zohre Adinehpour, Forough Kalantari, Soroush Zarehparvar Moghadam
Amino acid extravasation: a rare red flag to keep in mind during peptide receptor radioligand therapy (PRRT) with [^{177}Lu]Lu-DOTATATE 136

Letters to Editor

Evanthia Giannoula, Christos Melidis, Nikitas Papadopoulos, Panagiotis Bamidis, Vasilios Raftopoulos, Vasiliki Chatzipavlidou, Ioannis Iakovou
A 4.000 € way to improve perceived quality and meet expectations of thyroid cancer patients receiving therapeutic dose of Iodine-131 138

Joseph C. Lee, Alaa Alghamry
Multiple benefits of added attenuation correction computed tomography for myocardial perfusion imaging in patients with psoriasis 141

Experts' opinion

Katarzyna Holcman, Miroslaw Dziuk, Jacek Grzybowski, Anna Teresinska, Bogdan Malkowski, Diana Jedrzejuk, Bogna Brockhuis, Rafal Czepczynski, Lidia Tomkiewicz-Pajak, Magdalena Kostkiewicz
The scintigraphic diagnosis of cardiac amyloidosis. An expert opinion endorsed by the Section of Nuclear Medicine of the Polish Cardiac Society and the Polish Nuclear Medicine Society 142

VIA MEDICA

Nuclear Medicine Review 2022, 25, 2: V
DOI: 10.5603/NMR.2022.0016

ISSN 1506–9680, e-ISSN 1644–4345

Editorial

Dear Sirs and Madams,

I would like to announce the "hot summer 2022" issue of "Nuclear Medicine Review". We live in difficult times: not so far from us the terrible Russian-Ukrainian war is going on, there are heat waves and fires all over Europe and the new variants of SARS-CoV-2 still arise. We must be strong and united. To get to the point, the chapter "Original articles" consists of eight interesting papers. It opens with an article written by Turkish colleagues concerning correlation of [^{18}F] FDG PET activity with expressions of Ki-67 in non-small-cell lung cancer. The next paper, from Italy, finds the correlations between [^{18}F]FDG PET/CT and CA-125 in the evaluation of ovarian cancer relapse or persistence. Scientists from Saudi Arabia have focused on sensitivity and specificity of nuclear medicines (DTPA and DMSA) with magnetic resonance imaging in diagnosing bone metastasis in the third paper. The next one — from Ireland — shows that single late phase SPECT/CT is significantly superior to early SPECT/CT in the identification of parathyroid adenomas. It seems that early SPECT/CT acquisition can be eliminated from scan protocols. In the next paper Japanese scientists discovered increased physiological [^{18}F]FDG uptake in the liver and blood pool among patients with impaired renal function. An article considering comparison of planar lymphoscintigraphy, SPECT, and SPECT/CT in preoperative detection of sentinel lymph node in patients with endometrial cancer by authors from North Macedonia shows superiority of SPECT/CT technic. In the next paper Greek colleagues conclude that epileptic patients with atypical cardiac symptoms are at higher risk for cardiovascular disease and the myocardial perfusion imaging with [^{99m}Tc] tetrofosmin stress — rest single photon emission computer tomography may be utilized to assess even asymptomatic yet myocardial ischemia in patients with epilepsy for early intervention and reduction of sudden cardiac death. Finally from Egypt evaluate diffusion MRI versus FDG PET/CT in detection of cervical nodal metastases in patients with differentiated thyroid cancer. In the next paper we have got a review considering myocardial perfusion imaging using single-photon emission computed tomography with cadmium-zinc-telluride technology. Clinical vignette consists of five very interesting cases from Turkey, the United States and Iran. Also, there are two letters to the editor and in the end the opinion of Polish experts about scintigraphic diagnosis of cardiac amyloidosis.

Dear colleagues, looking for the better future and enjoy reading our journal!

Yours,
Grzegorz Kamiński

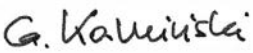

Editor-in-Chief
Nuclear Medicine Review

VIA MEDICA

Nuclear Medicine Review 2022, 25, 2: 73–77
DOI: 10.5603/NMR.a2022.0017

ISSN 1506–9680, e-ISSN 1644–4345

Original

Correlation of [^{18}F]FDG PET activity with expressions of Ki-67 in non-small-cell lung cancer

Ilknur Kucukosmanoglu[1], Meryem Ilkay Eren Karanis[1], Yasar Unlu[1], Mustafa Erol[2]

[1]Department of Pathology, Konya City Hospital, Konya, Turkey
[2]Department of Nuclear medicine, Konya City Hospital, Konya, Turkey

[Received 24 I 2021; Accepted 27 IV 2022]

Abstract

Background: Lung carcinoma is the most commonly diagnosed cancer throughout the world and is the leading cause of cancer-related deaths. Non-small cell lung cancer (NSCLC) accounts for up to 80% of newly diagnosed lung cancer cases. This study aimed to investigate the relationship between Ki-67 proliferation index (PI) and the maximum standardized uptake value (SUVmax) obtained from [^{18}F]FDG PET/CT in NSCLCs and whether prognosis was predicted with SUVmax values.

Material and methods: This retrospective study included biopsy and resection materials of 41 patients, who were examined in the pathology laboratory of Konya Training and Research Hospital between January 2010 and December 2019, and diagnosed with NSCLC, and whose [^{18}F]FDG PET/CT images were present.

Results: There was no significant difference between histopathological subtypes in terms of age ($p = 0.077$), Ki-67 PI ($p = 0.454$), and SUVmax ($p = 0.143$). No correlation was observed between Ki-67 PI and SUVmax values obtained from [^{18}F]FDG PET/CT ($p = 0.338$, $r = 0.153$). There was no significant correlation between Ki-67 PI and tumor diameter ($p = 0.531$). The SUVmax value was found to be lower (12.78 ± 6.14) in tumors measuring ≤ 2.5 in diameter and higher (18.46 ± 7.81) in tumors measuring > 2.5 cm ($p = 0.027$). Metastases not proven histopathologically but detected in [^{18}F]FDG PET/CT were found to have no significant correlation with Ki-67 and SUVmax values ($p = 0.881$, $p = 0.837$).

Conclusions: This study showed that there was no significant relationship between Ki-67 PI and SUVmax value obtained from [^{18}F]FDG PET/CT in NSCLC tumors.

KEY words: non-small cell lung cancer; Ki-67; PET/CT

Nucl Med Rev 2022; 25, 2: 73–77

Introduction

Lung carcinoma is the most commonly diagnosed cancer throughout the world and is the leading cause of cancer-related deaths. NSCLC accounts for up to 80% of newly diagnosed lung cancer cases [1–4]. Adenocarcinoma (AC) and squamous cell carcinoma (SCC) are two main histological subtypes of NSCLC. Compared to AC, SCC has a more destructive growth pattern and is associated with lower overall survival rates [3, 5]. The most important prognostic determinant is the stage of cancer at the time of diagnosis. Therefore, it is important to determine the extent of the disease, *i.e.*, staging at the time of diagnosis, for determining the most suitable treatment option and obtaining prognostic information in patients with newly diagnosed NSCLC. In particular, it is of great importance to accurately distinguish patients with potentially curable early-stage cancer, who may benefit from radical surgery, from those who are deemed to be non-operable and therefore addressed to chemotherapy, radiotherapy, or both [6]. Uptake of fluorine-18-fluorodeoxyglucose ([^{18}F]FDG) measured by integrated positron emission tomography/computed tomography (PET/CT) is a widely used non-invasive diagnostic test. Functional abnormalities can be detected by PET, even before they become morphologically apparent in conventional imaging. Moreover, PET imaging is also utilized for detecting fibrosis, the presence of edema, and viable tumor cells after treatment. The most commonly employed tracer for the evaluation of lung cancer is [^{18}F]FDG [4, 6, 7]. The [^{18}F]FDG PET/CT measures the SUV of a pulmonary nodule, *i.e.*, the glucose avidity of the tumor. The [^{18}F]FDG PET/CT

Correspondence to: Ilknur Kucukosmanoglu, Department of Pathology, Konya City Hospital, 42020 Akabe, Karatay, Konya, Turkey
e-mail: ilknurkukrer@hotmail.com

imaging is known to be useful in (i) determining the clinical behavior of a pulmonary nodule with an uncertain histopathological diagnosis and (ii) demonstrating mediastinal lymph node metastasis and distant metastasis [1]. Uptake of [^{18}F]FDG is associated with the proliferative activity of the tumor in lung cancers and is an independent prognostic factor [8]. Glucose metabolism in cancer tissues measured by [^{18}F]FDG PET/CT is an important biomarker for the characterization of lung cancer. Special care is recommended when using PET/CT in the investigation of patients with diabetes and in possible inflammatory processes [4]. Despite recent advances in personalized medicine, lung cancer still has a poor prognosis. Analyses of the predictive biomarkers are important to maximize the benefit of treatment [2, 3, 9].

Evaluation of tumor proliferation as a morphology-based measure of tumor growth kinetics has a long-standing background. The PI analysis of the Ki-67 antigen, one of the proliferation-related antigens, is frequently used for this purpose. Ki-67 was first developed by Gerdes et al. [10] in 1983. Ki-67 is a DNA-binding nuclear protein that proliferates throughout the cell cycle but is not expressed in quiescent (G0) cells [2, 11, 12]. It is a well-known powerful biomarker with significant prognostic value in breast cancers, gastrointestinal system tumors, and neuroendocrine tumors [2]. Tumor cell proliferation comprehensively describes the aggression and biological behavior of a tumor, which may provide additional tips for treatment selection. Meta-analyses of numerous studies on resected early-stage NSCLC suggest that high Ki-67 values are associated with poor prognosis, shorter disease-free survival, and shorter recurrence-free survival [2, 4, 13]. However, the Ki-67 assessment in NSCLC has not been successfully included in routine reporting yet. Several studies reported a correlation between FDG uptake and Ki-67 proliferation in lymphomas, head and neck tumors, and NSCLC [9]. This study aimed to investigate the correlation between the Ki-67 proliferation index (PI) and SUVmax values obtained from [^{18}F]FDG PET/CT in NSCLC cases.

Material and methods

This retrospective study included biopsy and resection materials of 41 patients (38 males and 3 females), who were examined in the pathology laboratory of Konya Training and Research Hospital between January 2010 and December 2019, and diagnosed with NSCLC, and whose [^{18}F]FDG PET/CT images were present. Age, gender, treatment, and other information were obtained from hospital records. Formalin-fixed paraffin-embedded (FFPE) tissue specimens were used in the study. Five-micron-thick sections obtained from the paraffin blocks were stained with hematoxylin and eosin (H&E). These H&E stained preparations taken from the archive were re-examined under a light microscope by a single pathologist to confirm the diagnoses. Ki-67 immunohistochemical (IHC) staining preparations (clone: MIB-1) of these cases were also present. Ki-67 PI of the cases was re-calculated by the same pathologist. During the evaluation, the area of most intense staining (hot spot) was identified at small magnification. In the area of most intense staining, 500 tumor cells were counted at high magnification (x400) and positive-stained cells were expressed as a percentage (Fig.1). All patients with pulmonary nodules identified by imaging methods underwent [^{18}F]FDG PET/CT for diagnosis or staging within 10 days before the biopsy. These [^{18}F]FDG PET/CT scans were blindly re-evaluated by an experienced nuclear medicine specialist. The protocol was as follows: A fasting condition for at least six hours and prohibition of intravenous glucose infusion was applied before [^{18}F]FDG injection. Blood glucose levels were measured using a fingerstick blood sugar test and confirmed to be 180 mg/dL before [^{18}F]FDG injection. The PET/CT scan was performed 60 minutes after intravenous injection of 0.12 mCi/kg [^{18}F]FDG. Then, PET scans were then taken at seven to eight-bed positions and at two-minute intervals for each position. During the PET/CT scan, all patients were in the supine position. Non-contrast CT scanning began at the orbitomeatal line and progressed to the upper thigh (30 mAs, 130 kV, 5 mm slice thickness), and PET imaging followed immediately over the same body region. The CT data were used for attenuation correction and anatomical localization of the lesions. PET/CT fusion images were obtained in transaxial, sagittal, and coronal planes. SUVmax of the lesions was obtained from transaxial images (Fig. 2).

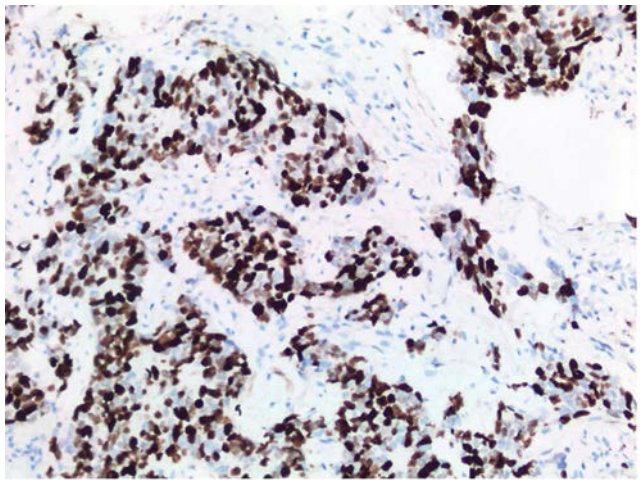

Figure 1. Ki-67 immunohistochemical staining, x 200 magnification (proliferation index: 75%)

The statistical analyses were performed using SPSS 15.0 for Windows (SPSS, Chicago, IL, USA). The Shapiro-Wilk test was used for examining the continuous variables with normal and abnormal distributions, while the one-way analysis of variance (ANOVA) was used for the normally distributed continuous variables. The Kruskal-Wallis test was used for the abnormally distributed continuous variables. When the Kruskal-Wallis test indicated statistically significant differences, the causes of those differences were determined using a Bonferroni-adjusted Mann-Whitney U test. The continuous variables were presented as the mean ± standard deviation (SD). For all possible multiple comparisons, the Bonferroni adjustment was performed to control the type I errors. The Spearman correlation analysis was used to study the correlations between measurements. Statistical significance was considered at $p < 0.05$.

Approval was obtained from the ethics committee of KTO Karatay University for the study.

Results

The diagnosis was SCC in six (14.6%) of the cases, AC in 21 (51.2%), and NSCLC-not otherwise specified (NOS) in 14 (34.1%).

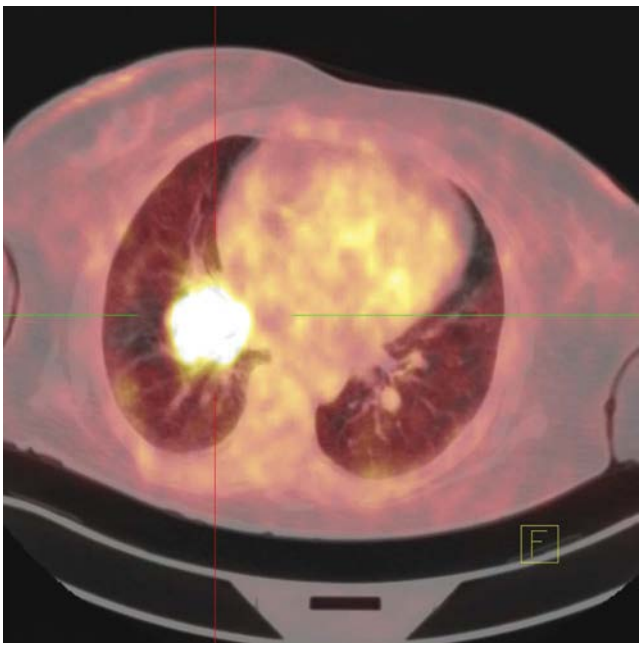

Figure 2. An [^{18}F]FDG PET/CT image of a patient with adenocarcinoma (SUVmax: 14.52)

The mean age was 60.19 ± 10.66 years in AC cases, 61.79 ± 8.11 years in NSCLC-NOS cases, and 69.33 ± 10.09 years in SCC cases. The mean Ki-67 PI was 33.86 ± 20.67 in AC, 49.57 ± 20.82 in NSCLC-NOS, and 34.00 ± 17.15 in SCC. The mean SUVmax value was 15.20 ± 6.34 in ACs, 17.85 ± 9.12 in NSCLC-NOS, and 18.99 ± 8.99 in SCC (Tab. 1). There was no significant difference between histopathological subtypes in terms of age, Ki-67 PI, and SUVmax.

No correlation was found between Ki-67 PI, and SUVmax values obtained from [^{18}F]FDG PET/CT ($p = 0.338$, $r = 0.153$). The cutoff values for Ki-67 PI were determined as ≤ 10, 10–25, and ≥ 25. Similarly, there was no correlation with SUVmax ($p = 0.230$). There was no significant correlation between Ki-67 PI and tumor diameter ($p = 0.531$). The SUVmax value was found to be lower in tumors measuring ≤ 2.5 in diameter and higher in tumors measuring > 2.5 cm ($p = 0.027$) (Tab. 2).

Metastases not proven histopathologically but detected in [^{18}F]FDG PET/CT were found to have no significant correlation with Ki-67 and SUVmax values ($p = 0.881$, $p = 0.837$) (Tab.3).

Conclusions

In recent years, PET/CT has become a routinely used procedure for the assessment of lung cancer. Many studies suggested that [^{18}F]FDG PET/CT was superior to CT in terms of the accuracy of nodal (N) staging for lung cancer. Therefore, [^{18}F]FDG PET/CT is currently recognized as the most accurate imaging method for N staging of lung cancer. Nonetheless, there are also studies reporting that [^{18}F]FDG PET/CT gives false negative and false positive findings in lung cancer cases, including N staging.

In a retrospective analysis involving solid lung masses, a positive correlation was found between the size of a malignant tumor and SUVmax. Multivariate analysis demonstrated that the combination of high SUV and large lesion size describes a subgroup of patients with the poorest prognosis and a median survival rate of fewer than six months [1].

The most widely used tracer for the detection of lung cancer is [^{18}F]FDG, which provides valuable information for patient management, particularly for detecting nodal and metastatic involvement and evaluating response to treatment. Misleading data may be encountered while utilizing [^{18}F]FDG PET/CT in

Table 1. Relationship between histopathological type ,and SUVmax, Ki-67 and age

	AC (n = 21)	NSCLC, NOS (n = 14)	SCC (n = 6)	p-value
Age	60.19 ± 10.66	61.79 ± 8.11	69.33 ± 10.09	0.077
Ki-67 PI	33.86 ± 20.67	49.57 ± 20.82	34.00 ± 17.15	0.454
SUVmax	15.20 ± 6.34	17.85 ± 9.12	18.99 ± 8.99	0.143

AC — adenocarcinoma; NOS — not otherwise specified; NSCLC — non-small cell lung cancer; PI — proliferation index; SCC — squamous cell carcinoma; SUVmax — maximum standardized uptake value

Table 2. Relationship between diameter and SUVmax, Ki-67

	≤ 2.5 cm (n = 13)	> 2.5 cm (n = 28)	p-value
Ki-67 PI	36 ± 22.74	40.68 ± 20.66	0.531
SUVmax	12.78 ± 6.14	18.46 ± 7.81	0.027

PI — proliferation index; SUVmax — maximum standardized uptake value

Table 3. Relationship between metastasis and SUVmax, Ki-67

	Metastasis present	Metastasis absent	p-value
Ki-67 PI	39.67 ± 19.96	38.65 ± 23.38	0.881
SUVmax	16.87 ± 7.29	16.36 ± 8.52	0.837

PI — proliferation index; SUVmax — maximum standardized uptake value

the assessment of brain metastasis (due to high physiological [^{18}F]FDG uptake in the brain), tumor types characterized by low glucose intake (neuroendocrine tumors, lepidic pattern adenocarcinomas), and cases with concomitant inflammation (due to high FDG uptake of inflammatory cells). In recent years, new PET tracers have been designed to overcome these limitations and have been successfully used in cases with suspected secondary brain lesions. The information provided by PET/CT is valuable in the clinical management of patients with lung cancer [6].

Several studies have demonstrated that SUV can reflect different histopathological parameters in lung cancer and has a moderate correlation with Ki-67. This is not a surprising finding. Ki-67, which is a non-histone nuclear protein and is synthesized throughout the entire cell cycle, except the G0 phase, is responsible for cell proliferation. It is an established biomarker in lung cancer for predicting tumor behavior. Theoretically, SUV reflects metabolic activity and can therefore be associated with various proliferation biomarkers. On the other hand, metabolic activity has no direct correlation with proliferation since FDG is not a specific tracer of cellular proliferation [5, 13]. The PET parameters can also be used as biomarkers if they correlate with various histopathological findings that reflect the proliferation or other features of lung cancer. Pretreatment SUV is often used as a relative measure of [^{18}F]FDG uptake and is accepted as a prognostic factor for risk stratification in different malignancies; however, it does not reflect the heterogeneity of a tumor. Therefore, other PET parameters including metabolic tumor volume (MTV) and total lesion glycolysis (TLG) reflecting metabolic volume and activity have been proposed as quantitative indices of tumor metabolism to eliminate this disadvantage of SUVmax. There is a need for further studies to identify any possible correlation between various PET parameters and histopathology in lung cancer [13].

Studies are demonstrating a positive correlation between Ki-67 PI and FDG uptake; however, the correlation was reported to be weak in these studies. On the other hand, a threshold value was determined for Ki-67 PI by authors who reported that there was a weak correlation between FDG uptake values and tumor cell proliferation. According to Spyratos et al. [14], the choice of cut-off depends on the clinical objective: if Ki-67 is used to exclude patients with slowly proliferating tumors from chemotherapeutic protocols, a cut-off value of 10% will help to avoid overtreatment. In contrast, if Ki-67 is used to identify patients sensitive to chemotherapy protocols, it is preferable to set the cut-off at 25% [5]. In conclusion, an optimal threshold still needs to be defined for Ki-67 PI and validated for lung cancer. Among studies published after 2000, no consensus seems to be present on the prognostic value of Ki-67 PI in neither univariate nor multivariate analyses. The reason for conflicting results from the studies may be attributed to the fact that different variables that may influence the prognostic effect of Ki-67 are included in the studies. Although many studies have shown the negative prognostic effect of high Ki-67, most of these studies are of retrospective design and involve heterogeneous patient groups receiving incomparable treatments and follow-ups [12].

Information related to cell proliferation can also be useful in understanding tumor behavior in addition to the histological classification of tumors. Proliferative activity was found to have a significant correlation with metastatic potential, recurrence, or general prognosis in lung cancer [15]. Standardization is required for IHC, particularly regarding the positivity threshold, to become a useful prognostic factor in clinical practice. Furthermore, the present findings should be confirmed by taking into account classical well-defined prognostic factors for survival in patients with lung cancer [11]. Whether Ki-67 PI and SUVmax values were prognostic biomarkers was investigated separately in previous studies whereas this study assessed Ki-67 and SUVmax values together and investigated the correlation between them. The literature review showed that several studies reported high Ki-67 PI as a poor prognostic parameter in lung cancers whereas there were also studies reporting that high FDG uptake was associated with the proliferative activity of the tumor and could be used as a poor prognostic parameter.

We believe that information on the Ki-67 biomarker indicating the proliferative activity of the tumor can be predicted by the FDG uptake of the tumor. However, correlation analysis revealed no correlation between these two parameters. There were speculations that the cut-off value for KI-67 PI was chosen to affect the p-value in several studies. According to the statistical analyses we performed for Ki-67 both without determining any cut-off value and determining a cut-off value, there was no significant correlation between the two parameters in both cases.

This study has several limitations. Firstly, it was conducted in a single hospital, with a small number of cases. Therefore, the results may not be representative of larger populations. Moreover, since the SUVmax value does not reflect the heterogeneity of a tumor, comparing other PET parameters such as MTV and TLG, which reflects metabolic volume and activity, with Ki-67 PI in future studies may be helpful to eliminate this disadvantage of SUVmax. Therefore, conducting similar prospective studies including a larger number of patients with more homogeneous distribution (such as near tumor diameter) may shed light on this issue.

Conflict of interest

The authors have no conflicts of interest to declare.

References

1. Ozgül MA, Kirkil G, Seyhan EC, et al. The maximum standardized FDG uptake on PET-CT in patients with non-small cell lung cancer. Multidiscip Respir Med. 2013; 8(1): 69, doi: 10.1186/2049-6958-8-69, indexed in Pubmed: 24148271.
2. Warth A, Cortis J, Soltermann A, et al. Tumour cell proliferation (Ki-67) in non-small cell lung cancer: a critical reappraisal of its prognostic role. Br J Cancer. 2014; 111(6): 1222–1229, doi: 10.1038/bjc.2014.402, indexed in Pubmed: 25051406.
3. Sauter AW, Winterstein S, Spira D, et al. Multifunctional Profiling of Non–Small Cell Lung Cancer Using 18F-FDG PET/CT and Volume Perfusion CT. J Nucl Med. 2012; 53(4): 521–529, doi: 10.2967/jnumed.111.097865, indexed in Pubmed: 22414637.
4. Hochhegger B, Alves GR, Irion KL, et al. PET/CT imaging in lung cancer: indications and findings. J Bras Pneumol. 2015; 41(3): 264–274, doi: 10.1590/S1806-37132015000004479, indexed in Pubmed: 26176525.
5. Vesselle H, Salskov A, Turcotte E, et al. Relationship between non-small cell lung cancer FDG uptake at PET, tumor histology, and Ki-67 proliferation index. J Thorac Oncol. 2008; 3(9): 971–978, doi: 10.1097/JTO.0b013e31818307a7, indexed in Pubmed: 18758298.

6. Ambrosini V, Nicolini S, Caroli P, et al. PET/CT imaging in different types of lung cancer: an overview. Eur J Radiol. 2012; 81(5): 988–1001, doi: 10.1016/j.ejrad.2011.03.020, indexed in Pubmed: 21458181.
7. Ma W, Wang M, Li X, et al. Quantitative F-FDG PET analysis in survival rate prediction of patients with non-small cell lung cancer. Oncol Lett. 2018; 16(4): 4129–4136, doi: 10.3892/ol.2018.9166, indexed in Pubmed: 30214552.
8. Chirieac LR. Ki-67 expression in pulmonary tumors. Transl Lung Cancer Res. 2016; 5(5): 547–551, doi: 10.21037/tlcr.2016.10.13, indexed in Pubmed: 27827465.
9. Bedir R, Yusufoğlu B, Bilir C, et al. Relationship Between The [18F]FDG Uptake with Ki-67 and P53 Expression in Patients with Lung Cancer: A Clino-Pathologic Study. J hum rhythm. 2016; 2(3): 126–33.
10. Gerdes J, Schwab U, Lemke H, et al. Production of a mouse monoclonal antibody reactive with a human nuclear antigen associated with cell proliferation. Int J Cancer. 1983; 31(1): 13–20, doi: 10.1002/ijc.2910310104, indexed in Pubmed: 6339421.
11. Martin B, Paesmans M, Mascaux C, et al. Ki-67 expression and patients survival in lung cancer: systematic review of the literature with meta-analysis. Br J Cancer. 2004; 91(12): 2018–2025, doi: 10.1038/sj.bjc.6602233, indexed in Pubmed: 15545971.
12. Jakobsen JN, Sørensen JB. Clinical impact of ki-67 labeling index in non-small cell lung cancer. Lung Cancer. 2013; 79(1): 1–7, doi: 10.1016/j.lungcan.2012.10.008, indexed in Pubmed: 23137549.
13. Surov A, Meyer HJ, Wienke A. Standardized Uptake Values Derived from F-FDG PET May Predict Lung Cancer Microvessel Density and Expression of KI 67, VEGF, and HIF-1 but Not Expression of Cyclin D1, PCNA, EGFR, PD L1, and p53. Contrast Media Mol Imaging. 2018, doi: 10.1155/2018/9257929, indexed in Pubmed: 29983647.
14. Spyratos F, Ferrero-Poüs M, Trassard M, et al. Correlation between MIB-1 and other proliferation markers: clinical implications of the MIB-1 cutoff value. Cancer. 2002; 94(8): 2151–2159, doi: 10.1002/cncr.10458, indexed in Pubmed: 12001111.
15. Ishibashi N, Maebayashi T, Aizawa T, et al. Correlation between the Ki-67 proliferation index and response to radiation therapy in small cell lung cancer. Radiat Oncol. 2017; 12(1): 16, doi: 10.1186/s13014-016-0744-1, indexed in Pubmed: 28086989.

Original
Nuclear Medicine Review 2022, 25, 2: 78–84
DOI: 10.5603/NMR.a2022.0018

ISSN 1506–9680, e-ISSN 1644–4345

VIA MEDICA

[18F]FDG PET/CT and CA-125 in the evaluation of ovarian cancer relapse or persistence: is there any correlation?

Francesco Dondi, Domenico Albano, Francesco Bertagna, Raffaele Giubbini
Nuclear Medicine, Spedali Civili Brescia, Brescia, Italy

[Received 13 I 2022; Accepted 27 IV 2022]

Abstract

Background: Ovarian cancer relapse can be diagnosed by serum tumor markers measurements and 18F-fluorodoxyglucose positron emission tomography/computed tomography ([18F]FDG PET/CT) findings. The aim of our study was to analyze the potential relationship between cancer antigen 125 (CA-125) and PET/CT results in patients affected by ovarian cancer.

Material and methods: Ninety-two [18F]FDG PET/CT scans in sixty-one patients with diagnosis of ovarian cancer were analyzed and compared to CA-125 values. PET/CT results were compared to other imaging modalities, histology or follow-up data in order to define its diagnostic accuracy. PET/CT studies were analyzed qualitatively and semiquantitatively by measuring the maximum and mean standardized uptake value body weight max (SUVbw max, SUVbw mean), maximum SUV lean body mass (SUVlbm), maximum SUV body surface area (SUVbsa), metabolic tumor volume (MTV) and total lesion glycolysis (TLG) of hypermetabolic lesions. All measurements were compared with CA-125 values.

Results: Twenty PET/CT studies were true negative, sixty-three true positive, five false positive and four false negative with sensitivity of 94%, specificity of 80%, negative predictive value of 83%, positive predictive value of 93% and accuracy of 90%. CA-125 levels were significantly correlated with PET/CT results and all PET/CT semiquantitative parameters. CA-125 cutoff values of 17 UI/mL is the best compromise between sensitivity and specificity in discriminating between positive and negative PET/CT result.

Conclusions: [18F]FDG PET/CT has good accuracy in evaluating patients with relapse or persistance of ovarian cancer. CA-125 levels were significantly correlated with metabolic PET/CT parameters.

KEY words: PET/CT; ovarian cancer; tumor markers; CA-125

Nucl Med Rev 2022; 25, 2: 78–84

Introduction

Ovarian cancer is the leading cause of death among all gynecological cancers in developed countries. Because of its silent nature, most of the patients are diagnosed at advanced stages, defined as the spread of the tumor outside the pelvis [1, 2]. The staging system used worldwide for ovarian cancer is the International Federation for Gynecology and Obstetrics (FIGO) staging classification [3]. Staging of the disease is usually performed by multiple imaging modalities such as ultrasonography (US), particularly useful for the assessment of ovarian masses, computed tomography (CT), and magnetic resonance (MR). 18F-fluodeoxyglucose positron emission tomography/computed tomography ([18F]FDG PET/CT) is not usually performed for staging purposes, but its utility for the assessment of retroperitoneal lymph nodes is proved [4].

Cancer antigen 125 (CA-125) is a high-molecular-weight glycoprotein expressed on the surface of epithelial cells and is also a tumor marker that can play an important role in staging and restaging of ovarian cancer [1, 5]. Standard treatment of the disease includes aggressive cytoreductive surgery followed by platinum-/taxane-based chemotherapy [6].

Recurrence of this tumor is extremely frequent and in particular, 75% to 80% of all patients and 90% to 95% of patients with advanced disease (FIGO stage III/IV) will relapse within 2 years after primary treatment [7]. According to this, early identification of tumor recurrence is crucial to defining subsequent therapeutic approach.

Cancer antigen 125 (CA-125) is a sensitive and reliable tumor marker to investigate possible relapse or persistence of ovarian

Correspondence to: Omer Francesco Dondi, Nuclear Medicine, Spedali Civili di Brescia, P.le Spedali Civili, 1; 25123, Brescia, Italy
phone: +380303995461; e-mail: f.dondi@outlook.com

cancer: in particular in literature, it is reported an accuracy of 79% to 95%, and its values increase from 3 to 6 months before the clinical presentation of recurrence [8–9]. A progressive low-level increase of this marker is strongly predictive of disease relapse among patients who are in complete clinical remission [10].

Conventional imaging (CI), such as CT and MR, is also used in the evaluation of recurrence or persistence of disease with high variability in terms of sensitivity and specificity [1]. Furthermore, [^{18}F]FDG PET/CT is frequently performed in the work-up of possible recurrence, given its ability to identify relapse of the disease in both asymptomatic and symptomatic patients [11].

The purpose of our study was to assess the accuracy of [^{18}F]FDG PET/CT in detecting tumor relapse or persistence in patients previously treated for ovarian cancer. Furthermore, a possible a possible correlation between PET/CT parameters and CA-125 values was also investigated.

Material and methods

A total of 92 [^{18}F]FDG PET/CT scans were retrospectively included in the study. The scans came from 61 patients with a previous diagnosis of ovarian cancer and were performed in our center from July 2007 to October 2019. Patients with a history of multiple tumors expressing CA-125 (*i.e.* breast) were excluded from the study. All PET/CT scans were performed at least 1 month after the end of chemotherapy and 3 months after the end of surgery or radiotherapy.

A dose of 3–3.5 MBq/kg of [^{18}F]FDG was administered intravenously to the patient 60 minutes before image acquisition. Patients were instructed to void before acquisition and no contrast agents were administrated; written consent was also obtained before studies. PET/CT scans were performed from the skull base to the midthigh on a Discovery ST or Discovery 690 PET/CT tomograph (General Electric Company, GE, Milwaukee, Wisconsin) with standard parameters (CT: 80 mA, 120 kV; PET: 2.5–4 min per bed position, PET step of 15 cm). Reconstruction of images was performed in a 256×256 matrix and 60 cm field of view.

All PET/CT scans were visually and semiquantitatively analyzed by two experienced nuclear medicine physicians by consensus. In this setting, readers were aware of the clinical history of the patient but not about CA-125 levels. Focal tracer uptakes diverging from physiological distribution of radiotracer and background were regarded as suggestive of disease recurrence or persistence. For semiquantitative analysis the measure of the maximum and mean standardized uptake value bodyweight max (SUVbw max, SUVbw mean), maximum SUV lean body mass (SUVlbm), maximum SUV body surface area (SUVbsa), metabolic tumor volume (MTV), and total lesion glycolysis (TLG) of hypermetabolic lesions were performed. In this setting, MTV was extracted from [^{18}F]FDG PET images corrected for attenuation, with an SUV-based automated contouring program (Advantage Workstation 4.6, GE HealthCare). This operation was performed with an isocontour threshold method based on 41% of the SUVmax, as previously recommended by the European Association of Nuclear Medicine, because of its high interobserver reproducibility [12]. Furthermore, TLG was calculated by summing the product of MTV of each lesion for its SUVmean.

Cancer antigen 125 (CA-125) values were collected in a range of times within 2 months from the PET/CT scan. In particular, CA-125 was considered positive when higher or equal to 35 UI/mL, according to the reference values of our institution. In order to evaluate PET/CT diagnostic accuracy, the reference standard was a combination of clinical and imaging follow-up data collected for at least 12 months. When available, also histopathologic information was taken into account.

Statistical analysis

Statistical analyses were carried out using MedCalc Software version 17.1 for Windows (Ostend, Belgium). Categorical variable were presented with the calculation of simple and relative frequencies while the numeric variables were described with mean, standard deviation, minimum and maximum values. Furthermore, using final diagnosis as a reference, sensitivity (SE), specificity (SP), positive predictive value (PPV), negative predictive value (NPV), and accuracy (AC) were calculated based on Bayes's law, with 95% confidence intervals (CIs).

To assess the possible correlation between qualitative PET/CT results in tumor markers positivity or negativity, age (considering a threshold of 75 years), and stage (I/II *vs.* III/IV FIGO stage), Chi-Square test was performed. Furthermore, the Kruskall-Wallis test was performed to evaluate a possible correlation between PET/CT results and tumor markers considered as absolute values and with a cutoff of 35 UI/mL (positivity or negativity) and PET/CT semiquantitative parameters (SUVmax, SUVmean, SUVbsa, SUVlbm, MTV and TLG). P-value was considered statistically significant if < 0.05.

In order to identify the best CA-125 values able to discriminate between positive and negative PET/CT, receiver operating characteristic (ROC) curve analysis was then performed. Area Under Curve (AUC), SE, and SP were then obtained from this analysis.

Results

Mean age of patients was 64 (range 45–85) years; 2 of them had stage I disease according to FIGO staging system, 4 had stage II disease, 36 had stage III while stage IV was present in 19 patients. All patients had a PET/CT scan after surgical removal of the primary tumor. Of these patients, 2 didn't perform any therapy after surgery, 56 had chemotherapy after surgery, 1 performed radiotherapy after surgery while 2 patients performed a mix of radio- and chemotherapy after surgery.

Seventeen patients performed more than a single [^{18}F]FDG PET/CT scan, resulting in 32 scans carried out for re-staging or follow-up purposes. In particular, 10 patients performed 2 scans, 3 patients performed 3 scans, one performed 4 scans, 2 performed 5 scans and only one patient performed 6 PET/CT scans. Furthermore, of the 32 scans performed after a prior one, 8 were carried out to evaluate relapse of disease after a negative [^{18}F]FDG PET/CT exam, 3 were performed as a part of the follow-up of the patients, while 21 scans were performed for the evaluation of disease during or after treatment (in particular in one case the patients had radiotherapy before the scan while 20 patients had chemotherapy before PET/CT evaluation). The mean imaging follow-up time of patients with CT or MR scans was 22.7 months.

Serous carcinoma was the most frequent histotype with 53 cases; endometrioid carcinoma was present in 3 patients, carcinosarcoma in 2 while one patient had a mixed carcinoma, one an undifferentiated, and one a clear cell carcinoma respectively

Table 1. The main features of our 61 patients

	n (%)
Age [years] (mean, range)	64 (45–85)
FIGO stage	
I	2 (3%)
II	4 (7%)
III	36 (59%)
IV	19 (31%)
Therapy	
Surgery	2 (3%)
Surgery + chemotherapy	56 (92%)
Surgery + radiotherapy	1 (2%)
Surgery + chemotherapy + radiotherapy	2 (3%)
Histology	
Carcinosarcoma	2 (3%)
Clear cell	1 (2%)
Endometrioid	3 (5%)
Mixed	1 (2%)
Serous	53 (86%)
Undifferentiated	1 (2%)

FIGO — International Federation for Gynecology and Obstetrics

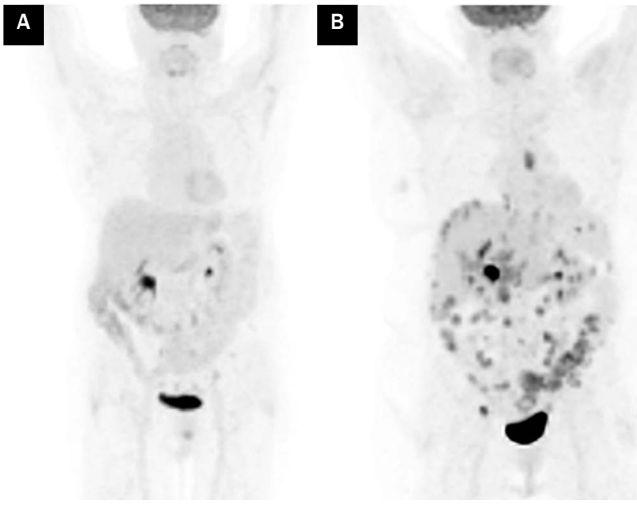

Figure 1. (**A**) Maximum intensity projection (MIP) of a negative [^{18}F]FDG PET/CT scan performed in a patient with negative CA-125; (**B**) MIP of a positive [^{18}F]FDG PET/CT scan performed in a patient with negative CA-125 showing peritoneal, thoracic, and abdominal localization of the disease

(Tab. 1). Cancer antigen 125 (CA-125) values were available in conjunction with PET/CT for all studies: 42 of them were under the normal limit while 50 were above.

Of the 92 PET/CT scans performed, 68 (74%) demonstrated the presence of recurrence of the disease while 24 (26%) were negative (Fig. 1). In the group of positive PET/CT, 43 (63%) demonstrated peritoneal localization of disease, 13 (19%) had a local relapse, 30 (44%) had abdominal nodal metastasis, 15 (22%) had thoracic nodal metastasis, 9 (13%) had hepatic metastasis, 3 (4%) had lung metastasis and 3 (4%) had spleen metastasis. One (2%) patient also had adrenal localization of the disease.

Among 68 positive PET/CT scans, 63 were confirmed as true positive while on subsequent follow-up 5 were classified as false positive. Histopathological diagnosis was possible for 41 (65%) of these studies. In one case we found a diffuse uptake in the left iliac wing that on a subsequent MR scan was classified as not pathological. Three false-positive scans were characterized by peritoneal focal uptakes interpreted as localization of disease that were not confirmed on subsequent radiological follow-up. Interestingly, in one patient we found a focal peritoneal uptake suggestive of localization of ovarian cancer but when removed this was diagnosed as a neuroendocrine tumor (Fig. 2).

Among 24 negative scans, 20 were confirmed as true negative while 4 resulted as false negative on subsequent follow-up (imaging follow-up with CT or MR scans for at least 12 months, in particular with a mean follow-up of 26.3 months): 2 of them had peritoneal or nodal metastasis of disease with dimension under 5 mm while in 2 cases PET/CT wasn't able to recognize lung localization for the same reason. Sensitivity (SE), specificity (SP), positive predictive value (PPV), negative predictive value (NPV) and accuracy (AC) of [^{18}F]FDG-PET/CT were 94% (85–98%), 80% (61–93%), 93% (85–96%), 83% (67–93%) and 90% (82–95%), respectively. Positive and negative likelihood ratios were 4.70 and 0.07, respectively.

Of the total of 92 PET/CT scans, 80 were performed by patients with a diagnosis of serous ovarian carcinoma while 12 patients were present with other histotypes. In the first group of patients, there were 4 false-negative scans, 5 false positives, 18 true negatives and 53 true positives; CA-125 was above the limit of 35 UI/mL in 42 cases while under this limit in 38. In the group of patients without serous carcinoma, 2 scans turned out to be true negative while 10 were true positive; CA-125 was positive in 8 cases and negative in 4.

A significant correlation was found between PET/CT results and CA-125 findings dichotomized as positive and negative ($p < 0.01$). No significant correlation was found between PET/CT results and stage or age (Tab. 2); the same happened when evaluating CA-125 results and stage or age.

A significant correlation between PET/CT results and CA-125 absolute values was found ($p < 0.01$) and as well as comparing CA-125 positivity or negativity and PET semiquantitative parameters ($p < 0.01$). A significant association was also found between CA-125 absolute values and semiquantitative PET parameters ($p < 0.01$) (Tab. 3).

In order to evaluate the possible influence of histotype on the correlation between PET/CT and CA-125, we decided to perform the aforementioned statistics by dividing the group of patients with serous carcinoma from other ones. In the group of the 80 patients with serous carcinoma, the significant correlation between PET/CT and CA-125 exposed before was confirmed. Otherwise, in the group of the 12 patients without serous carcinoma, the significant correlation wasn't confirmed.

Applying ROC curves analysis to all the 92 PET/CT scans, a value of 17 UI/mL for CA-125 (AUC 0.732, SE 84%, SP 62%) was extracted (Fig. 3). Furthermore, when comparing serum marker values using the aforementioned cutoff with PET/CT results, a significant association was observed ($p < 0.01$) (Tab. 4).

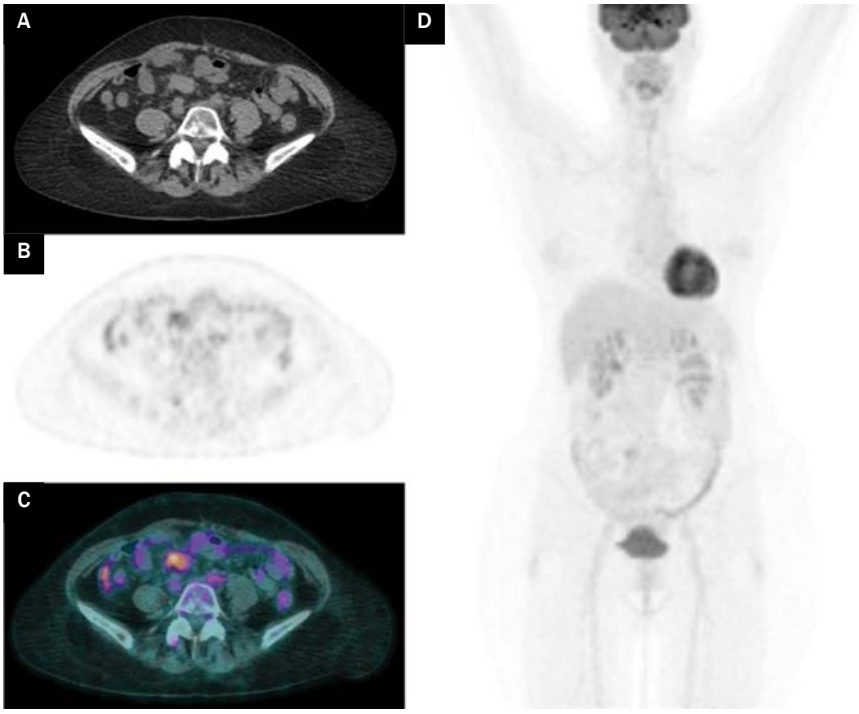

Figure 2. (**A**) Axial CT; (**B**) axial PET; (**C**) axial fused PET/CT; (**D**) and maximum intensity projection (MIP) images of an [^{18}F]FDG PET/CT scan demonstrating a focal peritoneal uptake in a patient with negative CA-125; subsequent removal of the lesion demonstrated the presence of a neuroendocrine tumor

Table 2. Correlation between PET/CT results and the main clinical features

	PET/CT		p-value
	Positive (%) n. 68	Negative (%) n. 24	
Age [years]			0.237
< 75	53 (78%)	22 (92%)	
≥ 75	15 (22%)	2 (8%)	
FIGO stage			0.357
I	1 (1%)	1 (4%)	
II	4 (6%)	0 (0%)	
III	37 (54%)	17 (71%)	
IV	26 (39%)	6 (25%)	
Therapy			
Surgery	1 (1%)	1 (4%)	
Surgery + chemotherapy	65 (97%)	22 (92%)	
Surgery + radiotherapy	1 (1%)	0 (0%)	
Surgery + chemotherapy + radiotherapy	1 (1%)	1 (4%)	
CA-125			0.002
Positive	44 (65%)	6 (25%)	
Negative	24 (35%)	18 (75%)	
CA-125 as continuos values	68 (100%)	24 (100%)	< 0.001

FIGO — International Federation for Gynecology and Obstetrics

Discussion

Relapse of ovarian cancer is extremely frequent affecting approximately 75% to 80% of all patients; 90% to 95% of patients with advanced disease (FIGO stage III/IV) will relapse within 2 years after primary treatment [7]. Furthermore, the role of [^{18}F]FDG PET/CT for the evaluation of relapse or persistence of disease and for the follow-up of patients has been underlined [11]. In a previous meta-analysis, Limei et al. [13] pointed out the fact that PET/CT may be the most accurate test for diagnosis of suspected recurrent ovarian cancer with high sensitivity and specificity and also a useful tool to evaluate the deextent of disease. In this context, the greatest value of [^{18}F]FDG PET/CT in ovarian cancer is represented by the high accuracy in detecting residual disease after primary treatment and in identifying recurrent disease in both symptomatic and asymptomatic patients [11]. PET/CT has also a role in optimizing the management plan in patients with recurrent ovarian cancer as was established previously (Ebina et al. [14] and Soussan et al. [15]).

Likewise, CA-125 is a sensitive and reliable tumor marker to investigate possible relapse of disease, with a reported accuracy of 79% to 95%, and its values increase from 3 to 6 months before the clinical presentation of recurrence [8–9]; it is also the simplest tool to trigger imaging and is a better approach than regular routine imaging for the diagnosis of recurrent ovarian cancer, as mentioned by the guidelines [2].

Table 3. Correlation between mean semiquantitative parameters and CA-125 values

	SUV-max	p-value	SUV-mean	p-value	SUVlbm	p-value	SUVbsa	p-value	MTV	p-value	TLG	p-value
CA-125 absolute values	9.52	< 0.001	5.09	< 0.001	6.67	< 0.001	2.49	< 0.001	21.94	< 0.001	184.71	< 0.001
CA-125		< 0.001		< 0.001		< 0.001		< 0.001		< 0.001		< 0.001
positive	9.66		5.09		6.69		2.53		23.01		194.45	
negative	3.61		3.91		2.83		1.02		8.20		67.92	

MTV — metabolic tumor volume; TLG — total lesion glycolysis

Table 4. Receiver operating characteristic (ROC) curves analysis for CA-125

	Value	AUC	Standard error	95% CI	Significance level	Sensitivity	Specificity
CA-125	17	0.732	0.055	0.629–0.819	0.0001	83.8	62.5

AUC — area under curve; CI — confidence interval

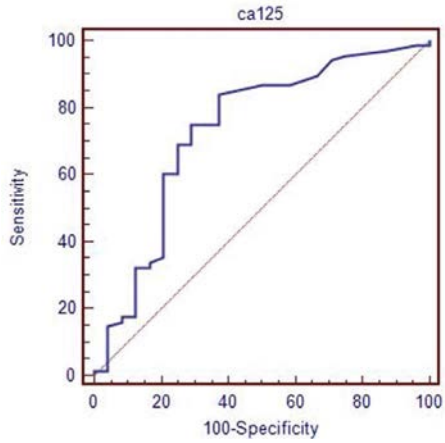

Figure 3. Receiver operating characteristic (ROC) curve was obtained when searching for the best tumor marker value for CA-125 to discriminate between positive PET/CT or negative one: a value of 17 UI/mL was obtained (AUC 0.732, SE 84%, SP 63%)

A meta-analysis by Gu et al. [5] reported that [^{18}F]FDG PET/CT could be a useful tool for current surveillance techniques, in particular for those patients with increasing CA-125 levels and negative CT or MR imaging. In this context, rising CA-125 levels in patients who were radically treated for ovarian cancer but show no evidence of relapse is the most frequent indication for PET/CT and high overall sensitivity (97%) has been obtained using PET/CT in asymptomatic patients with high serum CA-125 levels and non-conclusive results at CT [16–18]. A correlation between PET/CT and CA-125 could be therefore very useful since it can provide metabolic information allowing for differentiation between tumor recurrence and post-therapy scarring/fibrosis [1].

Our analysis confirmed the diagnostic value of [^{18}F]FDG PET/CT for the restaging of ovarian cancer after primary therapy. In particular, most of the exams resulted true positives and just a small amount of scans turned out to be false positives: in one case we found a diffuse uptake in the left iliac wing that on a subsequent MR scan was classified as not pathological, 3 were characterized by peritoneal focal uptakes interpreted as localization of disease that weren't confirmed and in 1 scan we found a focal peritoneal uptake suggestive of localization that was then diagnosed as a neuroendocrine tumor. Most of negative scans were confirmed as true negative and in the small amount of false negative, PET/CT was not able to identify pulmonary, peritoneal, or nodal lesions under its resolution power (5 mm).

The ranges of SE, SP, PPV, NPV and AC reported in literature for [^{18}F]FDG PET/CT in the restaging of ovarian cancer from some meta-analysis are 88% to 98%, 71% to 100%, 85% to 100%, 67% to 100% and 71% to 100% [5, 19]. Our results confirmed these evidences.

We find a significant correlation between PET scan positivity or negativity and CA-125 one. In the past Menzel et al. pointed out the correlation between CA-125 and PET/CT by demonstrating that serum marker levels were higher in patients whit positive PET/CT compared with patients with negative one and this finding was confirmed by other studies [1, 17].

Most of our patients had a diagnosis of serous carcinoma (87%) and this fact is really important to underline because it's known that this is the ovarian carcinoma histotype that expresses CA-125 the most; in other histotypes such as mucinous, endometrioid, and clear cell, the prognostic value of CA-125 is less known according to European guidelines [2]. In detail, 80% of serous ovarian cancer can express CA-125, while fewer than 30% of mucinous-, clear-cell-, and endometrioid cancer are positive for this surface antigen [20]. In this context, when applying statistical analysis between the two different groups of serous *vs.* non-serious carcinomas we reported a significant correlation between PET/CT and CA-125 just in the first group, underlying this different expression of tumor marker between different histotypes.

A significant correlation was also found between CA-125 absolute values and all PET semiquantitative parameters, CA-125 absolute values and PET/CT scan positivity or negativity, and PET semiquantitative parameters with CA-125 positivity or negativity. In the past, Kim et al. [21] pointed out a correlation between MTV and TLG with serum CA-125 levels at relapse in a patient with recurrence of ovarian epithelial cancer but they did not find any correlation between SUVmax and CA-125. These findings agree only in parts with ours, where also SUVmax is strongly correlated with CA-125 serum levels.

In the past, Kim et al. [6] reported a significant correlation of changes in [^{18}F]FDG PET/CT SUVmax, with recurrence in advanced epithelial ovarian cancer. Moreover, other papers noticed that the doubling time of CA-125 strongly correlates with recurrence and outcomes of ovarian cancer [22–23]. Evangelista et al. [24], observed that overall survival (OS) is significantly higher in patients with negative CA-125 values at the time of PET/CT, with negative PET/CT scan, and with no evidence of peritoneum recurrence and distant metastases. Moreover, Kim et al. [21] pointed out a significant correlation between MTV, TLG, and SUVmax with post-relapse survival. By underlying the significant correlation of PET/CT parameters and CA-125, we think that our study can confirm these findings.

A discriminating value of 17 UI/mL for CA-125 (AUC 0.732, SE 84%, SP 63%) for PET/CT positivity or negativity was underlined when applying ROC curve analysis. This value is very similar to the one found by Palomar et al. [16] in the past (18 UI/mL) when evaluating the role of [^{18}F]FDG PET/CT in 175 patients treated for ovarian cancer and with raised CA-125 levels. Similar results were also obtained by Fularz et al. [25] (17.6 UI/mL) in a study with 68 patients with suspicion of ovarian cancer relapse. Furthermore, when comparing serum marker values using the aforementioned cutoff with PET/CT results, a statistically significant association was observed.

Our work is not without limitations. First of all, its retrospective nature with heterogeneous clinical features of the population. Moreover, all 92 [^{18}F]FDG PET/CT came from a relatively low sample of patients. Lastly, a definitive histopathological diagnosis was not available for all PET/CT scans.

Conclusions

In conclusion, [^{18}F]FDG PET/CT is an accurate diagnostic tool to evaluate possible relapse or persistence of ovarian cancer after primary therapy. A strong correlation between PET qualitative and semiquantitative parameters and CA-125 values was underlined.

Conflict of interest

All the authors declare that they have no conflict of interest.

References

1. Marzola MC, Chondrogiannis S, Rubello D. Fludeoxyglucose F 18 PET/CT Assessment of Ovarian Cancer. PET Clin. 2018; 13(2): 179–202, doi: 10.1016/j.cpet.2017.11.005, indexed in Pubmed: 29482749.
2. Colombo N, Sessa C, Bois Adu, et al. ESMO–ESGO Ovarian Cancer Consensus Conference Working Group. ESMO-ESGO consensus conference recommendations on ovarian cancer: pathology and molecular biology, early and advanced stages, borderline tumours and recurrent disease. Int J Gynecol Cancer. 2019 [Epub ahead of print], doi: 10.1136/ijgc-2019-000308, indexed in Pubmed: 31048403.
3. Forstner R. Radiological staging of ovarian cancer: imaging findings and contribution of CT and MRI. Eur Radiol. 2007; 17(12): 3223–3235, doi: 10.1007/s00330-007-0736-5, indexed in Pubmed: 17701180.
4. Signorelli M, Guerra L, Pirovano C, et al. Detection of nodal metastases by 18F-FDG PET/CT in apparent early stage ovarian cancer: a prospective study. Gynecol Oncol. 2013; 131(2): 395–399, doi: 10.1016/j.ygyno.2013.08.022, indexed in Pubmed: 23988414.
5. Gu P, Pan LL, Wu SQ, et al. CA 125, PET alone, PET-CT, CT and MRI in diagnosing recurrent ovarian carcinoma: a systematic review and meta-analysis. Eur J Radiol. 2009; 71(1): 164–174, doi: 10.1016/j.ejrad.2008.02.019, indexed in Pubmed: 18378417.
6. Kim TH, Kim J, Kang YK, et al. Identification of Metabolic Biomarkers Using Serial F-FDG PET/CT for Prediction of Recurrence in Advanced Epithelial Ovarian Cancer. Transl Oncol. 2017; 10(3): 297–303, doi: 10.1016/j.tranon.2017.02.001, indexed in Pubmed: 28314183.
7. Antunovic L, Cimitan M, Borsatti E, et al. Revisiting the clinical value of 18F-FDG PET/CT in detection of recurrent epithelial ovarian carcinomas: correlation with histology, serum CA-125 assay, and conventional radiological modalities. Clin Nucl Med. 2012; 37(8): e184–e188, doi: 10.1097/RLU.0b013e31825b2583, indexed in Pubmed: 22785525.
8. Goonewardene TI, Hall MR, Rustin GJS. Management of asymptomatic patients on follow-up for ovarian cancer with rising CA-125 concentrations. Lancet Oncol. 2007; 8(9): 813–821, doi: 10.1016/S1470-2045(07)70273-5, indexed in Pubmed: 17765190.
9. Rustin GJ, Nelstrop AE, McClean P, et al. Defining response of ovarian carcinoma to initial chemotherapy according to serum CA 125. J Clin Oncol. 1996; 14(5): 1545–1551, doi: 10.1200/JCO.1996.14.5.1545, indexed in Pubmed: 8622070.
10. Santillan A, Garg R, Zahurak ML, et al. Risk of epithelial ovarian cancer recurrence in patients with rising serum CA-125 levels within the normal range. J Clin Oncol. 2005; 23(36): 9338–9343, doi: 10.1200/JCO.2005.02.2582, indexed in Pubmed: 16361633.
11. Ghosh J, Thulkar S, Kumar R, et al. Role of FDG PET-CT in asymptomatic epithelial ovarian cancer with rising serum CA-125: a pilot study. Natl Med J India. 2013; 26(6): 327–331, indexed in Pubmed: 25073988.
12. Boellaard R, Delgado-Bolton R, Oyen WJG, et al. European Association of Nuclear Medicine (EANM). FDG PET/CT: EANM procedure guidelines for tumour imaging: version 2.0. Eur J Nucl Med Mol Imaging. 2015; 42(2): 328–354, doi: 10.1007/s00259-014-2961-x, indexed in Pubmed: 25452219.
13. Limei Z, Yong C, Yan Xu, et al. Accuracy of positron emission tomography/computed tomography in the diagnosis and restaging for recurrent ovarian cancer: a meta-analysis. Int J Gynecol Cancer. 2013; 23(4): 598–607, doi: 10.1097/IGC.0b013e31828a183c, indexed in Pubmed: 23502451.
14. Ebina Y, Watari H, Kaneuchi M, et al. Impact of FDG PET in optimizing patient selection for cytoreductive surgery in recurrent ovarian cancer. Eur J Nucl Med Mol Imaging. 2014; 41(3): 446–451, doi: 10.1007/s00259-013-2610-9, indexed in Pubmed: 24221243.
15. Soussan M, Wartski M, Cherel P, et al. Impact of FDG PET-CT imaging on the decision making in the biologic suspicion of ovarian carcinoma recurrence. Gynecol Oncol. 2008; 108(1): 160–165, doi: 10.1016/j.ygyno.2007.07.082, indexed in Pubmed: 17961640.
16. Palomar A, Nanni C, Castellucci P, et al. Value of FDG PET/CT in patients with treated ovarian cancer and raised CA125 serum levels. Mol Imaging Biol. 2012; 14(1): 123–129, doi: 10.1007/s11307-010-0468-9, indexed in Pubmed: 21240639.
17. Menzel C, Döbert N, Hamscho N, et al. The influence of CA 125 and CEA levels on the results of (18)F-deoxyglucose positron emission tomography in suspected recurrence of epithelial ovarian cancer. Strahlenther Onkol. 2004; 180(8): 497–501, doi: 10.1007/s00066-004-1208-3, indexed in Pubmed: 15292970.
18. Thrall MM, DeLoia JA, Gallion H, et al. Clinical use of combined positron emission tomography and computed tomography (FDG-PET/CT) in recurrent ovarian cancer. Gynecol Oncol. 2007; 105(1): 17–22, doi: 10.1016/j.ygyno.2006.10.060, indexed in Pubmed: 17208284.
19. Suppiah S, Chang WL, Hassan HA, et al. Systematic Review on the Accuracy of Positron Emission Tomography/Computed Tomography and Positron Emission Tomography/Magnetic Resonance Imaging in the Management of Ovarian Cancer: Is Functional Information Really Needed? World J Nucl

Med. 2017; 16(3): 176–185, doi: 10.4103/wjnm.WJNM_31_17, indexed in Pubmed: 28670174.

20. Mainguené C, Aillet G, Kremer M, et al. Immunohistochemical study of ovarian tumors using the OC 125 monoclonal antibody as a basis for potential in vivo and in vitro applications. J Nucl Med Allied Sci. 1986; 30(1): 19–22, indexed in Pubmed: 3528419.
21. Kim CY, Jeong SY, Chong GOh, et al. Quantitative metabolic parameters measured on F-18 FDG PET/CT predict survival after relapse in patients with relapsed epithelial ovarian cancer. Gynecol Oncol. 2015; 136(3): 498–504, doi: 10.1016/j.ygyno.2014.12.032, indexed in Pubmed: 25557270.
22. Han LY, Karavasilis V, Hagen Tv, et al. Doubling time of serum CA125 is an independent prognostic factor for survival in patients with ovarian cancer relapsing after first-line chemotherapy. Eur J Cancer. 2010; 46(8): 1359–1364, doi: 10.1016/j.ejca.2010.02.012, indexed in Pubmed: 20303743.
23. Varughese E, Kondalsamy-Chennakesavan S, Obermair A. The value of serum CA125 for the development of virtual follow-up strategies for patients with epithelial ovarian cancer: a retrospective study. J Ovarian Res. 2012; 5: 11, doi: 10.1186/1757-2215-5-11, indexed in Pubmed: 22436532.
24. Evangelista L, Palma MD, Gregianin M, et al. Diagnostic and prognostic evaluation of fluorodeoxyglucose positron emission tomography/computed tomography and its correlation with serum cancer antigen-125 (CA125) in a large cohort of ovarian cancer patients. J Turk Ger Gynecol Assoc. 2015; 16(3): 137–144, doi: 10.5152/jtgga.2015.15251, indexed in Pubmed: 26401105.
25. Fularz M, Adamiak P, Czepczyński R, et al. Utility of PET/CT in the diagnosis of recurrent ovarian cancer depending on CA 125 serum level. Nuklearmedizin. 2015; 54(4): 158–162, doi: 10.3413/Nukmed-0709-14-11, indexed in Pubmed: 26076719.

VIA MEDICA

Nuclear Medicine Review 2022, 25, 2: 85–88
DOI: 10.5603/NMR.a2022.0019

ISSN 1506–9680, e-ISSN 1644–4345

Original

Sensitivity and specificity of nuclear medicines (DTPA and DMSA) with magnetic resonance imaging in diagnosing bone metastasis

Shoaa G. Shetewi[1], Jaber Alyami[2], Bander S. Al Mutairi[1], Saeed M. Bafaraj[2]

[1]Department of Radiology, King Abdulaziz University Hospital, Jeddah, Saudi Arabia
[2]Radiology Sciences Department, King Abdulaziz University, Jeddah, Saudi Arabia

[Received 3 III 2022; Accepted 27 IV 2022]

Abstract

Background: The frequency of bone metastases in individuals increases at advanced stages of cancer, mostly in patients suffering from lung, breast, or prostate cancer. The study aims to evaluate the effectiveness of bone metastases diagnosis of nuclear medicine, CT scan, and MRI in detecting bone metastases among patients with lung, breast, and prostate carcinoma.

Material and methods: Retrospective study design was adopted for the analysis of 120 recruited patients (with the presence of bone metastasis) following a series of examinations and tests.

Results: Better sensitivity (73.33%) and specificity (94.66%) for MRI as compared to SPECT. MRI also proved to be more sensitive (68%) and specific (95.74%), as compared to the findings of the CT scan.

Conclusions: The results conclude that MRI provided favorable diagnostic performance for bone metastasis. It emphasizes that diagnosis using MRI may enable practitioners to devise optimal carcinoma treatment strategies. The healthcare practitioners need to assess the MRI findings to determine improved treatment plans.

KEY words: bone; metastasis; magnetic resonance imaging; nuclear medicine

Nucl Med Rev 2022; 25, 2: 85–88

Introduction

The process of metastasis is a debilitating property of a malignant tumor that is not confined to its origin site *i.e.*, the primary tumor site, but it can detach and spread to other parts of the body forming secondary tumors [1]. The formation of secondary tumors inside the bone or bone metastasis in a cancer patient is an incapacitating and often untreatable disease [2]. Halabi et al. [3] revealed an incidence of approximately 65–75% of skeletal involvement among patients with advanced cancer. After the lymph nodes, the skeleton is the second common malignancy site for the development of metastases from prostate or breast cancer. Mostly, the presence of bone metastases is implied to any alteration in an ongoing treatment, where survival prospects of the affected individual are low [4]. Complications such as spinal paralysis and pathological fractures caused by bone metastasis increase the complexity of the cancer treatment and pose a significant impact on an individual's quality of life [5]. Several studies have revealed that the diagnosis of bone metastases can have a substantial impact on the overall treatment strategy [3, 6].

The use of contemporary imaging techniques has enabled the rapid diagnosis of bone metastases. Nuclear medicine and magnetic resonance imaging (MRI) have a significant role in the diagnosis and therapy of bone metastases. The imaging of bone is considered one of the first nuclear medicine techniques. The sensitivity of nuclear medicine is 90 percent greater as compared to other imaging methods, particularly, when there is a compression of the spinal cord or inclusion of radiographic examination [7]. Whole-body MRI, axial skeleton MRI, and routine prostate/breast MRI are significant in the diagnosis of bone metastases [8]. The number of metastatic foci in the skeletal system is evaluated through suitable

Correspondence to: Saeed M. Bafaraj, King Abdulaziz University, 21589 Jeddah, Saudi Arabia
e-mail: smbafaraj@kau.edu.sa

selected diagnostic imaging techniques, including positron emission tomography (PET), bone scintigraphy (BS), and whole-body MRI [9]. Whereas, according to Lukaszewski et al. [6], the extent of metastasis and its mixed, osteolytic, osteoblast characteristics are determined through complementary imaging examinations such as MRI, X-rays, and computed tomography (CT) scan.

One of the significant advantages of using MRI is the reporting of bone metastases response to treatment, using functional approaches, quantitative parameters, and morphologic images [10]. According to Qu, Huang at al. [11], compared to MRI or BS, PET scan was found more sensitive and specific in detecting bone metastasis due to lung cancer. Whereas, according to Huysse at al. [12], MRI has higher sensitivity compared to PET on a lesion level and has a low probability of false-negative results. Also, there is a predominant up-regulation of osteoblastic activity in bone metastases, which may lead to the formation of mineralized woven bone [13]. This condition shows a characteristic osteosclerotic appearance and is recognized as an osteoclast that plays a significant role in the pathophysiology of metastatic growth procedures [13]. The techniques, including nuclear medicine, CT scan, and MRI, can improve the diagnosis and check the response of therapy among cancer patients [6]. There is a strong need to evaluate and reveal the effectiveness of the mentioned techniques in detecting bone metastases in patients with lung, breast, and prostate carcinoma. This study significantly contributes by highlighting each modality's pros and cons, along with their response to treatment, and diagnoses of bone metastases. Additionally, it presents a practical approach for the evaluation of bone metastasis and the diagnosis of bone metastasis.

Nuclear medicines are widely used in approximately all the imaging techniques. But the diagnosis through this sometimes shows the false-negative results [14]. This misdiagnosis ultimately troubles the oncologist as well as the patient who does not understand the stage of bone metastases. Diethylenetriamine pentaacetate (DTPA) and dimercaptosuccinic acid (DMSA) are used with CT scans, and MRI and PET scanning. In the current study, both of these nuclear medicines were used in order to find their specificity and sensitivity in the diagnosis of bone metastases.

Although previous researchers have established the significance of digital imaging of bone metastasis in detecting and evaluating prostate, breast, and lung cancer; no empirical evidence is found concerning the agreement on the optimal imaging modality for detecting the specific disease. Union for International Cancer Control (UICC), response evaluation criteria in solid tumors, and World Health Organization (WHO) have developed the evaluation of bone tumor response criteria, but its execution was not found up to the mark in clinical practice and hence dissolved [15]. The comparison between nuclear medicines, DTPA and DMSA, with MRI for their specificity and sensitivity in detecting bone metastases has not been studied explicitly among prostate, lung, and breast carcinoma. The present study, therefore, bridges this gap and provides an evaluation of the quality parameters between different digital imaging systems and modalities of digital imaging systems. Mainly, it outlines the superiority of an imaging system over others concerning quality and sensitivity.

Materials and methods

Study design

This study is purely based on the retrospective design. The selection of this design is based on its efficacy for concluding effective results in previous studies [16, 17]. However, the present study differs from these studies in terms of its inclusion criteria, sample collection, and region. In this study, the patients with histologically proven malignancy but unknown bone metastasis were recruited. The patients were mainly diagnosed with prostate, lung, and breast carcinoma.

Study sample

The selection of the participants was based on the determining inclusion and exclusion criteria. Malignant patients who have the age 18 years or above were included in the study. The presence of bone metastasis was also one of the main factors that were ensured in the inclusion criteria. All the pregnant or lactating women were excluded from the study. Based on inclusion and exclusion criteria, a total of 120 patients were recruited for the study. The sample size was comparable to a similar study by Bafaraj [18]. Also, GPower 3.1 software was used to determine if the sample size comes within the estimated power analysis. It was calculated that at least 88 cases were required for 80% power with a 0.05 margin of error.

Data collection

Among these 120 patients, 37.5% were male, and the remaining 62.5% were female. These patients went through nuclear medicine scanning for the diagnosis of bone metastasis in them.

Study procedure

Diagnosis of metastasis, each patient was assessed for the presence of bone metastases using a series of examinations and tests. The presence was confirmed based on the application of MDP, MRI findings, and CT scan findings. For the CT scan, different angles of the patient's body were assessed, and cross-sectional images (slices) of the bones were created through computer processing. DTPA and DMSA are radioactive compounds that were used to perform scanning. MRI was performed using contrast material, typically gadolinium, which enhanced the appearance of certain details [19].

Measurement of sensitivity and specificity

Results obtained from the overall findings of each test were used to measure the sensitivity and specificity of each technique. In order to get the values of specificity and sensitivity, the results with true positive (TP), true negative (TN), false positive (FP), and false negative (FN) findings were isolated. Positive and negative predictive values were also obtained by using the obtained data [16].

Formula to measure the % sensitivity = $TP/(TP + FN) \times 100$

Formula to measure the % specificity = $TN/(TN + FP) \times 100$

Formula to measure the positive predictive value =

$= TP/(TP + FP) \times 100$

Formula to measure the negative predictive value =

$= TN/(TN + FN) \times 100$

Table 1. MRI Findings with diethylenetriamine pentaacetate (DTPA) and dimercaptosuccinic acid (DMSA)

Bone metastasis	TP	TN	FP	FN	Sensitivity	Specificity	PPV	NPV	p-value
DTPA	33	71	4	12	73.33%	94.66%	89.18%	85.54%	0.001
DMSA	34	67	3	16	68%	95.74%	68%	80.72%	0.001

TP — true positive; TN — true negative; FP — false positive; FN — false negative; PPV — positive predictive value; NPV — negative predictive value; DTPA — diethylenetriamine pentaacetate; DMSA — dimercaptosuccinic acid

Data analysis

All the examinations were observed following the administration of nuclear medicine. MRI scan was read in a standard workstation. The test was performed in segmental view. Data were analyzed through descriptive statistics using SPSS (Statistical Package for Social Sciences) Version 20.0. Pearson chi-square test was used to analyze the data for negative and positive cases. The results obtained from the interpretations were confirmed through clinical follow-up, histological evaluation, and other imaging studies.

Results

Table 1 shows statistically significant results for the detection of bone metastases through MRI using DMSA and DTPA. Sensitivity of DPTA and DMSA was 73.3% and 68% respectively which shows that the sensitivity of DPTA is significantly better than DMSA (p-value = 0.001). However, the specificity of both of these nuclear medicines was almost the same that is 94.66% and 95.74% (p-value = 0.001). Positive and negative predictive values were also obtained that show significantly higher PPV values of DTPA (89.18%) than DMSA (68%) (p-value = 0.001). NPV values were near in both of the scans *i.e.* DTPA and DMSA (85.54% and 80.72%). Overall, DTPA was found to be significantly better nuclear medicine compared to the DMSA which can be used in the diagnosis of bone metastasis with greater sensitivity and specificity.

Discussion

The study empirically reveals the sensitivity, specificity, and accuracy of two different nuclear medicines, DPTA and DMSA, with MRI scan through descriptive statistics. It found DTPA to be significantly more specific and sensitive in detecting bone metastasis. The sensitivity and specificity of MRI among cancer patients are more optimum as compared to any other imaging technique like CT/PET, BS, or SPECT findings [20]. As metastasis usually involves multiple sites and organs, therefore, a technique that does full-body imaging is more convenient and time-saving for patients [21]. Diethylenetriamine pentaacetate (DTPA) and dimercaptosuccinic acid (DMSA) are two different nuclear medicine that are used in the analysis of various organ functions and are widely used in the diagnosis of bone metastases of the whole body. DMSA and DTPA are also useful in the diagnosis of various organ function detection and show similar effects when used with CT or SPECT. The previous study shows that they exert no significant difference in imaging technique when doing renal scans, however, no study has compared their efficiency against each other in diagnosing bone metastasis [22]. These two nuclear medicines are very specific in the identification of bone metastases [23].

In this study, patients with prostate, lung, and breast carcinoma were enrolled. These tumors are widely found, and early and accurate diagnosis of these malignancies is a big challenge [24]. The present study would be helpful for such patients to know their metastatic stage earlier so that it can be managed accordingly. It is suggested that healthcare practitioners should assess the MRI findings with DTPA for determining improved treatment plans. However, consideration of the clinical setting and the clinical risk to the patients must also be studied for improved interpretation of the risk of bone metastasis.

The study was limited due to its retrospective nature. As the data were retrospectively collected, it was assumed that the scans and MRIs were done nearly at the same time. A similar prospective study on a larger population is suggested to have the diagnostic tests done nearly at the same time for more accuracy and a comparison with other modalities can also be done.

Conclusions

Magnetic resonance imaging (MRI) proves itself as the most accurate technique in the diagnosis and tumor and its metastases. This nuclear medicine made it more valuable in the identification. It is concluded that DTPA is more specific and sensitive in diagnosing bone metastases. The positive predictive value of DTPA is also greater than that of DMSA which also supports this finding. It provides clinical implication for using DTPA in detecting bone metastasis.

Conflict of interest

The authors declare that there is no conflict of interest regarding the publication of this paper.

Acknowledgment

The author is very thankful to all the associated personnel in any reference that contributed in/for the purpose of this research.

References

1. Welch DR, Hurst DR. Defining the Hallmarks of Metastasis. Cancer Res. 2019; 79(12): 3011–3027, doi: 10.1158/0008-5472.CAN-19-0458, indexed in Pubmed: 31053634.
2. Esposito M, Guise T, Kang Y. The Biology of Bone Metastasis. Cold Spring Harb Perspect Med. 2018; 8(6), doi: 10.1101/cshperspect.a031252, indexed in Pubmed: 29101110.
3. Halabi S, Kelly WK, Ma H, et al. Meta-Analysis Evaluating the Impact of Site of Metastasis on Overall Survival in Men With Castration-Resistant Prostate Cancer. J Clin Oncol. 2016; 34(14): 1652–1659, doi: 10.1200/JCO.2015.65.7270, indexed in Pubmed: 26951312.

4. Parker C, Gillessen S, Heidenreich A, et al. ESMO Guidelines Committee. Cancer of the prostate: ESMO Clinical Practice Guidelines for diagnosis, treatment and follow-up. Ann Oncol. 2015; 26 Suppl 5: v69–v77, doi: 10.1093/annonc/mdv222, indexed in Pubmed: 26205393.
5. Sevimli R, Korkmaz MF. Analysis of orthopedic surgery of patients with metastatic bone tumors and pathological fractures. J Int Med Res. 2018; 46(8): 3262–3267, doi: 10.1177/0300060518770958, indexed in Pubmed: 29690812.
6. Łukaszewski B, Nazar J, Goch M, et al. Diagnostic methods for detection of bone metastases. Contemp Oncol (Pozn). 2017; 21(2): 98–103, doi: 10.5114/wo.2017.68617, indexed in Pubmed: 28947878.
7. Glaudemans A, Lam M, Veltman N, et al. The Contribution Of Nuclear Medicine In The Diagnosis Of Bone Metastases. Bone Metastases. 2009: 137–162, doi: 10.1007/978-1-4020-9819-2_7.
8. Kim JH, Lee B, Chung BI, et al. Diagnostic Performance of Magnetic Resonance Imaging for the Detection of Bone Metastasis in Prostate Cancer: A Systematic Review and Meta-analysis. Eur Urol. 2018; 73(1): 81–91, doi: 10.1016/j.eururo.2017.03.042, indexed in Pubmed: 28412063.
9. Macedo F, Ladeira K, Pinho F, et al. Bone Metastases: An Overview. Oncol Rev. 2017; 11(1): 321, doi: 10.4081/oncol.2017.321, indexed in Pubmed: 28584570.
10. Lecouvet FE, Talbot JN, Messiou C, et al. EORTC Imaging Group. Monitoring the response of bone metastases to treatment with Magnetic Resonance Imaging and nuclear medicine techniques: a review and position statement by the European Organisation for Research and Treatment of Cancer imaging group. Eur J Cancer. 2014; 50(15): 2519–2531, doi: 10.1016/j.ejca.2014.07.002, indexed in Pubmed: 25139492.
11. Qu X, Huang X, Yan W, et al. A meta-analysis of ^{1} FDG-PET-CT, ^{1} FDG-PET, MRI and bone scintigraphy for diagnosis of bone metastases in patients with lung cancer. Eur J Radiol. 2012; 81(5): 1007–1015, doi: 10.1016/j.ejrad.2011.01.126, indexed in Pubmed: 21354739.
12. Huysse W, Lecouvet F, Castellucci P, et al. Prospective Comparison of F-18 Choline PET/CT Scan Versus Axial MRI for Detecting Bone Metastasis in Biochemically Relapsed Prostate Cancer Patients. Diagnostics (Basel). 2017; 7(4): 56, doi: 10.3390/diagnostics7040056, indexed in Pubmed: 29039785.
13. Clézardin P. Pathophysiology of bone metastases from solid malignancies. Joint Bone Spine. 2017; 84(6): 677–684, doi: 10.1016/j.jbspin.2017.05.006, indexed in Pubmed: 28499894.
14. Borofsky S, George AK, Gaur S, et al. What Are We Missing? False-Negative Cancers at Multiparametric MR Imaging of the Prostate. Radiology. 2018; 286(1): 186–195, doi: 10.1148/radiol.2017152877, indexed in Pubmed: 29053402.
15. Hamaoka T, Madewell JE, Podoloff DA, et al. Bone imaging in metastatic breast cancer. J Clin Oncol. 2004; 22(14): 2942–2953, doi: 10.1200/JCO.2004.08.181, indexed in Pubmed: 15254062.
16. Hawass NE. Comparing the sensitivities and specificities of two diagnostic procedures performed on the same group of patients. Br J Radiol. 1997; 70(832): 360–366, doi: 10.1259/bjr.70.832.9166071, indexed in Pubmed: 9166071.
17. Shen G, Deng H, Hu S, et al. Comparison of choline-PET/CT, MRI, SPECT, and bone scintigraphy in the diagnosis of bone metastases in patients with prostate cancer: a meta-analysis. Skeletal Radiol. 2014; 43(11): 1503–1513, doi: 10.1007/s00256-014-1903-9, indexed in Pubmed: 24841276.
18. Bafaraj SM. Significance of nuclear medicine scan in comparison with diethylenetriamine pentaacetic acid and ultrasound imaging in diagnosing renal disorders: An observational study. Medicine (Baltimore). 2020; 99(36): e22038, doi: 10.1097/MD.0000000000022038, indexed in Pubmed: 32899061.
19. Balci TA, Ciftci I, Karaoglu A. Incidental DTPA and DMSA uptake during renal scanning in unknown bone metastases. Ann Nucl Med. 2006; 20(5): 365–369, doi: 10.1007/BF02987249, indexed in Pubmed: 16878710.
20. Shen G, Deng H, Hu S, et al. Comparison of choline-PET/CT, MRI, SPECT, and bone scintigraphy in the diagnosis of bone metastases in patients with prostate cancer: a meta-analysis. Skeletal Radiol. 2014; 43(11): 1503–1513, doi: 10.1007/s00256-014-1903-9, indexed in Pubmed: 24841276.
21. Damle NA, Bal C, Bandopadhyaya GP, et al. The role of 18F-fluoride PET-CT in the detection of bone metastases in patients with breast, lung and prostate carcinoma: a comparison with FDG PET/CT and 99mTc-MDP bone scan. Jpn J Radiol. 2013; 31(4): 262–269, doi: 10.1007/s11604-013-0179-7, indexed in Pubmed: 23377765.
22. Fahmy H, Yassin H, Muhamed I, et al. Evaluation of the Efficiency of 99mTc-DMSA as a Radiopharmaceutical in Dynamic Renal Scans. Erciyes Tıp Dergisi/Erciyes Medical Journal. 2018; 40(3): 140–147, doi: 10.5152/etd.2018.0014.
23. Kimura T. Multidisciplinary Approach for Bone Metastasis: A Review. Cancers (Basel). 2018; 10(6), doi: 10.3390/cancers10060156, indexed in Pubmed: 29795015.
24. Loud JT, Murphy J. Cancer Screening and Early Detection in the 21 Century. Semin Oncol Nurs. 2017; 33(2): 121–128, doi: 10.1016/j.soncn.2017.02.002, indexed in Pubmed: 28343835.

VIA MEDICA

Nuclear Medicine Review 2022, 25, 2: 89–94
DOI: 10.5603/NMR.a2022.0020

ISSN 1506–9680, e-ISSN 1644–4345

Original

Optimal timing of SPECT/CT to demonstrate parathyroid adenomas in ^{99m}Tc-sestamibi scintigraphy

Kate Hunter, Niamh Gavin, Colin McQuade, Brendan Hogan, John Feeney

Tallaght University Hospital, Dublin, Ireland

[Received: 26 V 2021; Accepted: 22 VI 2022]

Abstract

Background: Accurate preoperative localisation of the parathyroid adenoma is essential to achieve a minimally invasive parathyroidectomy. The purpose of this study was to validate and improve our single-isotope dual-phase parathyroid imaging protocol utilising ^{99m}Technetium-Sestamibi ([^{99m}Tc]MIBI). There has been no accepted gold standard evidence-based protocol regarding timing of single-photon emission computed tomography/computed tomography (SPECT/CT) acquisition in parathyroid imaging with resultant variation between centres. We sought to determine the optimum timing of SPECT/CT post administration of [^{99m}Tc]MIBI in the identification of parathyroid adenomas. We aimed to evaluate the efficacy of early and late SPECT/CT and to establish whether SPECT/CT demonstrates increased sensitivity over planar imaging.

Material and methods: A sample of 36 patients with primary hyperparathyroidism underwent planar and SPECT/CT acquisition 15 minutes (early) and two hours (late) post [^{99m}Tc]MIBI administration. Two radionuclide radiologists reviewed the images and Fisher's exact Chi-squared statistic was used to evaluate the diagnostic performances of early versus late SPECT/CT acquisition and SPECT/CT versus planar imaging.

Results: Twenty-one likely parathyroid adenomas were identified with a statistically superior diagnosis rate in the late SPECT/CT acquisition compared with both early SPECT/CT and planar imaging ($p < 0.05$). All adenomas diagnosed on early SPECT/CT acquisition were also identified on late SPECT/CT images.

Conclusions: Single late phase SPECT/CT is significantly superior to early SPECT/CT in the identification of parathyroid adenomas. Late SPECT/CT improves diagnostic accuracy over planar acquisition. Imaging protocols should be revised to include late SPECT/CT acquisition. Early SPECT/CT acquisition can be eliminated from scan protocols with associated implications regarding reduced scan time and increased patient throughput.

KEY words: parathyroid scintigraphy; [^{99m}Tc]MIBI; sestamibi; SPECT/CT

Nucl Med Rev 2022; 25, 2: 89–94

Introduction

Untreated primary hyperparathyroidism can result in significant morbidity including renal calculi, osteoporosis and hypercalcemia-related complications [1]. Lifetime risk of primary hyperparathyroidism (PHPT) is estimated at 1% with up to 80% of cases due to the presence of a solitary parathyroid adenoma and less common causes including glandular hyperplasia and carcinoma [2]. For asymptomatic PHTP, medical management and conservative treatment are possible, however, surgical removal of hyperfunctioning parathyroid tissue remains the only definitive treatment [3].

Historically, the gold standard for parathyroidectomy was invasive surgery, with bilateral neck exploration necessary to locate all four parathyroid glands. Today, focused parathyroidectomy is the preferred surgical approach, made possible by pre-operative localization. Accuracy of localization is crucial to ensure successful targeted and minimally invasive surgery [4, 5]. Technetium-99m labeled sestamibi ([^{99m}Tc]MIBI) scintigraphy is the imaging agent of choice with reported sensitivities of up to 90% in accurately localizing a solitary parathyroid adenoma [6]. Planar imaging is increasingly supplemented with hybrid SPECT/CT for three-dimensional representation and anatomical localization.

Correspondence to: Kate Hunter, Tallaght University Hospital, Dublin, Ireland, phone: +35314143745, fax: +35314149805, e-mail: hunterk@tcd.ie

Dual phase imaging including early and late phase acquisition exploits the premise of differential washout of [^{99m}Tc]MIBI, with rapid wash-out from thyroid tissue and late phase retention of [^{99m}Tc]MIBI in a parathyroid adenoma [7]. However, this pattern does not occur in approximately 25% of cases raising the potential for false-negative studies [8]. False-positive results are caused by thyroid nodules, thyroiditis, and metastatic cervical lymph nodes potentially retaining [^{99m}Tc]MIBI [9]. The detection of smaller parathyroid adenomas, multiple adenomas, and parathyroid hyperplasia also poses a challenge. It has been suggested that variable uptake of [^{99m}Tc]MIBI by parathyroid adenomas is related to the number of mitochondria present in the abnormal tissue [10]. Proposed explanations for the absence of increased radiotracer uptake include multidrug resistance-associated protein and a relatively lower proportion of oxyphil cells [11].

The addition of computed tomography (CT) to gamma camera installations provides accurately localized functional and anatomical information with improved sensitivity and specificity [12].

The use of SPECT and or SPECT/CT and the timing of such acquisitions can differ greatly. Imaging protocols vary widely with significant differences in methodology between nuclear medicine departments. There is no single accepted generic protocol for parathyroid scintigraphy using SPECT/CT. In this study, we aimed to determine the optimum timing of SPECT/CT in the identification of parathyroid adenomas.

The study objective was to validate and improve local single isotope dual-phase parathyroid imaging protocols utilizing [^{99m}Tc]MIBI. We sought to establish if there is any significant difference between early and late SPECT/CT imaging in the detection and localization of parathyroid adenomas. We also wished to determine if SPECT/CT leads to improved sensitivity in the diagnosis of parathyroid adenomas when used as an adjunct to planar parathyroid scintigraphy.

Material and methods

Inclusion criteria

A prospective consecutive sampling method was employed over a 6 month period among patients who presented to our institution for investigation of PHPT. Patients were injected with [^{99m}Tc]MIBI 740 MBq (0.02 Curie) with an accepted tolerance range of 666–777 MBq (0.018–0.021 Curie). The patients were imaged on either a Siemens Symbia T2 or a Symbia T16, with a scanner chosen according to availability at the time of patient presentation. The same scanner was used for both early and late phase acquisition on a single patient in order to minimize intra-subject variability.

Acquisition protocol and scan parameters

The patient was positioned supine with a scan field of view extending from the superior orbital margin to the superior heart border. An initial planar image was acquired with a cobalt maker positioned at the sternal notch to provide an anatomical reference point. The marker was removed for subsequent planar acquisitions. Early planar acquisitions were commenced fifteen minutes post intravenous administration of [^{99m}Tc]MIBI, followed by the early SPECT acquisition. Late planar acquisitions were acquired two hours post-administration of [^{99m}Tc]MIBI, followed immediately by late SPECT/CT.

Planar image acquisition

All patients were provided with water to drink immediately prior to early planar acquisition in order to minimize [^{99m}Tc]MIBI salivary gland activity. Planar images were acquired using the anterior camera of a dual-headed gamma camera, positioned with minimal possible distance from the patient and a low energy high resolution parallel (LEGR) collimator. The initial acquisition with the cobalt marker at the sternal notch was terminated after 100 kilocounts had been achieved with the image matrix fixed at 128 × 128. Early (15 minutes post-injection) planar images were acquired using an image matrix of 256 × 256 and images were acquired over a fixed time frame of ten minutes. Late (two hours post-injection) planar acquisition was performed over a fixed time frame of fifteen minutes.

SPECT and SPECT/CT image acquisition

A SPECT acquisition was obtained immediately following the fifteen-minute planar acquisition with an unchanged patient position with the field of view extending from the angle of the mandible to the mediastinum. A second SPECT/CT acquisition was performed following the delayed planar acquisition in all patients. Scan parameters are outlined in Table 1.

Image processing

Images were processed on Symbia.net using manufacturer software. The early SPECT acquisition and the B30 attenuated corrected CT reconstructed images were manually fused to produce early and late SPECT/CT datasets for comparative review. Multiplanar reconstructions (axial, coronal, and sagittal) were generated for both the early and late SPECT/CT acquisitions with soft tissue CT windows applied, and all images were displayed using the 'warm

Table 1. SPECT and CT acquisition parameters

Spect acquisition parameters	CT acquisition parameters	
	Topogram	CT
M: 128 × 128	mA: 25	Effective mAs: 15 CARE dose 4D
Detectors: both	kV: 130	kV: 130
Patient orientation: head out, supine	Scan time: 0.8 s	Scan time: 12.9 s
Rotation direction: clockwise	Slice thickness: 0.6 mm	Slice thickness: 5 mm Acquisition: 16 × 1.2 mm
Degrees rotation: 180	Topogram length: 512 mm	Pitch: 0.8
Number of views: 32	Tube position: top	Rotation time: 0.6 s
Time per view: 25 s		Scan delay: 3 s
Detector configuration: 180		CTDIvol: 1.68 mGy
Orbit: non-circular		
Mode: step and shoot		

CT — computed tomography; kV — kilovolt; mA — milliamperes; mGY — milligray; M — matrix; SPECT — single-photon emission computed tomography

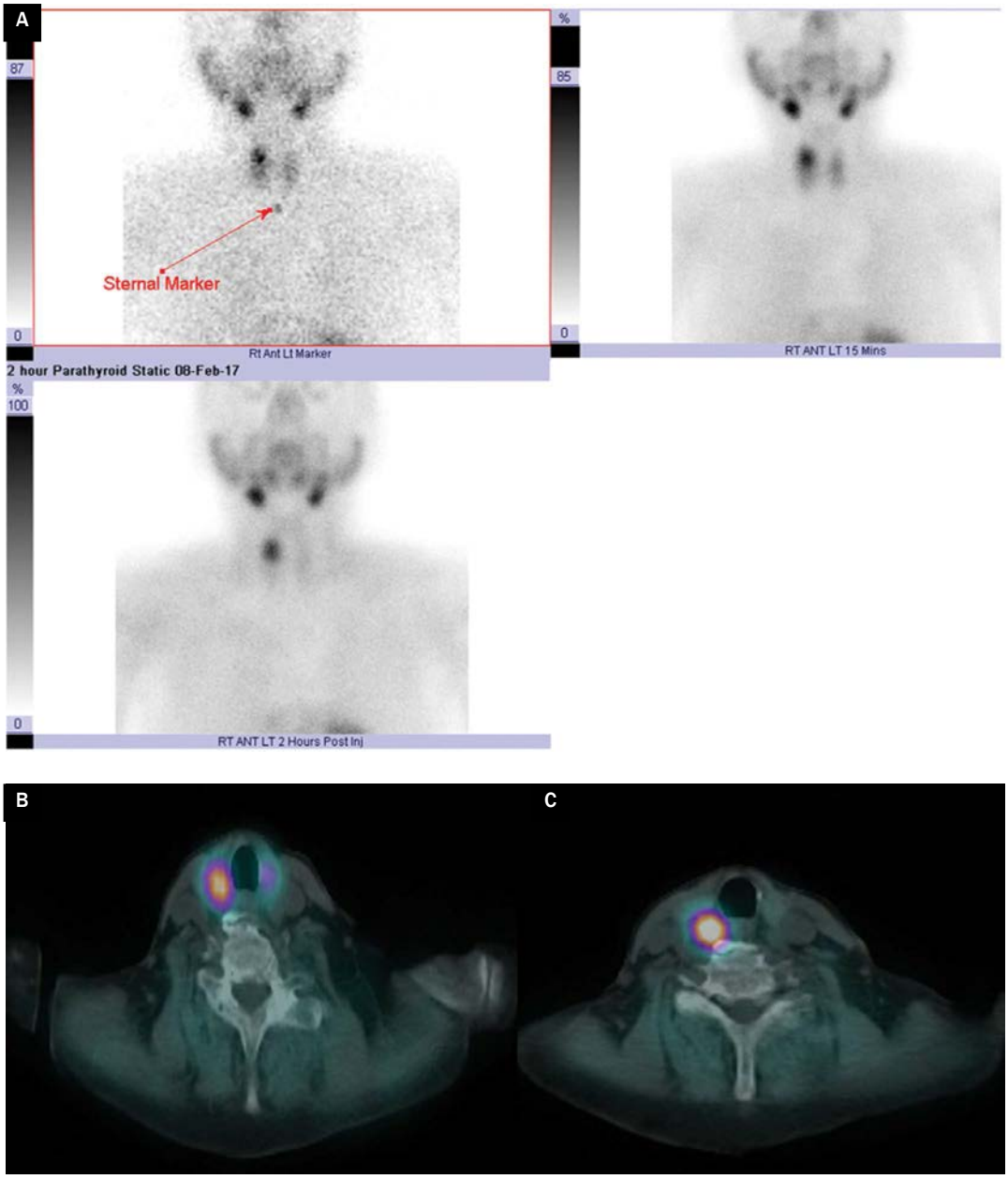

Figure 1. (**A**) Early and late planar images demonstrating a solitary region of [99mTc]MIBI uptake on delayed imaging indicating the presence of a parathyroid adenoma; (**B**) Single slice from early (15 mins) and late [(**C**), 2 hours] SPECT/CT axial reconstruction on the same patient demonstrating sustained uptake of [99mTc]MIBI in the region of suspected adenoma

metal' color scheme (see figures 1, 2). However, only the axial fused dataset was used for the purpose of this study.

Image review

Data were fully anonymized prior to review on a Barco Diagnostic Imaging monitor for blinded retrospective analysis. The datasets were jointly reviewed by two experienced consultant radionuclide radiologists and consensus was achieved. Reviewers were blinded to the timing of the axial SPECT/CT dataset and did not have access to patient history, laboratory results, or previous imaging.

Planar images and fused SPECT/CT axial reconstructions for each patient were initially reviewed separately. The reviewers determined whether each set of images was positive, negative, or indeterminate for the presence of a parathyroid adenoma. They then evaluated whether the diagnosis of a parathyroid adenoma was made via the planar images alone, the SPECT/CT alone independently or in a combination. Scans were classed as indeterminate when a definitive conclusion could not be reached. A two-alternative forced-choice strategy was employed whereby indeterminate scans were classed as negative.

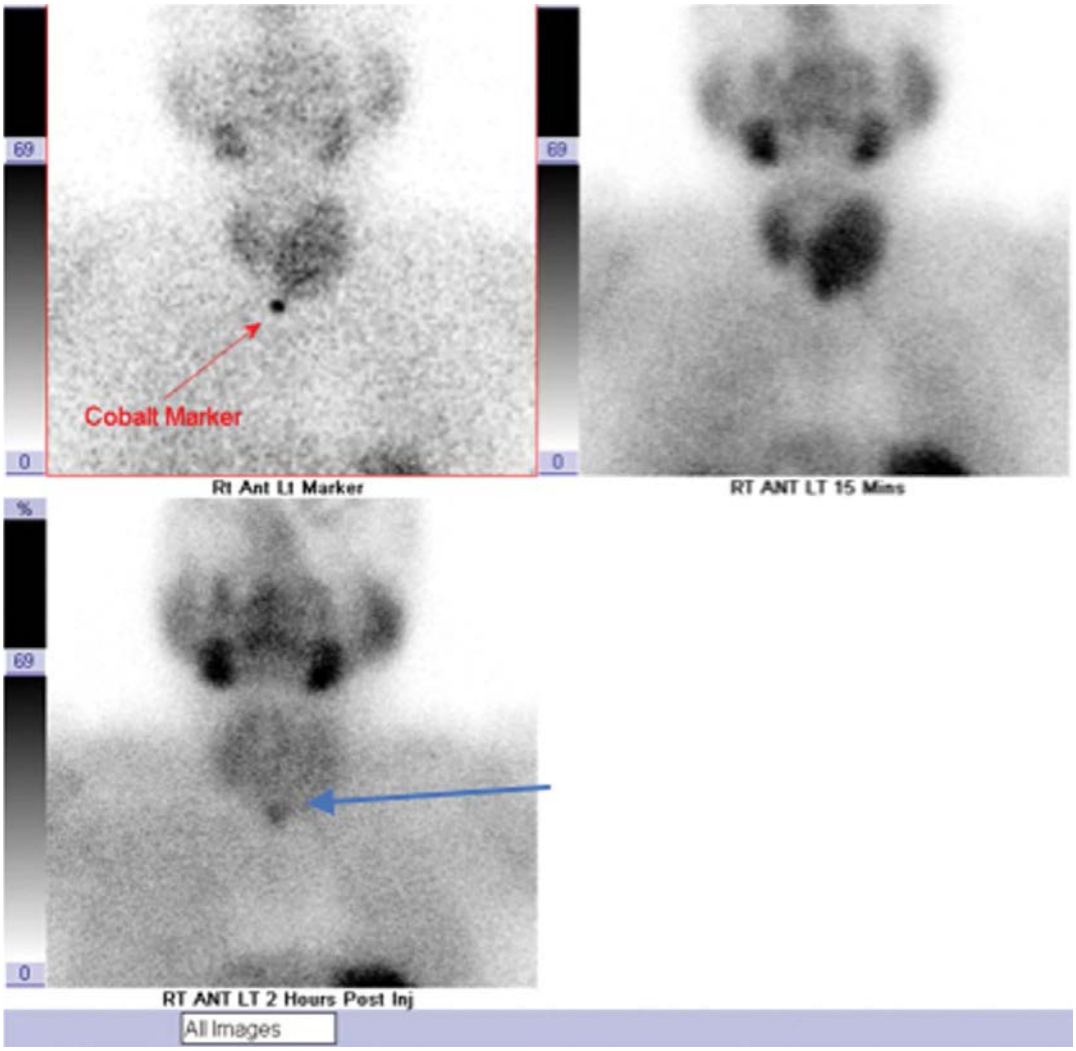

Figure 2. Planar parathyroid scintigraphy images in a patient with known multi-nodular goiter: Blue arrow indicates the presence of focally increased uptake which may represent a parathyroid adenoma or retained [^{99m}Tc]MIBI within a thyroid nodule

Statistical analysis

Data were input into a Microsoft EXCEL 2016 spreadsheet and Fisher's exact Chi-squared statistic was used to evaluate the diagnostic performances of early and late SPECT/CT and planar versus late SPECT/CT acquisition.

Results

Demographics and referral criteria

The sample population consisted of 36 patients, comprising 28 females (78%) and 8 males (22%). Age range was 24 to 83 years (mean = 59, SD 14.0).

Image analysis

In total, 21 likely parathyroid adenomas were identified within the patient sample, of which 13 were demonstrated on all sets of acquisitions. In the group comprising early planar and early SPECT/CT acquisitions:

- images were negative for the presence of parathyroid adenoma in 18 cases;
- four parathyroid adenomas were visualized on planar images only;
- one parathyroid adenoma was visualized on early SPECT/CT only;
- thirteen parathyroid adenomas were visualized on both early planar and SPECT/CT images (Tab. 2).

The Fisher's exact test found a significant difference between the diagnostic performance of early planar and SPECT/CT ($p < 0.001$). In the group consisting of late planar and SPECT/CT acquisitions:

- images were negative for the presence of parathyroid adenoma in 15 cases;
- six parathyroid adenomas were visualized on late SPECT/CT only;
- all 15 suspected parathyroid adenomas on planar images were also visualized on late SPECT/CT images (Tab. 3).

The Fisher's exact test found a significant difference between the diagnostic performance of late planar and SPECT/CT ($p < 0.001$).

Table 2. 2 × 2 contingency table comparing early planar and SPECT/CT diagnostic findings

		Early SPECT/CT		
		Negative	Positive	Total
Planar acquisition	Negative	18	1	19
	Positive	4	13	17
	Total	22	14	36

SPECT/CT — single-photon emission computed tomography/computed tomography

Table 3. 2 × 2 contingency table comparing late planar and SPECT/CT diagnostic findings

		Late SPECT/CT		
		Negative	Positive	Total
Planar acquisition	Negative	15	6	21
	Positive	0	15	15
	Total	15	21	36

SPECT/CT — single-photon emission computed tomography/computed tomography

Table 4. 2 × 2 contingency table comparing early and late SPECT/CT diagnostic findings

		Late SPECT/CT		
		Negative	Positive	Total
Early SPECT/CT	Negative	15	7	22
	Positive	0	14	14
	Total	15	21	36

SPECT/CT — single-photon emission computed tomography/computed tomography

Comparison of early and late SPECT/CT imaging protocols

Table 4 depicts the diagnostic performance of early and late SPECT/CT imaging protocols, with late SPECT/CT identifying an additional 7 adenomas not visualized within the early SPECT/CT dataset. All 14 suspected adenomas identified on early SPECT/CT were also visualized on late SPECT/CT images. The Fisher's exact test found a significant difference between the diagnostic performance of early and late SPECT/CT ($p < 0.001$).

Discussion

This study has demonstrated significantly superior performance of late-phase SPECT/CT in the identification of parathyroid adenomas with only 14 (67%) of the total of 21 suspected parathyroid adenomas demonstrated on early SPECT/CT alone.

Previous research has failed to define a single standardized imaging methodology for imaging of the parathyroid glands with evidence in support of both early and delayed SPECT/CT. Consequent implications for study duration and patient throughput underscore the need for a standardized, gold-standard, evidenced-based parathyroid imaging protocol.

Single-photon emission computed tomography/computed tomography (SPECT/CT) images have been found to be diagnostically superior to single or dual-phase planar or SPECT images [13]. Some centers perform SPECT/CT directly after early phase planar acquisition while others perform SPECT/CT following late planar acquisition, typically two hours post [99mTc]MIBI administration. Late SPECT/CT has previously been proposed as the imaging methodology of choice for improved sensitivity in the detection of parathyroid adenomas [14].

All 14 adenomas identified on early SPECT/CT imaging were also apparent on an independent review of the late SPECT/CT images, therefore omission of the early SPECT acquisition would not have altered diagnosis within the study sample.

An additional six parathyroid adenomas were reported on a review of the late SPECT/CT images that had not been identified on the review of the planar images. These findings are consistent with previous studies demonstrating the added value of SPECT/CT over planar scintigraphy in the localization of parathyroid adenomas [13].

Figure 1A–C illustrate the importance of late imaging to assess delayed retention of [99mTc]MIBI indicating the presence of a parathyroid adenoma. Delayed planar imaging after thyroid washout illustrates a single area of retained, increased focal uptake of [99mTc]MIBI suggestive of a parathyroid adenoma.

In Figure 1B, there is an uptake of [99mTc]MIBI visualized in the thyroid on early SPECT/CT acquisition. There is potential for the visualized hotspot to represent a thyroid nodule, hindering definitive diagnosis. The additional delayed SPECT/CT image (Fig. 1C) demonstrates thyroid washout of [99mTc]MIBI with retained activity suggestive of a parathyroid adenoma.

[^{99m}Tc]MIBI negative images

The sensitivity of dual-phase parathyroid scintigraphy is limited in several instances including small lesion size, multiglandular disease, and co-existing thyroid disease. Consequently, a negative dual-phase [^{99m}Tc]MIBI scan does not exclude the presence of a parathyroid adenoma. False-negative, false-positive and indeterminate findings are well recognized [3]. Although all sample patients had clinical histories suggestive of parathyroid disease, only 58% (21/36) had likely parathyroid adenomas visualized on review of the acquired images. Surgical and pathology data were not collated, precluding sensitivity and specificity analyses.

The potential for thyroidal retention of [^{99m}Tc]MIBI particularly in the presence of concurrent thyroid disease may hinder the detection of parathyroid disease. Multi-modal imaging is of benefit to confirming or out rule the presence of a parathyroid adenoma in cases where thyroid disease limits the sensitivity of a single imaging modality [15].One study patient had a notable multi-nodular goiter (Fig. 2), hindering diagnostic accuracy and underlining the limitations of parathyroid scintigraphy in this patient cohort. The sample size of 36 is relatively small however produced statistically significant results. Larger sample size would further validate the study findings.

Acquired images were reviewed concurrently with both radiologists working together rather than independently and any inter-observer variability was resolved via consensus agreement. The potential for inter-rater variability on an independent review of the images was not assessed. The implementation of a two-alternative forced-choice strategy resulted in nine indeterminate results being reclassed as negative, leading to a bias toward underdiagnosis.

The investigators had no access to the clinical history, laboratory results, pathology reports, surgical reports, official radiology reports, or further imaging undergone by the sample cohort. In the normal working environment, this information is readily available and provides increased accuracy of results within an informed clinical context.

Conclusions

We have demonstrated that delayed phase SPECT/CT is significantly superior to early SPECT/CT in the identification of likely parathyroid adenomas ($p < 0.001$). The reported potential for some parathyroid adenomas to show early washout of [^{99m}Tc]MIBI was not demonstrated.

An additional 6 likely parathyroid adenomas were identified on late SPECT/CT that was not reported on a review of the associated planar image acquisitions. Late SPECT/CT improves diagnostic accuracy over planar imaging alone ($p < 0.001$), consistent with prior research [13].

We have validated local imaging protocols and found that the practice of early (15 minutes) and late planar imaging, plus a single late phase SPECT/CT two hours post-administration of [^{99m}Tc]MIBI is the most accurate parathyroid scintigraphy protocol. This refined imaging protocol has been implemented within the Nuclear Medicine department at our institution. Elimination of the early SPECT/CT acquisition has obvious implications for decreased image processing time and storage space and reduced patient scan time by a minimum of 13 minutes, with increased patient throughput.

Conflict of interest

There are no conflicts of interest to declare.

References

1. Brown SJ, Ruppe MD, Tabatabai LS. The parathyroid gland and heart disease. Methodist Debakey Cardiovasc J. 2017; 13(2): 49–54, doi: 10.14797/mdcj-13-2-49, indexed in Pubmed: 28740581.
2. Shindo M, Lee JA, Lubitz CC, et al. The changing landscape of primary, secondary, and tertiary hyperparathyroidism: highlights from the American College of Surgeons panel, "What's new for the surgeon caring for patients with hyperparathyroidism". J Am Coll Surg. 2016; 222(6): 1240–1250, doi: 10.1016/j.jamcollsurg.2016.02.024, indexed in Pubmed: 27107975.
3. Liddy S, Worsley D, Torreggiani W, et al. Preoperative imaging in primary hyperparathyroidism: literature review and recommendations. Can Assoc Radiol J. 2017; 68(1): 47–55, doi: 10.1016/j.carj.2016.07.004, indexed in Pubmed: 27681850.
4. Kunstman JW, Udelsman R. Superiority of minimally invasive parathyroidectomy. Adv Surg. 2012; 46: 171–189, doi: 10.1016/j.yasu.2012.04.004, indexed in Pubmed: 22873039.
5. Chan RK, Ruan DT, Gawande AA, et al. Surgery for hyperparathyroidism in image-negative patients. Arch Surg. 2008; 143(4): 335–337, doi: 10.1001/archsurg.143.4.335, indexed in Pubmed: 18427019.
6. Minisola S, Cipriani C, Diacinti D, et al. Imaging of the parathyroid glands in primary hyperparathyroidism. Eur J Endocrinol. 2016; 174(1): D1–D8, doi: 10.1530/EJE-15-0565, indexed in Pubmed: 26340967.
7. Hindié E, Ugur O, Fuster D, et al. 2009 EANM parathyroid guidelines. Eur J Nucl Med Mol Imaging. 2009; 36(7): 1201–1216, doi: 10.1007/s00259-009-1131-z, indexed in Pubmed: 19471928.
8. Caveny SA, Klingensmith WC, Martin WE. Parathyroid imaging: the importance of dual-radiopharmaceutical simultaneous acquisition with 99mTc-sestamibi and 123I. J Nuclear Med Technol. 2012; 40(2): 104–110, doi: https://doi.org/10.2967/jnmt.111.098400 .
9. Erbil Y, Barbaros U, Yanik BT, et al. Impact of gland morphology and concomitant thyroid nodules on preoperative localization of parathyroid adenomas. Laryngoscope. 2006; 116(4): 580–585, doi: 10.1097/01.MLG.0000203411.53666.AD, indexed in Pubmed: 16585862.
10. Martin WH, Sandler MP, Gross MD. Thyroid, parathyroid, and adrenal gland imaging. In: Sharp PF, Gemmell HG, Murray DM. ed. Practical Nuclear Medicine 3rd edition. Springer, London 2005: 247–272.
11. Payne SJ, Smucker JE, Bruno MA, et al. Radiographic evaluation of non-localizing parathyroid adenomas. Am J Otolaryngol. 2015; 36(2): 217–222, doi: 10.1016/j.amjoto.2014.10.036, indexed in Pubmed: 25465322.
12. Monzen Y, Tamura A, Okazaki H, et al. SPECT/CT fusion in the diagnosis of hyperparathyroidism. Asia Ocean J Nucl Med Biol. 2015; 3(1): 61–65, indexed in Pubmed: 27408883.
13. Lavely WC, Goetze S, Friedman KP, et al. Comparison of SPECT/CT, SPECT, and planar imaging with single- and dual-phase (99m)Tc-sestamibi parathyroid scintigraphy. J Nucl Med. 2007; 48(7): 1084–1089, doi: 10.2967/jnumed.107.040428, indexed in Pubmed: 17574983.
14. Qiu ZL, Wu Bo, Shen CT, et al. Dual-phase (99m)Tc-MIBI scintigraphy with delayed neck and thorax SPECT/CT and bone scintigraphy in patients with primary hyperparathyroidism: correlation with clinical or pathological variables. Ann Nucl Med. 2014; 28(8): 725–735, doi: 10.1007/s12149-014-0876-z, indexed in Pubmed: 25120244.
15. Hwang SH, Rhee Y, Yun M, et al. Usefulness of SPECT/CT in parathyroid lesion detection in patients with thyroid parenchymal Tc-sestamibi retention. Nucl Med Mol Imaging. 2017; 51(1): 32–39, doi: 10.1007/s13139-016-0438-5, indexed in Pubmed: 28250856.

VIA MEDICA

Nuclear Medicine Review 2022, 25, 2: 95–100
DOI: 10.5603/NMR.a2022.0021

ISSN 1506–9680, e-ISSN 1644–4345

Original

Increased physiological [^{18}F]FDG uptake in the liver and blood pool among patients with impaired renal function

Yoichi Otomi[1], Yuta Arai[1], Maki Otomo[1], Saho Irahara[1], Kaori Terazawa[1], Michiko Kubo[1], Takashi Abe[2], Takayoshi Shinya[1], Hideki Otsuka[1], Masafumi Harada[1]

[1]Department of Radiology, Tokushima University, Tokushima City, Japan
[2]Department of Radiology, Nagoya University Hospital, Nagoya City, Japan

[Received: 13 VI 2021; Accepted: 22 VI 2022]

Abstract

Background: In the daily clinical course, the liver uptake may seem to be increased in patients with renal failure. The purpose of this study was to investigate whether or not the FDG uptake of the liver, and the FDG uptake of blood pool which is generally used as a reference site as well as liver, is increased in patients with renal failure.

Material and methods: We retrospectively analyzed 233 patients who underwent FDG positron emission tomography/computed tomography (PET/CT). Renal failure is defined as an estimated glomerular filtration rate (eGFR) < 60 mL/min/1.73 m^2. We compared the FDG uptake in the liver and mediastinal blood pool of 67 patients with impaired renal function to that in 166 patients with a normal renal function (eGFR ≥ 60 mL/min/1.73 m^2). Correlations between the liver or mediastinal blood pool FDG uptake and the eGFR were also analyzed by Spearman's correlation test.

Results: Maximum and mean standardized uptake values (SUV_{max} and SUV_{mean}, respectively) of the liver and the SUV_{mean} of the mediastinal blood pool were 3.48 ± 0.57, 2.56 ± 0.37, and 1.90 ± 0.28 in the impaired renal function group, respectively, and 3.13 ± 0.45, 2.29 ± 0.33, and 1.66 ± 0.23, in the normal group, respectively. The SUV_{max} and SUV_{mean} of the liver and SUV_{mean} of the mediastinal blood pool in the impaired renal function group were significantly higher than those in the normal group ($p < 0.001$, < 0.001, and < 0.001, respectively). The SUV_{max} and SUV_{mean} of the liver and SUV_{mean} of the mediastinal blood pool of patients showed a significant negative correlation with the eGFR (Spearman's $p = -0.25$, -0.30, and -0.40, respectively, each $p < 0.001$).

Conclusions: FDG uptake in both the liver and mediastinal blood pool was higher in patients with impaired renal function.

KEY words: renal failure; eGFR; liver; mediastinal blood pool; FDG

Nucl Med Rev 2022; 25, 2: 95–100

Introduction

[^{18}F] fluoro-2-deoxyglucose (FDG) positron emission tomography/computed tomography (PET/CT) is a hybrid imaging method clinically used as an effective, non-invasive imaging tool for assessing various neoplastic diseases [1–4]. In the clinical course, both the visual assessment of FDG uptake in the tumor and the quantitative assessment of FDG uptake in the tumor lesions are performed using the standardized uptake values (SUV) [5, 6]. During the assessment of tumor uptake in malignant lymphoma, the liver and blood pool of the mediastinum are used as reference sites [7–9]. In daily clinical use, the liver uptake appears to be increased in patients with impaired renal function. Given that the FDG uptake in the liver and mediastinal blood pool is often used as a reference region for evaluating the tumor activity, it is important to understand the influencing factors. This study aimed to clarify if the FDG uptake in the liver and mediastinal blood pool in patients with impaired renal function is increased compared to that in patients with normal renal function.

Correspondence to: Yoichi Otomi, Department of Radiology, Tokushima University, 3-18-15 Kuramoto-cho, Tokushima City, Tokushima Prefecture, 770-8503, Japan, phone: +81886337173, fax: +81886337468, e-mail: otomi.yoichi@tokushima-u.ac.jp

Table 1. Clinical characteristics of the study groups

	Patients with impaired renal function (eGFR < 60 mL/min/1.73 m^2; n = 67)	Patients with normal renal function (eGFR ≥ 60 mL/min/1.73m^2; n = 166)	p-value
Age [years]	70.8 ± 10.2	66.3 ± 13.2	0.006*
Gender			0.810
Female	29	69	
Male	38	97	
Weight [kg]	58.8 ± 12.1	55.1 ± 10.7	0.021*
Blood glucose [mg/dL]	104.4 ± 13.5	103.8 ± 13.2	0.752
FDG [MBq]	182.8 ± 40.1	170.8 ± 37.8	0.033*
eGFR [mL/min/1.73 m^2]	45.3 ± 11.3	78.1 ± 13.9	< 0.001*
GOT (IU/L) [13–30]	21.8 ± 7.9	21.2 ± 6.5	0.547
GPT (IU/L) [7–23]	16.7 ± 10.8	15.8 ± 7.0	0.509
T-Bil (mg/dL) [0.4–1.5]	0.69 ± 0.27	0.66 ± 0.24	0.514
Alb (g/dL) [4.0–5.2]	3.9 ± 0.5	3.9 ± 0.5	0.967
TP (g/dL) [6.5–8.0]	6.9 ± 0.6	7.0 ± 0.5	0.113

*Data are represented as the mean ± standard deviation; A p-value < 0.05 was considered statistically significant; FDG — fluorodeoxyglucose; eGFR — estimated glomerular filtration rate; GOT — glutamic oxaloacetic transaminase; GPT — glutamic pyruvic transaminase; T-Bil — total bilirubin; Alb — albumin; TP — total protein

Material and methods

Procedures and population

This retrospective study was approved by the Ethics Committee of Tokushima University Hospital (approval number: 3210). The need for written informed patient consent was waived due to the study's retrospective design. All methods were carried out in accordance with relevant guidelines and regulations. We identified retrospectively patients who underwent FDG PET/CT from January 2018 to June 2018 and who had renal function test values measured within one month of the FDG PET/CT.

We excluded patients with a history of primary liver tumor, liver metastasis, or liver invasion; liver mass lesion detectable on PET/CT; suspected cirrhosis; fatty liver (less than 40 Hounsfield units on CT); diabetes mellitus; blood glucose level of 140 mg/dL or higher before FDG injection; and PET/CT within 3 months of chemotherapy, radiation therapy, or a surgical procedure. Finally, 233 patients (male, n = 135; female, n = 98; mean age, 67.6 years) were included in this study.

The KDIGO CKD Work Group clinical practice guidelines define chronic kidney disease as decreased kidney function shown by a glomerular filtration rate of < 60 mL/min/1.73 m^2, kidney damage markers, or both of at least three months duration, regardless of the underlying cause [10]. Based on this guideline, patients with an estimated glomerular filtration rate (eGFR) of < 60 mL/min/1.73 m^2 were suspected of having, CKD. We used that definition to identify patients with impaired renal function.

We compared the FDG uptake in the liver and mediastinal blood pool of 67 patients with impaired renal function to that in 166 patients with normal renal function (eGFR ≥ 60 mL/min/1.73 m^2). Liver function test values (glutamic oxaloacetic transaminase [GOT], glutamic pyruvic transaminase [GPT], and total bilirubin [T-Bil]), renal function test values (eGFR) and serum albumin and total protein measured within one month of the FDG PET/CT were compared between these groups. Correlations between eGFR and, individually, the liver uptake and mediastinal blood pool uptake were also calculated.

The evaluation of the FDG uptake in the liver and mediastinal blood pool of the study group

PET/CT images were retrospectively evaluated using the image viewer (AW server 2.0; GE Healthcare, Milwaukee, WI, USA) by board-certified nuclear medicine physicians. The maximum and mean standardized uptake values (SUV_{max} and SUV_{mean}) of the liver and SUV_{mean} of the mediastinal blood pool were calculated. The SUV_{max} and SUV_{mean} of the liver were calculated by automatically setting a volume of interest (VOI) in the liver of the study group using AW server 2.0 [5]. For the mediastinal blood pool SUV_{mean}, a 1-cm-diameter spherical VOI was set in the descending aorta to not overlap with the blood vessel wall [11].

Statistical analyses

Data are expressed as the mean ± standard deviation. The homogeneity of variance was assessed using Levene's test. The Kolmogorov–Smirnov test was used to determine which variables were normally distributed. For normally distributed variables, differences in the parameter variables were evaluated using Student's t-test, whereas non-normally distributed variables were evaluated using Welch's t-test. We quantified the relationship between liver and blood pool uptake and eGFR using Spearman's correlation analysis. Statistical analyses were performed using the SPSS Statistics software program (version 24; IBM, Chicago, IL, USA). A p-value of less than 0.05 was considered statistically significant.

Results

A comparison of the clinical characteristics related to PET/CT and the liver function test data, serum albumin, and total protein of the patients with impaired renal function and the data of those with normal renal function are shown in Table 1. While each group's mean serum albumin was slightly lower than the normal limit, the mean serum GOT, GPT, T-Bil, and total protein levels of each group were within the normal ranges. A comparison of the liver and mediastinal blood uptake data of the patients with impaired renal function and the data of those with normal renal function are shown in Table 2.

Table 2. Comparison of the FDG uptake in the liver and mediastinal blood between patients with impaired renal function and normal renal function levels

Parameter	Patients with impaired renal function (eGFR < 60 mL/min/1.73 m^2; n = 67)	Patients with normal renal function (eGFR ≥ 60 mL/min/1.73 m^2; n = 166)	p-value
Liver			
SUV_{max}	3.48 ± 0.57	3.13 ± 0.45	< 0.001*
SUV_{mean}	2.56 ± 0.37	2.29 ± 0.33	< 0.001*
Blood pool			
SUV_{mean}	1.90 ± 0.28	1.66 ± 0.23	< 0.001*

*Data are represented as the mean ± standard deviation; A p-value < 0.05 was considered statistically significant; eGFR — estimated glomerular filtration rate; SUV_{max} — maximum standardized uptake value; SUV_{mean} — mean standardized uptake value

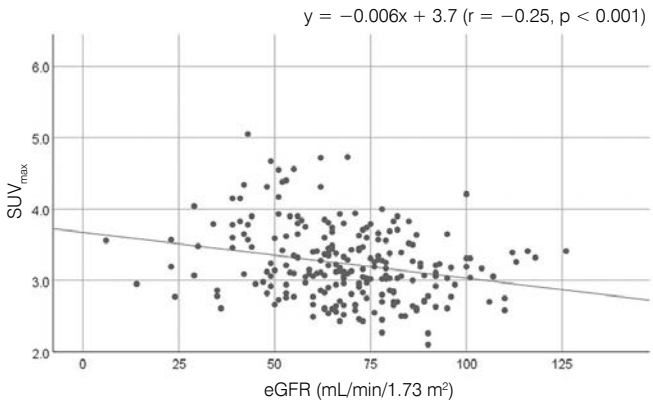

Figure 1. The correlation between eGFR and the liver SUV_{max}, eGFR demonstrated a significantly negative but weak correlation with the liver SUV_{max}, showing a regression line of y = –0.006x + 3.7 (r = –0.25, p < 0.001)

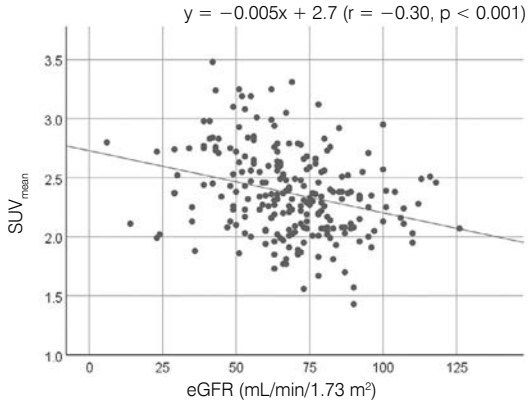

Figure 2. The correlation between eGFR and liver SUV_{mean}, eGFR demonstrated a significantly negative but weak correlation with the liver SUV_{mean}, showing a regression line of y = –0.005x + 2.7 (r = –0.30, p < 0.001)

The SUV_{max} and SUV_{mean} of the liver and the SUV_{mean} of the mediastinal blood pool in the impaired renal function group were 3.48 ± 0.57, 2.56 ± 0.37, and 1.90 ± 0.28, respectively; these values in the normal group were 3.13 ± 0.45, 2.29 ± 0.33, and 1.66 ± 0.23, respectively. The SUV_{max} and SUV_{mean} of the liver and SUV_{mean} of the mediastinal blood pool (p < 0.001, < 0.001, and < 0.001, respectively) were significantly different between the two groups. The eGFR had a negative, but weak, correlation with liver SUV_{max}, with a regression line of y = −0.006x + 3.7 (r = −0.25, p < 0.001) (Fig. 1). Furthermore, eGFR had a similar negative, but weak, correlation with the liver SUV_{mean}, with a regression line of y = −0.005x + 2.7 (r = −0.30, p < 0.001) (Fig. 2). The eGFR had a negative and moderate correlation, which was significant, with the SUV_{mean} of the mediastinal blood pool, with a regression line of y = −0.005x + 2.1 (r = −0.40, p < 0.001) (Fig. 3). Figure 4 shows the representative PET/CT images of a patient with impaired renal function, showing increased liver and mediastinal blood uptake. Figure 5 shows the representative PET/CT images of a patient with a normal renal function level.

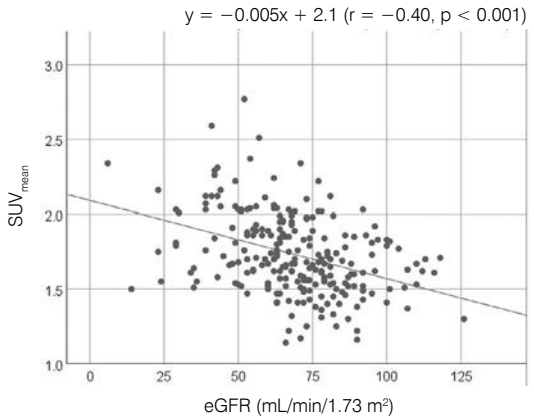

Figure 3. The correlation between eGFR and the SUV_{mean} of the mediastinal blood pool. eGFR demonstrated a significantly negative and moderate correlation with the SUV_{mean} of the mediastinal blood pool, showing a regression line of y = –0.005x + 2.1 (r = –0.40, p < 0.001)

Discussion

The SUV_{max} and SUV_{mean} of the liver and SUV_{mean} of the mediastinal blood pool in the impaired renal function group were significantly higher than those in the normal group. The eGFR showed a weak but significant negative correlation with the liver SUV_{max} and SUV_{mean}. Furthermore, eGFR was significantly negatively correlated with the SUV_{mean} of the mediastinal blood pool. There is no consensus on the FDG uptake in the liver and blood pool in patients with impaired renal function. A previous study stated that 12 patients with impaired renal function (eGFR < 60 mL/min) exhibited no significant differences in FDG uptake in the liver and

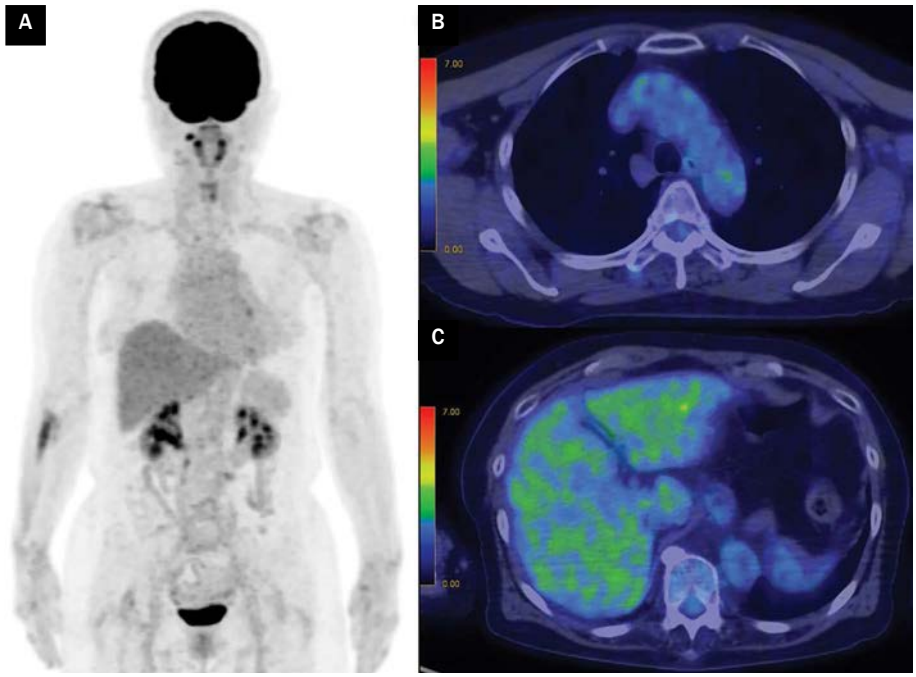

Figure 4. PET/CT image of a representative case with impaired renal function showing increased liver and mediastinal blood uptake. Maximum intensity projection of FDG PET (**A**), PET/CT fusion image of mediastinal blood pool (**B**), PET/CT fusion image of liver (**C**) of a 70-year-old female patient with impaired renal function (eGFR: 48 mL/min/1.73 m^2). Parameters of interest were as follows: SUV_{max} of 4.3, SUV_{mean} of 2.8 in liver, SUV_{mean} of 1.9 in mediastinal blood pool

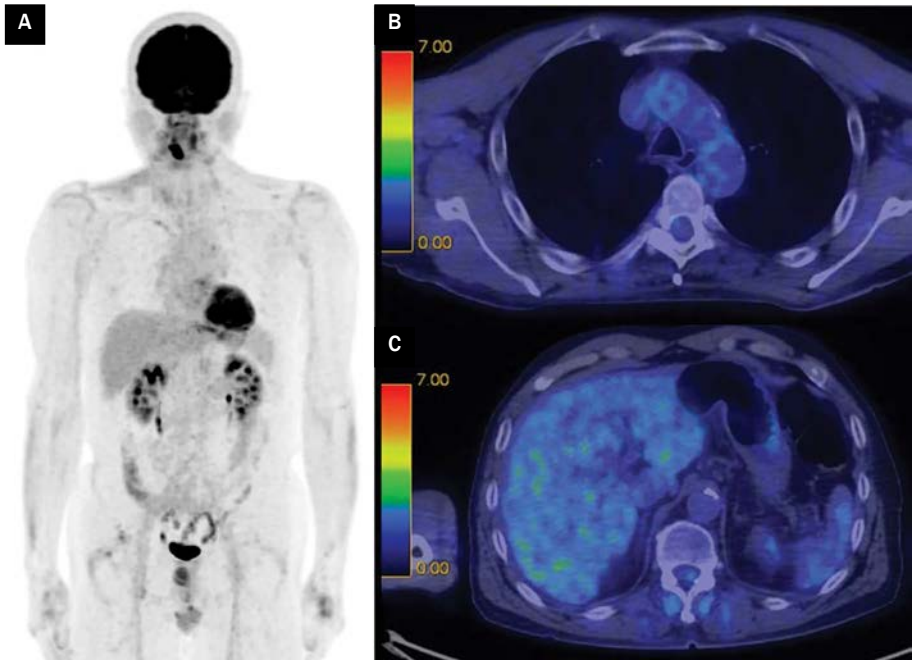

Figure 5. PET/CT image of a representative case with normal renal function. Maximum intensity projection of FDG PET (**A**), PET/CT fusion image of mediastinal blood pool (**B**), PET/CT fusion image of liver (**C**) of a 60-year-old male patient with normal renal function (eGFR: 79 mL/min/1.73 m^2). Parameters of interest were as follows: SUV_{max} of 3.0, SUV_{mean} of 2.1 in liver, SUV_{mean} of 1.6 in mediastinal blood pool

blood pool compared with patients with normal renal function [12]. Another study reported that FDG uptake in the liver in 30 patients with impaired renal function was higher than in patients with normal renal function; however, there was no significant difference (liver SUV_{max} 2.90 *vs.* 2.60, respectively. p=0.62) [13]. Lastly, a paper reported that the SUV_{mean} of the left atrium as a cardiac blood pool in 20 patients with impaired renal function and a blood serum creatinine level over 1.1 mg/dL was significantly higher than that in

20 healthy volunteers (SUV_{mean} 1.5 ± 0.2 *vs.* 1.3 ± 0.1, respectively $p < 0.05$) [14]. This same study also reported that the SUV_{mean} of the liver in patients with impaired renal function was higher than in healthy volunteers, but not significant (SUV_{mean} 1.8 ± 0.4 *vs.* 1.7 ± 0.3, respectively). The present article is the first report which showed uptakes in both the liver and the mediastinal blood pool in the impaired renal function group were significantly higher than those in the normal group. Our study included more patients than did previous studies, strengthening the level of evidence.

The potential explanation for why the uptake in the liver and mediastinal blood pool is significantly higher in patients with impaired renal function is thought to be that radiopharmaceuticals (FDG) remain in the blood because of lower renal metabolism and less urinary excretion in patients with impaired renal function. Therefore, the uptake in the blood pool becomes slightly higher. Since many blood vessels are stretched in the liver, it is considered that the uptake in the liver becomes slightly higher if there is a relatively higher concentration in the blood.

In this study, no strong effect of renal function decline on the liver uptake and blood pool uptake was observed; however, uptake in these sites in the impaired renal function group was significantly higher than in the normal group. The target tumor lesion is usually compared with the normal uptake in the surrounding background or by referencing the uptake in the mediastinal blood pool or the liver [15, 16]. It may be necessary to recognize impaired renal function as one factor which affects the liver and blood pool uptake and its use as the reference.

Some factors that can affect liver uptake in FDG PET/CT have been previously reported. Abele et al. [17] reported that on CT there was no association between liver attenuation and liver SUV_{mean}. On the other hand, Keramida et al. [18] reported increased FDG uptake into fatty liver. Liu et al. [19] reported that moderate fatty liver positively affected liver FDG uptake, while severe fatty liver negatively affected it. Patients with fatty liver were excluded from the present study. It has been reported that hypoglycemia appeared to reduce liver and blood pool activity [20]. In our study, no significant difference in blood sugar level between patients with normal renal function and impaired renal function was observed. It also has been reported that the liver SUV_{max} and SUV_{mean} of patients with hypoalbuminemia derived from malnutrition were significantly lower than those of individuals with normal serum albumin levels [21]. In this study, no significant difference in the serum albumin and total protein level between patients with impaired renal function and normal renal function was observed; hence, the effect of hypoalbuminemia on hepatic uptake seemed almost negligible.

Our study has a few limitations. First, the retrospective study design may predispose to selection bias. Second, the VOI was set when measuring liver uptake, and it is possible that the VOI might contain hidden liver lesions. Patients with detectable liver lesions were excluded from the analysis in this study. However, our study may still have included patients with small cystic lesions, liver hemangiomas, vascular abnormalities such as intrahepatic portosystemic shunts, undetectable hepatocellular carcinomas, or liver metastases with low FDG uptake. Third, several clinical features between the study groups were inconsistent. There were significant differences in age, body weight, and FDG injection dose between patients with impaired renal function and those with normal renal function. These factors may have affected liver uptake. However, despite these limitations, this is the first report to note a significant increase in FDG uptake in both the liver and blood pool, which could be attributed to impaired renal function. The FDG uptake in the liver and blood pool may appear slightly higher in patients with impaired renal function; we confirmed that this trend existed. The increased FDG uptake in the liver or blood pool, which was generally used as the reference site for evaluating tumor uptake, could influence the assessment of therapeutic efficacy. As the number of patients with impaired renal function and the usefulness of PET/CT increase, it is important to understand and appropriately deal with various factors that affect PET images to avoid an inaccurate interpretation. Further studies are needed to confirm the adequacy of referencing to the liver and blood pool in patients with impaired renal function.

Conclusions

Increased liver uptake and mediastinal blood pool uptake on FDG PET/CT is associated with impaired renal function, which seems to be a factor associated with increased liver uptake and mediastinal blood pool uptake. Renal function (eGFR) was found to be significantly negatively correlated with both the liver and mediastinal blood pool uptake.

Acknowledgments

We would like to thank Editage (www.editage.com) for English language editing.

Funding

No funding was received.

Conflict of interest

The authors declare no competing interests.

References

1. Strauss LG, Conti PS. The applications of PET in clinical oncology. J Nucl Med. 1991; 32(4): 623–648, indexed in Pubmed: 2013803.
2. Hawkins RA, Hoh CK. PET FDG studies in oncology. Nuclear Medicine and Biology. 1994; 21(5): 739–747, doi: 10.1016/0969-8051(94)90045-0, indexed in Pubmed: 9241650.
3. Hoh CK, Hawkins RA, Glaspy JA, et al. Cancer detection with whole-body PET using 2-[18F]fluoro-2-deoxy-D-glucose. J Comput Assist Tomogr. 1993; 17(4): 582–589, doi: 10.1097/00004728-199307000-00012, indexed in Pubmed: 8331230.
4. Ali SA, Amin DH, Abdelkhalek YI. Efficiency of whole-body 18F-FDG PET CT in detecting the cause of rising serum AFP level in post-therapeutic follow-up for HCC patients. Jpn J Radiol. 2020; 38(5): 472–479, doi: 10.1007/s11604-020-00930-8, indexed in Pubmed: 32078123.
5. Wahl RL, Jacene H, Kasamon Y, et al. From RECIST to PERCIST: Evolving Considerations for PET response criteria in solid tumors. J Nucl Med. 2009; 50 Suppl 1: 122S–50S, doi: 10.2967/jnumed.108.057307, indexed in Pubmed: 19403881.
6. Zasadny KR, Wahl RL. Standardized uptake values of normal tissues at PET with 2-[fluorine-18]-fluoro-2-deoxy-D-glucose: variations with body weight and a method for correction. Radiology. 1993; 189(3): 847–850, doi: 10.1148/radiology.189.3.8234714, indexed in Pubmed: 8234714.

7. Meignan M, Gallamini A, Meignan M, et al. Report on the First International Workshop on Interim-PET-Scan in Lymphoma. Leuk Lymphoma. 2009; 50(8): 1257–1260, doi: 10.1080/10428190903040048, indexed in Pubmed: 19544140.
8. Barrington SF, Kluge R. FDG PET for therapy monitoring in Hodgkin and non-Hodgkin lymphomas. Eur J Nucl Med Mol Imaging. 2017; 44(Suppl 1): 97–110, doi: 10.1007/s00259-017-3690-8, indexed in Pubmed: 28411336.
9. Zijlstra JM, Burggraaff CN, Kersten MJ, et al. FDG-PET as a biomarker for early response in diffuse large B-cell lymphoma as well as in Hodgkin lymphoma? Ready for implementation in clinical practice? Haematologica. 2016; 101(11): 1279–1283, doi: 10.3324/haematol.2016.142752, indexed in Pubmed: 27799345.
10. Eknoya GE, Lameire N. Kidney Disease: Improving Global Outcomes (KDIGO) CKD Work Group. KDIGO 2012 Clinical practice guideline for the evaluation and management of chronic kidney disease. Kidney Int Suppl. 2013; 3: 1–150.
11. Furuya S, Manabe O, Ohira H, et al. Which is the proper reference tissue for measuring the change in FDG PET metabolic volume of cardiac sarcoidosis before and after steroid therapy? EJNMMI Res. 2018; 8(1): 94, doi: 10.1186/s13550-018-0447-8, indexed in Pubmed: 30291527.
12. Akers SR, Werner TJ, Rubello D, et al. 18F-FDG uptake and clearance in patients with compromised renal function. Nucl Med Commun. 2016; 37(8): 825–832, doi: 10.1097/MNM.0000000000000513, indexed in Pubmed: 27058366.
13. Kode V, Karsch H, Osman MM, et al. Impact of Renal Failure on F18-FDG PET/CT Scans. Front Oncol. 2017; 7: 155, doi: 10.3389/fonc.2017.00155, indexed in Pubmed: 28785537.
14. Minamimoto R, Takahashi N, Inoue T. FDG-PET of patients with suspected renal failure: standardized uptake values in normal tissues. Ann Nucl Med. 2007; 21(4): 217–222, doi: 10.1007/s12149-007-0012-4, indexed in Pubmed: 17581720.
15. Ziai P, Hayeri MR, Salei A, et al. Role of optimal quantification of FDG PET imaging in the clinical practice of radiology. Radiographics. 2016; 36(2): 481–496, doi: 10.1148/rg.2016150102, indexed in Pubmed: 26963458.
16. Ambrosini V, Fanti S, Chengazi VU, et al. Diagnostic accuracy of FDG PET/CT in mediastinal lymph nodes from lung cancer. Eur J Radiol. 2014; 83(8): 1301–1302, doi: 10.1016/j.ejrad.2014.04.035, indexed in Pubmed: 24917223.
17. Abele JT, Fung CI. Effect of hepatic steatosis on liver FDG uptake measured in mean standard uptake values. Radiology. 2010; 254(3): 917–924, doi: 10.1148/radiol.09090768, indexed in Pubmed: 20177102.
18. Keramida G, Potts J, Bush J, et al. Accumulation of (18)F-FDG in the liver in hepatic steatosis. AJR Am J Roentgenol. 2014; 203(3): 643–648, doi: 10.2214/AJR.13.12147, indexed in Pubmed: 25148170.
19. Liu G, Li Y, Hu P, et al. The combined effects of serum lipids, BMI, and fatty liver on 18F-FDG uptake in the liver in a large population from China: an 18F-FDG-PET/CT study. Nucl Med Commun. 2015; 36(7): 709–716, doi: 10.1097/MNM.0000000000000301, indexed in Pubmed: 25757200.
20. Sarikaya I, Sarikaya A, Sharma P. Assessing the effect of various blood glucose levels on F-FDG activity in the brain, liver, and blood pool. J Nucl Med Technol. 2019; 47(4): 313–318, doi: 10.2967/jnmt.119.226969, indexed in Pubmed: 31182660.
21. Otomi Y, Otsuka H, Terazawa K, et al. A reduced liver F-FDG uptake may be related to hypoalbuminemia in patients with malnutrition. Ann Nucl Med. 2019; 33(9): 689–696, doi: 10.1007/s12149-019-01377-2, indexed in Pubmed: 31201673.

VIA MEDICA

Nuclear Medicine Review 2022, 25, 2: 101–104
DOI: 10.5603/NMR.a2022.0022

ISSN 1506–9680, e-ISSN 1644–4345

Original

Preoperative detection of sentinel lymph node in patients with endometrial cancer — comparison of planar lymphoscintigraphy, SPECT and SPECT/CT

Anamarija Jankulovska[1], Bojana Stoilovska Rizova[1], Nikolina Bozhinovska[1], Aleksandra Peshevska[1], Mile Tanturovski[2], Igor Aluloski[2], Sasho Stojcevski[2], Nevena Manevska[1], Sinisa Stojanoski[1], Daniela Miladinova[1]

[1]Institute of Pathophysiology and Nuclear Medicine, Faculty of Medicine, University "Ss Cyril and Methodius", Skopje, North Macedonia
[2]University Clinic for Obstetrics and Gynecology, Skopje, North Macedonia

[Received 20 X 2021; Accepted 22 VI 2022]

Abstract

Background: Sentinel lymph node (SLN) mapping allows minimal invasive assessment of lymph node status in patients with early-stage endometrial cancer (EC). Intraoperative detection of SLNs is based on the results obtained from preoperative nuclear medical images. The purpose of this study was to compare the data obtained from planar lymphoscintigraphy (PL), single-photon emission computed tomography (SPECT), and SPECT with computed tomography (SPECT/CT) for preoperative SLN detection in patients with EC.

Material and methods: A total of 44 images in 22 patients with early-stage EC (22 PL, 9 SPECT and 13 SPECT/CT) were analyzed. The scans were performed in the period 2018–2020 at the Institute of Pathophysiology and Nuclear Medicine in Skopje. Thirteen patients underwent PL and SPECT/CT and nine patients underwent PL and SPECT after cervical injection of 4 mCi ^{99m}Tc-SENTI-SCINT on the day of surgery. Descriptive statistics, Wilcoxon Matched Pairs Test, and Spearman rank R coefficient were used for data analyses.

Results: Twenty-two patients with mean age of 61.1 ± 7.5 and body mass index (BMI) 34.62 ± 6.4 kg/m^2 were included in the study. In four patients (18.2%) SLN was not detected on PL. Detection rate on SPECT and SPECT/CT was 100%. The average number of detected SLN was 1.4 ± 1.05, 2.2 ± 1.1 и 2.15 ± 1.1 on PL, SPECT and SPECT/CT respectively. We found a statistically significant difference in the number of detected SLNs on PL *vs.* SPECT/CT ($p = 0.0077$). The most common SLN location on SPECT/CT was the right internal iliac followed by the left common iliac region.

Conclusions: The results of the presented study indicate a higher diagnostic value of SPECT/CT in terms of SLN detection and exact anatomic localization as compared to planar lymphoscintigraphy (PL).

KEY words: sentinel lymph node; lymphoscintigraphy; SPECT/CT; endometrial cancer

Nucl Med Rev 2022; 25, 2: 101–104

Introduction

Detection of a sentinel gland or a sentinel lymph node (SLN) allows the removal of the first drainage lymph node from the region of the malignant lesion. If no malignant cells are detected in this node, it is assumed that the other lymph nodes of the same lymph path are not affected by metastatic deposits as well [1]. Detection and biopsy of a sentinel gland are part of the standard surgical protocol for assessing nodal status in patients with early-stage breast cancer and malignant melanoma [2, 3]. In recent years, the number of published data in the literature for detection of a SLN in patients with endometrial cancer (EC) has increased. The interest in introducing the SLN concept in these patients is due, above all, to the minimally invasive approach to assessing lymph node status by reducing the morbidity associated with radical lymph node dissection [4–6].

Correspondence to: Anamarija Jankulovska, Institute of Pathophysiology and Nuclear Medicine, Faculty of Medicine, University "Ss Cyril and Methodius", Mother Teresa 17, 1000 Skopje, North Macedonia, phone: +38978405778, e-mail: dr.jankulovska@gmail.com

The nuclear medicine procedure for preoperative mapping of the lymphatic drainage in EC is performed by using colloidal tracers labeled with Technetium-99m (^{99m}Tc), applied with cervical, subendometrial/peritumoral, or subserosal/myometrial injection [7]. The cervical method of tracer application is most commonly used because of the simple approach and the highest pelvic detection rate [8]. The tracer is usually administered on the day of the intervention.

Intraoperative detection of the SLN is based on the results obtained from its preoperative localization on nuclear medicine images. Conventional planar lymphoscintigraphy (PL), through dynamic and static imaging in multiple positions, provides a two-dimensional display of lymphatic drainage and the SLN. Single-photon emission computed tomography (SPECT) through the acquisition of multiple cross-sections, allows obtaining a three-dimensional image which increases the sensitivity, and in combination with computed tomography as hybrid SPECT/CT technology provides more accurate anatomical localization of the SLN [9–11]. Identification of the SLN leads to its simpler and faster detection, and also to a reduction in the extent of surgery. The aim of this study was to analyze and compare the data of the SLN in patients with early-stage EC, obtained with different techniques of nuclear medicine imaging: PL, SPECT and SPECT/CT.

Material and methods

A prospective, randomized study was conducted at the Institute of Pathophysiology and Nuclear Medicine, Faculty of Medicine "Ss. Cyril and Methodius" in Skopje, in the period March 2018––December 2020. The study analyzed a total of 44 nuclear medical images (22 PL, 9 SPECT, and 13 SPECT/CT) in 22 patients with EC in the preoperative first stage of the disease. The patients were recruited at the University Clinic for Gynecology and Obstetrics in Skopje. The study included patients with histologically verified EC (endometrioid adenocarcinoma of grade 1 and 2) at a presumed first stage of the disease (based on preoperative evaluation) T1; N0; M0. All patients have signed informed consent for the procedures and participation in the study, which was approved by the Ethics Committee of the Medical Faculty in Skopje.

Procedure

^{99m}Tc-SENTI SCINT (commercial kit of MEDI-RADIOPHARMA LTD, Hungary) was applied to all patients in the morning on the day of surgery with cervical injection in four quadrants at a depth of 5 mm: 1 mCi (37 Mbq) × 4 injections (total dose per patient 4 mCi). The application of ^{99m}Tc-SENTI SCINT was performed by a specialist in gynecology and obstetrics. After the application of the tracer, PL and SPECT were performed in 9 patients, while PL and SPECT/CT were performed in 13 patients, according to the following acquisition protocol:

— dynamic study after the application of the radiopharmaceutical (30 frames, 60 seconds per frame);
— static images for 30 minutes, 60 minutes, and 120 minutes (600 seconds/image);
— SPECT or SPECT/CT after 120–180 minutes:
  - SPECT (60 projections for 15 seconds per projection, angle per projection: 6 degrees, angle per detector: 180 degrees, matrix 128 × 128);
  - CT (matrix 512 × 512, rotation time: 1 second, cross-sectional thickness: 2.5 mm, cross-sectional distance 2.5 mm).

During the performance of the nuclear medicine methods, the principle ALARA (as low as reasonably achievable) was fully observed, i.e. the smallest dose of radiopharmaceutical was used to visualize the SLN on PL, SPECT and SPECT/CT. All static images were taken using a Mediso DHV Nucline Spirit dual-head gamma camera. SPECT and SPECT/CT were performed using the SPECT/CT camera OPTIMA NM/CT 640 GE Healthcare dual detector/4 slice CT.

After SLN identification in nuclear medicine imaging, all patients were operated at the University Clinic for Gynecology and Obstetrics in Skopje, in accordance with the operating protocols of the Clinic.

Nuclear medicine images were analyzed in terms of display of the SLN, number of SLNs, time of visualization of the SLN after application of the tracer, localization of the SLN (unilateral pelvic, bilateral pelvic, para-aortic), and pelvic localization of the SLN by anatomical regions, which is possible only on SPECT/CT.

Statistical data analysis

A database was created for statistical data processing in the statistical program SPSS for Windows 23.0. Category variables are presented by absolute and relative numbers, quantitative variables are presented by descriptive parameters (mean, SD, minimum, maximum). The detection rate of the SLN in nuclear medicine images is shown as the total detection rate (defined as the ratio between the number of patients with at least 1 detected SLN in a nuclear medicine image and the total number of subjects in the study), bilateral detection rate (defined as the ratio between the number of patients with at least 1 SLN detected in the two hemipelvic regions and the total number of participants in the study), the detection rate of PL, SPECT, SPECT/CT; total detection rate of para-aortic SLN (defined as the ratio between the number of patients with at least 1 detected SLN in the para-aortic region in nuclear medicine imaging and the total number of participants in the study).

To compare the number of SLNs among the techniques performed, a non-parametric Wilcoxon Matched pairs test was used. A non-parametric correlation test (Spearman rank R coefficient) was used to correlate age and BMI with the number of SLNs on PL and the time of onset of the SLN after application of ^{99m}Tc-SENTI-SCINT. For the level of significance, the value of $p < 0.05$ is taken.

Results

The study included a total of 22 female patients with histologically verified endometrioid adenocarcinoma (grade 1) — 7 patients, and (grade 2) — 15 patients, aged 46 to 74 years, with an average age of 61.1 ± 7.5 years. The body mass index (BMI) had an average value of 34.62 ± 6.4 kg/m^2, and ranged from 23.4 to 53.3 kg/m^2.

In 4 patients (18.2%), the SLN was not detected on the planar image. In all patients with SPECT or SPECT/CT pelvic SLNs were detected (Fig. 1). The total detection rate was 100%, bilateral detection rate was 31.81%, detection rate of PL was 81.81%, while for SPECT and SPECT/CT it was 100%. The total detection rate of para-aortic SLNs was 22.72%. On the PL, the most common finding was one SLN in 9 patients (40.9%), while on SPECT/CT the finding of two SLNs was most common, in 5 patients (38.5%). The total number

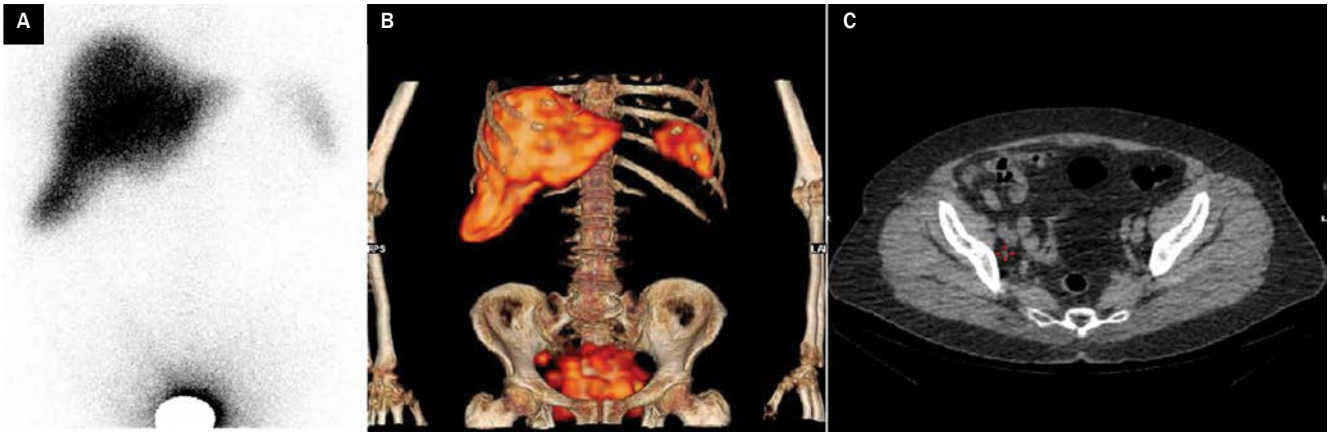

Figure 1. Planar lymphoscintigraphy (PL) and SPECT/CT in a 67-year-old patient with grade 2 endometrial adenocarcinoma; PL (**A**) did not show activity corresponding to a SLN. The fused SPECT/CT image (**B**) showed a focal accumulation in the right hemipelvic region, corresponding to two, non-enlarged lymph nodes in the right internal iliac region at the CT (**C**)

Table 1. Distribution of patients by number of detected SLNs on nuclear medicine imaging

Visualization of the SLN on a gamma camera	Number of SLNs		
	PL n (%)	SPECT n (%)	SPECT/CT n (%)
No SLN is shown	4 (18.18)		
One SLN is shown	9 (40.91)	3 (33.33)	4 (30.77)
Two SLNs are shown	6 (27.27)	2 (22.22)	5 (38.47)
Three SLNs are shown	2 (9.09)	3 (33.33)	2 (15.38)
Four SLNs are shown	1 (4.54)	1 (11.11)	2 (15.38)
Total number of shown SLNs	31	20	28

PL — planar lymphoscintigraphy; SLN — sentinel lymph node; SPECT/CT — single photon emission computed tomography/computed tomography

Table 2. Distribution of the SLNs in the pelvis by anatomical regions

Anatomical location of the SLN in the pelvis	Number of SLNs
Right obturator region	2
Left obturator region	1
Right external iliac region	2
Left external iliac region	2
Right internal iliac region	7
Left internal iliac region	1
Right common iliac region	2
Left common iliac region	6
Right para-aortic region	3

SLN — sentinel lymph node

of detected SLNs was 31 on PL, 20 on SPECT, and 28 on SPECT/CT (Tab. 1). The average number of detected SLNs was 1.4 ± 1.05, 2.2 ± 1.1, and 2.15. 1.1, respectively, on PL, SPECT, and SPECT/CT.

According to the results of the statistical analysis, the difference in the number of SLNs detected on PL and SPECT was not statistically significant (15 SLNs detected on PL *vs.* 20 SLNs detected on SPECT in 9 patients; $p = 0.068$), while the difference in the number of SLNs detected on PL and SPECT/CT was confirmed as statistically significant, for $p = 0.0077$ (16 SLNs detected on PL *vs.* 28 SLNs detected on SPECT/CT in 13 patients).The analyzed correlations between age and BMI, with the number of SLNs visualized on PL and with the time of presentation of SLNs after application of ^{99m}Tc-SENTI-SCINT, were statistically insignificant.

The most common anatomical location of the SLNs in the pelvis in the group of patients with SPECT/CT was the right internal iliac region followed by the left common iliac region (Fig. 1). Data on the anatomical location of the SLNs is shown in Table 2.

Discussion

Endometrial cancer (EC) is the sixth most commonly diagnosed cancer in women and the second most common cancer of the female genital tract in developing and underdeveloped countries. According to Global cancer statistics 2020: GLOBOCAN, there is a growing trend of EC worldwide with increasing morbidity and mortality (417,367 new cases of EC were registered in 2020, of which 97,370 ended in death) [12]. About 80 percent of diagnosed cases are in the early stages of the disease. Obesity and advanced age are significant risk factors associated with the endometrioid type of EC [13]. Our study included patients in the preoperative first stage of the disease, with histologically verified endometrioid type of adenocarcinoma, with a grade 1 and 2. A total of seven patients had EC with grade 1 and fifteen patients had EC with grade 2. The average age of patients was 61.1 ± 7.5 years, and 90% of them were over 50 years of age. These data are correlated with the already published epidemiological data in the literature [13]. Patients diagnosed at an early stage of the disease have a good prognosis, with a 5-year survival of about 90%, compared with patients with nodal metastases having a 5-year survival of about 60% [14, 15]. Nodal status is the most important prognostic factor for relapse and an indicator on which further oncological therapy is based. SLN biopsy is a minimally invasive method for determining the nodal status of patients with early-stage EC [16].

The detection rate of the SLN with cervical tracer application ranges from 67% to 85.7% for PL, and 84% to 100% for SPECT/CT (10, 17–20). The total rate of preoperative detection of the SLN

in our study was 100%, the rate of bilateral detection was 31.81%, while the individual detection rate of PL, SPECT and SPECT/CT was 81.81%, 100%, and 100% respectively. The total detection rate of para-aortic SLNs was 22.72%. The number of SLNs detected on SPECT/CT was statistically higher than the PL, which corresponds to the literature data in addition to the significantly higher detection rate of SPECT/CT [20, 21].

In 2012, Kraft and Havel [22] published a study on the impact of age and obesity on the detection rate of PL and SPECT/CT in 69 patients with gynecological tumors. The authors found that younger age was associated with a higher rate of detection of SLNs as opposed to obesity, which had no effect on the study population. The analyzed correlation between age and BMI with the number of SLNs on PL in our study was statistically insignificant.

Lymphatic drainage mapping using the nuclear medicine method for SLN visualization in the correct anatomical region enables faster and more accurate localization of the SLN with the help of the gamma detection probe. The increased sensitivity with the application of SPECT is complemented by the precise localization and morphofunctional assessment provided by SPECT/CT. In most patients, the SLN is found in the external iliac region and the obturator region [19, 23]. In our study, the precise anatomical location of the SLN was confirmed intraoperatively in all thirteen patients with SPECT/CT. The most common location was the right internal iliac followed by the left common iliac region.

Conclusions

The results of our study indicate an advantage of the SPECT/CT modality over the detection rate of planar lymphoscintigraphy or SPECT alone, greater sensitivity in detecting SLNs with low activity and precise anatomical localization. We recommend SPECT/CT as the modality of choice in the preoperative SLN mapping in patients with EC.

Conflict of interest

The authors have no conflicts of interest to declare.

References

1. Cabanas RM. The concept of the sentinel lymph node. Recent Results Cancer Res. 2000; 157: 109–120, doi: 10.1007/978-3-642-57151-0_9, indexed in Pubmed: 10857165.
2. Cardoso F, Kyriakides S, Ohno S, et al. Early breast cancer: ESMO Clinical Practice Guidelines for diagnosis, treatment and follow-up†. Ann Oncol. 2019; 30(8): 1194–1220, doi: 10.1093/annonc/mdz173, indexed in Pubmed: 31161190.
3. Swetter SM, Tsao H, Bichakjian CK, et al. Guidelines of care for the management of primary cutaneous melanoma. J Am Acad Dermatol. 2019; 80(1): 208–250, doi: 10.1016/j.jaad.2018.08.055, indexed in Pubmed: 30392755.
4. Holloway RW, Abu-Rustum NR, Backes FJ, et al. Sentinel lymph node mapping and staging in endometrial cancer: A Society of Gynecologic Oncology literature review with consensus recommendations. Gynecol Oncol. 2017; 146(2): 405–415, doi: 10.1016/j.ygyno.2017.05.027, indexed in Pubmed: 28566221.
5. Owen C, Bendifallah S, Jayot A, et al. [Lymph node management in endometrial cancer]. Bull Cancer. 2020; 107(6): 686–695, doi: 10.1016/j.bulcan.2019.06.015, indexed in Pubmed: 31648773.
6. Staley A, Sullivan SA, Rossi EC. Sentinel Lymph Node Technique in Endometrial Cancer. Obstet Gynecol Surv. 2017; 72(5): 289–295, doi: 10.1097/OGX.0000000000000425, indexed in Pubmed: 28558116.
7. Giammarile F, Bozkurt MF, Cibula D, et al. The EANM clinical and technical guidelines for lymphoscintigraphy and sentinel node localization in gynaecological cancers. Eur J Nucl Med Mol Imaging. 2014; 41(7): 1463–1477, doi: 10.1007/s00259-014-2732-8, indexed in Pubmed: 24609929.
8. Ballester M, Dubernard G, Lécuru F, et al. Detection rate and diagnostic accuracy of sentinel-node biopsy in early stage endometrial cancer: a prospective multicentre study (SENTI-ENDO). Lancet Oncol. 2011; 12(5): 469–476, doi: 10.1016/S1470-2045(11)70070-5, indexed in Pubmed: 21489874.
9. Navalkissoor S, Wagner T, Gnanasegaran G, et al. SPECT/CT in imaging sentinel nodes. ClinTransl Imaging. 2015; 3(3): 203–215, doi: 10.1007/s40336-015-0113-3.
10. Pandit-Taskar N, Gemignani ML, Lyall A, et al. Single photon emission computed tomography SPECT-CT improves sentinel node detection and localization in cervical and uterine malignancy. Gynecol Oncol. 2010; 117(1): 59–64, doi: 10.1016/j.ygyno.2009.12.021, indexed in Pubmed: 20117827.
11. Valdés Olmos RA, Rietbergen DDD, Vidal-Sicart S. SPECT/CT and sentinel node lymphoscintigraphy. ClinTransl Imaging. 2014; 2(6): 491–504, doi: 10.1007/s40336-014-0087-6.
12. Sung H, Ferlay J, Siegel RL, et al. Global cancer statistics 2020: GLOBOCAN estimates of incidence and mortality worldwide for 36 cancers in 185 countries. CA Cancer J Clin. 2021; 71(3): 209–249, doi: 10.3322/caac.21660, indexed in Pubmed: 33538338.
13. Felix AS, Weissfeld JL, Stone RA, et al. Factors associated with Type I and Type II endometrial cancer. Cancer Causes Control. 2010; 21(11): 1851–1856, doi: 10.1007/s10552-010-9612-8, indexed in Pubmed: 20628804.
14. Lajer H, Elnegaard S, Christensen RD, et al. Survival after stage IA endometrial cancer; can follow-up be altered? A prospective nationwide Danish survey. Acta Obstet Gynecol Scand. 2012; 91(8): 976–982, doi: 10.1111/j.1600-0412.2012.01438.x, indexed in Pubmed: 22548255.
15. Rajasooriyar C, Bernshaw D, Kondalsamy-Chennakesavan S, et al. The survival outcome and patterns of failure in node positive endometrial cancer patients treated with surgery and adjuvant radiotherapy with curative intent. J Gynecol Oncol. 2014; 25(4): 313–319, doi: 10.3802/jgo.2014.25.4.313, indexed in Pubmed: 25142629.
16. Concin N, Matias-Guiu X, Vergote I, et al. ESGO/ESTRO/ESP guidelines for the management of patients with endometrial carcinoma. Int J Gynecol Cancer. 2021; 31(1): 12–39, doi: 10.1136/ijgc-2020-002230, indexed in Pubmed: 33397713.
17. Collarino A, Vidal-Sicart S, Perotti G, et al. The sentinel node approach in gynaecological malignancies. Clin Transl Imaging. 2016; 4(5): 411–420, doi: 10.1007/s40336-016-0187-6, indexed in Pubmed: 27738629.
18. Naaman Y, Pinkas L, Roitman S, et al. The Added Value of SPECT/CT in Sentinel Lymph Nodes Mapping for Endometrial Carcinoma. Ann Surg Oncol. 2016; 23(2): 450–455, doi: 10.1245/s10434-015-4877-5, indexed in Pubmed: 26438438.
19. Sawicki S, Kobierski J, Łapińska-Szumczyk S, et al. Comparison of SPECT-CT results and intraoperative detection of sentinel lymph nodes in endometrial cancer. Nucl Med Commun. 2013; 34(6): 590–596, doi: 10.1097/MNM.0b013e328360d8cc, indexed in Pubmed: 23542912.
20. Kraft O, Havel M. Detection of sentinel lymph nodes in gynecologic tumours by planar scintigraphy and SPECT/CT. Mol Imaging Radionucl Ther. 2012; 21(2): 47–55, doi: 10.4274/Mirt.236, indexed in Pubmed: 23486989.
21. Togami S, Kawamura T, Yanazume S, et al. Comparison of lymphoscintigraphy and single photon emission computed tomography with computed tomography (SPECT/CT) for sentinel lymph node detection in endometrial cancer. Int J Gynecol Cancer. 2020; 30(5): 626–630, doi: 10.1136/ijgc-2019-001154, indexed in Pubmed: 32200352.
22. Kraft O, Havel M. Detection of sentinel lymph nodes by SPECT/CT and planar scintigraphy: The influence of age, gender and BMI. Journal of Biomedical Graphics and Computing. 2012; 2(2), doi: 10.5430/jbgc.v2n2p11.
23. Perissinotti A, Paredes P, Vidal-Sicart S, et al. Use of SPECT/CT for improved sentinel lymph node localization in endometrial cancer. Gynecol Oncol. 2013; 129(1): 42–48, doi: 10.1016/j.ygyno.2013.01.022, indexed in Pubmed: 23376806.

VIA MEDICA

Nuclear Medicine Review 2022, 25, 2: 105–111
DOI: 10.5603/NMR.a2022.0023

ISSN 1506–9680, e-ISSN 1644–4345

Original

Myocardial perfusion imaging single photon emission computed tomography may detect silent myocardial ischemia in patient with epilepsy

Sofia Markoula[1], Afroditi Tsoumani[1], Chainti Antonella Votti[2], Maria Beltsiou[2], Lampros Lakkas[3], Konstantinos Pappas[3], Ioannis Iakovou[4], Andreas Fotopoulos[5], Athanassios P Kyritsis[1, 2], Chrissa Sioka[2, 5]

[1]Department of Neurology, University Hospital of Ioannina, Greece
[2]Neurosurgical Institute of Ioannina, University Hospital of Ioannina, Greece
[3]Department of Cardiology, University Hospital of Ioannina, Greece
[4]Department of Nuclear Medicine, AHEPA Hospital, Aristotle University, Thessaloniki, Greece
[5]Department of Nuclear Medicine, University Hospital of Ioannina, Greece

[Received: 1 II 2022; Accepted: 22 VI 2022]

Abstract

Background: The aim of the present study was to compare the myocardial perfusion imaging (MPI) with [^{99}mTc]tetrofosmin stress — rest single-photon emission computer tomography (SPECT) of patients with epilepsy with matched control individuals.

Material and methods: All 29 adult epileptic patients were receiving antiepileptic drugs (AEDs) for epilepsy. Thirty-two individuals matched for gender and age consisted of the control group. MPIs SPECT were performed, and myocardial summed scores were obtained during stress (SSS) and rest (SRS) images. Abnormal MPI was considered when SSS was ≥ 4. In addition, the difference (SDS) between SSS and SRS was also assessed, which represents a rate of reversibility after stress.

Results: Twenty of 29 (68.97%) patients with epilepsy had abnormal MPI and 14/32 (43.75%) of the controls ($p = 0.04$). Among males, 18/23 patients and 11/25 controls had abnormal MPI ($p = 0.01$), with quite a significant difference for mean SSS between male patients and controls ($p = 0.002$). Furthermore, SDS comparison showed that irreversible abnormalities were more common in patients than in control individuals. A difference of inadequately compensated myocardial ischemia between patients treated with enzyme inducing AEDs and patients treated with valproic acid was also detected.

Conclusions: Single-photon emission computer tomography (SPECT) may detect increased risk for coronary artery disease and further cardiovascular events in patients with epilepsy. Our findings favor the conclusion that SPECT could be used for the early identification of cardiovascular comorbidity in epilepsy.

KEY words: cardiovascular disease; epilepsy; myocardial ischemia; myocardial perfusion imaging; seizures

Nucl Med Rev 2022; 25, 2: 105–111

Introduction

Cardiovascular disease represents a significant contributor to the increased mortality and hospitalized morbidity in people with epilepsy, compared with the general population [1]. Myocardial infarction (MI) following seizures may occur in a variety of epileptic conditions including single or repetitive, convulsive or nonconvulsive seizures [2]. Higher prevalence of cardiovascular risk factors such as hypertension, diabetes, and high cholesterol has been reported in patients with epilepsy compared to the general population [3]. Oxidative stress circulating markers are higher in epileptic patients and may lead to atherosclerosis [4]. In addition, previous scientific reports have indicated that antiepileptic drugs (AEDs) monitor various risk factors linked to atherothrombotic disease [5].

Even though coronary angiography is the first examination performed for the diagnosis of ischemic myocardial disease,

Correspondence to: Andreas Fotopoulos,
Department of Nuclear Medicine, University Hospital of Ioannina,
1 Stavrou Niarchou Street, Ioannina 45110, Greece,
phone: +302651099377, e-mail: professor.fotopoulos@yahoo.com

alternative non-invasive cardiovascular imaging methods may be utilized, especially in cases where the symptoms and findings are controversial and inconsistent. Among them, myocardial perfusion imaging (MPI) with ^{99m}Technetium (^{99m}Tc) tetrofosmin (TF) SPECT, is probably the non-invasive modality of choice to distinguish a silent ischemic myocardial area [6].

The aim of the present study was the comparison of MPI SPECT results in patients with epilepsy to age and gender-matched control individuals and assess whether MPI SPECT could be utilized for diagnosis of early myocardial ischemia in patients with epilepsy exhibiting non-specific cardiac symptoms and having normal ECG and cardiologic examination.

Material and methods

Patients

The study patients with active epilepsy (epilepsy on AEDs or with one or more seizures in the past year or both) were followed in the Epilepsy Outpatient Clinic of our University Hospital from January 2019 to November 2019. For inclusion in the study, patients should suffer from epilepsy for over 5 years. In addition, they should have exhibited transient or persistent atypical cardiac complaints such as non-specific chest wall discomfort or shortness of breath and had normal ECG and cardiologic evaluation. The control group consisted of gender and age-matched individuals that demonstrated similar symptoms. All study participants (patients and control individuals) had no known history of coronary artery disease (CAD). In addition, patients and controls had a medical history and thorough physical examination obtained. Specifically, relevant biochemical parameters and cardiovascular risk factors were recorded (smoking, arterial hypertension, diabetes mellitus, hypercholesterolemia, and cardiovascular disease heredity). The history of family cardiovascular disease (angina pectoris, unstable angina, myocardial infarction) was assessed by questionnaire.

Among the patients with epilepsy, several data were noted such as age at the onset of epilepsy, the duration of epilepsy, and the frequency and the type of epilepsy. Moreover, the type, frequency and number of the AEDs at the time of inclusion and during the study were documented. Patients were also classified according to epilepsy type (focal/generalized and symptomatic/no symptomatic-genetic and of unknown origin), seizures type (focal without and with awareness loss/primary generalized and secondary generalized-focal with bilateral spasms), and whether their therapeutic schema included enzyme-inducing AEDs and/or valproic acid (VPA). The study was approved by the Medical Ethical Committee Section of our University General Hospital.

SPECT MPI

All study individuals, patients and controls, were subjected to ^{99m}Tc-TF-SPECT, before and after stress, according to standard protocols [7]. Single-photon emission computer tomography (SPECT) images were acquired 15–60 minutes post radiopharmaceutical injection. Images were visually evaluated by two nuclear medicine specialists, using a 17-segment polar map as previously reported [8, 9] and scoring each segment with a scale of 0 to 4, in accordance with the severity of the myocardial perfusion deficit. A SSS score ≥ 4 was indicative of myocardial ischemia. Myocardial ischemia was considered mild if the SSS was between 4 and 8, moderate if the SSS was between 9 and 13, and of a high degree when SSS was over 13 [10].

Statistical analysis

All continuous data were stated as mean ± standard deviation (± SD), whereas binary data were noted as percentages. All patients and controls were considered as having 'pathologic' MPI (MPI ≥ 4) or not. Comparisons of traits of interest between patients and controls were quantified by x^2 test for dichotomous outcome pathologic MPI and with t-test for SSS and SDS scores. Logistic regression analysis was performed to detect any potential association of age, gender and cardiovascular risk factors with MPI results between patients and controls. Mean SSS and SDS for patients and controls were also calculated. Linear regression analysis was performed to examine the impact of gender, age, and cardiovascular risk factors associated with SSS score and SDS and compare patients and controls.

In patients was epilepsy, the impact of gender, age, cardiovascular risk factors, age of epilepsy onset, epilepsy duration, epilepsy type, seizures type, AEDs number and AEDs type on the dichotomous outcome pathologic MPI was assessed with logistic regression analysis and on SSS and SDS results with linear regression analysis. All statistical tests were calculated with the SPSSv26 software.

Results

Twenty-nine patients with epilepsy (23 males, 6 females) and 32 control individuals (25 males, 7 females) were recruited for the study. The mean age of the patients was 56.2 ± 10.5 years *vs.* 55.0 ± 9.3 years for control individuals ($p = 0.58$). There were no differences in the cardiovascular risk factors between patients with epilepsy and the control group for both genders. The mean age of epilepsy onset was 30.4 (± 21.0) years, the mean duration of epilepsy was 26.4 (± 18.5) years and the mean number of AEDs receiving was 2.2 (± 1.2). (Tab. 1).

Twenty patients (68.9%) and 14 controls (43.7%) had abnormal MPI with SSS ≥ 4, $p = 0.04$. Among males, 78.2% (18/23) patients and 44% (11/25) controls had abnormal MPI ($p = 0.01$). No statistical difference was found for the female individuals. The mean SSS was 4.5 (± 2.3) for the patients and 3.1 (± 1.8) for the controls, $p = 0.01$. For males, a statistically significant difference was found for SSS scores and for SDS scores between patients and controls with $p = 0.002$ and $p = 0.02$ accordingly (Tab. 1). The logistic regression analysis did not show any association of age and cardiovascular risk factors with MPI results. The linear regression analysis did not disclose any association of gender, age and cardiovascular risk factors with the SSS and SDS scores for patients and controls.

Focusing on patients and controls with pathologic MPI, a statistically significant difference was found between male patients and controls for SDS ($p = 0.04$). The above results on SDS scores were also found by analyzing the impact of age, gender and cardiovascular risk factors with regression models. Besides the effect of gender on SDS, no other association was found (Tab. 2). No difference in the demographics, the risk factors, the characteristics of epilepsy,

Table 1. Characteristics of epilepsy patients and controls

	Patients with epilepsy		
	Total	Males	Females
Number [%]	29	23/29 (71.8)	6/29 (20.7)
Age [y] (± SD)	56.2 (10.5)	56.7 (11.4)	59.3 (7.0)
Hyperlipidemia [%]	20/29 (69)	17/23 (73.9)	3/6 (50)
Hypertension [%]	14/29 (48.3)	12/23 (52.2)	2/6 (33.3)
Smoking (%)	12/29 (41.4)	10/23 (43.5)	2/6 (33.3)
Diabetes mellitus [%]	7/29 (24.1)	5/23 (21.7)	2/6 (33.3)
CV Heredity [%]	10/29 (34.5)	7/23 (30.4)	3/6 (50)
Age of epilepsy onset, [y] (± SD)	30.4 (21.0)	31.0 (20.6)	28.3 (24.7)
Epilepsy duration, [y] (± SD)	26.4 (18.5)	25.3 (18.2)	31 (20.4)
Epilepsy type [F/G]	13/16	12/11	1/5
Epilepsy type [S/non S]	12/17	9/14	3/3
Seizures type [f/g]	4/25	1/22	3/3
Current AEDs, mean (± SD)	2.24 (1.2)	2.3 (1.2)	2.0 (1.0)
Inducers, No.	9	9	0
Inducers (AED, No.)	(CBZ:6, PH:2, PB:1)	(CBZ:6, PH:2, PB:1)	0
VPA, No.	9	7	2
Other AEDS (No.)	LEV(12), LMG (8), LCM(4), TPM(5), ESL(5), BRV(4), ZNS(3), OXC(2), CLB(2), PRP(2), PRG(2), GBP(1)	LEV(10), LMG(5) LCM(3), TPM(4), ESL(4), BRV(3), ZNS(2), OXC(2), CLB(1), PRP(2), PRG (2), GBP (1)	LEV(2), LMG(3), LCM(1), TPM(1), ESL(1), BRV(1), ZNS(1), OXC(0), CLB(1), PRP(0), PRG(0), GBP(0)
Total AEDs, mean (± SD)	3.1 (1.4)	3.1 (1.4)	3.3 (1.6)
Abnormal MPI [%]	20/29 (69)	18/23 (78.3)	2/6 (33.3)
SSS, mean (± SD)	4.5 (2.3)	5.1 (2.2)	2.5 (1.6)
SDS, mean (± SD)	2.2 (1.1)	2.4 (2.3)	1.4 (1.5)
	Control group individuals		
	Total	Males	Females
Number [%]	32	25/32 (78.1)	7/32 (21.8)
Age [y] (± SD)	55.0 (9.3)	55.1 (9.2)	54.7 (10.2)
Hyperlipidemia [%]	18/32 (56.25)	15/25 (60)	3/7 (42.9)
Hypertension [%]	21/32 (65.6)	15/25 (60)	6/7 (85.7)
Smoking (%)	15/32 (46.9)	12/25 (48)	3/7 (42.9)
Diabetes mellitus [%]	7/32 (21.9)	6/25 (24)	1/7 (14.3)
CV Heredity [%]	13/32 (40.6)	9/25 (36)	4/7 (57.1)
Abnormal MPI [%]	14/32 (43.7)	11/25 (44)	3/7 (42.9)
SSS, mean (± SD)	3.1 (1.8)	3.2 (1.6)	2.5 (1.6)
SDS, mean (± SD)	2.4 (1.7)	1.1 (1.7)	1.8 (1.7)
	p-value		
	Total (p1)	Males (p2)	Females (p3)
Number [%]		0.58	
Age [y] (± SD)	0.38	0.60	0.35
Hyperlipidemia [%]	0.22	0.23	0.61
Hypertension [%]	0.13	0.39	0.08
Smoking (%)	0.43	0.49	0.58
Diabetes mellitus [%]	0.53	0.56	0.43
CV Heredity [%]	0.45	0.50	0.61
Abnormal MPI [%]	**0.04***	**0.01***	0.58
SSS, mean (± SD)	**0.01***	**0.002***	0.86
SDS, mean (± SD)	0.06	**0.02***	0.58

*statistically significant; AED — antiepileptic drugs; BRV — brivaracetam; CBZ — carbamazepine; CLB — clobazame; CV — cardiovascular; ESL — eslicarbazepine; f — focal without and/or with loss of awareness; F — focal; g — primary generalized and secondary generalized (focal with bilateral spasms); G — generalized; GBP — gabapentin; LCM — lacosamide; LEV — levetiracetam; LMG — lamotrigine; MPI — myocardial perfusion imaging; No. — number; Non S — no symptomatic = genetic and of unknown origin; OXC — oxcarbamazepine; p(1) — comparison between the total number of patients and controls; p(2) — between the male patients and controls; p(3) — comparison between the female patients and controls; PB — phenobarbital; PH — phenytoin; PRG — pregabaline; PRP — perampanel; S — symptomatic; SD — standard deviation; SDS — summed difference score; SRS — summed rest score; SSS — summed stress score; TPM — topiramate; y — years; ZNS — zonisamide

Table 2. Patients and controls with myocardial perfusion imaging (MPI) ≥ 4

	Patients			Controls			p-value		
	Total	Males	Females	Total	Males	Females	(1)	(2)	(3)
Age [y] (± SD)	56.2 (11.2)	56.1 (11.9)	57 (0)	56.0 (5.5)	55.1 (5.1)	59.3(6.5)	0.95	0.75	0.59
Hyperlipidemia [%]	13/20 (65)	12/18 (66.6)	1/2 (50)	7/14 (50)	7/11 (63.6)	0/3 (0)	0.48	0.58	NA
Hypertension [%]	9/20 (45)	8/18 (44.4)	1/2 (50)	10/14 (71.4)	7/11 (63.6)	3/3 (100)	0.17	0.26	0.40
Smoking [%]	10/20 (50)	9/18 (50)	1/2 (50)	6/14 (42.8)	6/11 (54.5)	0/3 (0)	0.73	0.55	NA
Diabetes mellitus [%]	4/20 (20)	3/18 (16.6)	1/2 (50)	2/14 (14.2)	1/11 (0.1)	1/3 (33.3)	0.51	0.50	0.70
CV Heredity (%)	6/20 (30)	6/18 (33.3)	0/2 (0)	9/14 (64.2)	7/11 (63.6)	2/3 (66.6)	0.08	0.08	NA
SSS, mean (± SD)	5.6 (1.9)	5.8 (1.9)	4 (0)	5.0 (0.7)	4.1 (2.3)	5.3 (6.5)	0.19	0.14	0.18
SDS, mean (± SD)	2.7 (2.6)	2.7 (2.4)	2.5 (2.1)	1.8 (1.9)	1.2 (2.1)	3.6 (1.1)	0.13	**0.04***	0.57

*statistically significant; CV — cardiovascular; MPI — myocardial perfusion imaging; p(1) — comparison between the total number of patients and controls; p(2) — between the male patients and controls; p(3) — comparison between the female patients and controls; SD — standard deviation; SDS — summed difference score; SSS — summed stress score

Table 3. Epilepsy patients with myocardial perfusion imaging (MPI) ≥ 4 and MPI < 4

	MPI ≥ 4	MPI < 4	p-value
Number	20	9	
Age [y] (± SD)	56.2 (11.2)	59.6 (9.1)	0.38
Hyperlipidemia [%]	13/20 (65)	7/9 (77.7)	0.41
Hypertension [%]	9/20 (45)	5/9 (55.5)	0.45
Smoking [%]	10/20 (50)	2/9 (22.2)	0.16
Diabetes mellitus [%]	4/20 (20)	3/9 (33.3)	0.36
CV Heredity [%]	6/20 (30)	4/9 (44.4)	0.40
Age of epilepsy onset [y]	29.4 (20.9)	32.8 (22.4)	0.69
Epilepsy duration [y]	25.3 (19.0)	29 (18.1)	0.62
Epilepsy type (F/G)	7/13	6/3	0.11
Epilepsy type (S/Non S)	7/13	5/4	0.26
Seizures type (f/g)	18/2	7/2	0.36
AEDS, current number (± SD)	2.3 (1.3)	2 (1)	0.43
AEDs, total number (± SD)	3.1 (1.5)	3.2 (1.2)	0.89
nducers [%]	8 (40)	1 (11)	0.13
Valproic acid [%]	4 (20)	5 (55.5)	0.07

AED — antiepileptic drugs; CV — cardiovascular; f — focal without and/or with loss of awareness; F — focal; g — primary generalized and secondary generalized (focal with bilateral spasms); G — generalized; MPI — myocardial perfusion imaging; Non S — no symptomatic = genetic and of unknown origin; S — symptomatic; SD — standard deviation

the AEDs number, and the AEDs type (enzyme inducers and VPA) with MPI results was found between patients with MPI ≥ 4 and patients with MPI < 4 (Tab. 3).

The impact of enzyme inducers and valproic acid was also assessed. No difference was found for the presence of pathologic MPI and for SSS and SDS scores (Tab. 4). Of interest was the finding of the statistically significant difference in SDS scores between patients receiving inducers and patients receiving VPA, which favors inducers (p = 0.05).

Discussion

In the present study, we used radionuclide myocardial scanning to assess early cardiovascular disease in patients with epilepsy. Our findings suggested that patients with epilepsy have higher percentage of early cardiovascular disease compared to age and sex-matched controls. Most of the patients in the study were males and few were females. Male patients had also statistically significant pathologic MPI while the small number of females did not allow any statistical conclusion to be made.

The role of non-invasive imaging techniques in the evaluation of patients with suspected or known CAD has increased exponentially over the past decade [11]. The value of radionuclide MPI has been reported in the literature [11–13] since it represents a reliable non-invasive test for the evaluation of myocardial ischemia in various medical conditions [14–21].

Several studies reported that patients with epilepsy exhibited increased mortality from MI or increased risk of MI. Risk for premature death was three to four times higher in people with epilepsy than in the general Chinese population, much higher in young people with epilepsy, with MI myocardial among the leading putative causes of death [22]. A retrospective open cohort analysis reported that socioeconomically deprived patients with epilepsy experience high mortality and die 17 years prematurely, with cardiovascular diseases, cancer, and unintentional injuries being the most common causes of death [23]. A nationwide Danish population showed that epilepsy was linked to higher risk of MI [24], while another study

Table 4. Antiepileptic drugs (AEDs) type

	AEDs				p-value		
	Inducer	No inducer	VPA	No VPA	(1)	(2)	(3)
Age of patients with MPI ≥ 4 (±SD)	56.2 (14.6)	56.1 (9.1)	55 (20.3)	56.5 (8.8)	0.53	0.81	0.78
SSS, mean (±SD)	5.5 (2.0)	4.1 (2.4)	4.2 (1.9)	4.7 (2.5)	0.12	0.58	0.16
SDS, mean (±SD)	3.4 (2.7)	1.6 (2.1)	1.1 (2.0)	2.7 (2.5)	0.06	0.11	**0.05***

AED — antiepileptic drugs; MPI — myocardial perfusion imaging; p(1) — comparison between patients taking inducers *vs.* patients not on inducer; p(2) — comparison between patients on VPA *vs.* patients not on VPA; p(3) — comparison between patients taking inducers and patients taking VPA; SD — standard deviation; VPA — valproic acid

demonstrated that adult patients with epilepsy but no previous cardiac disease had higher risk for MI compared to patients with fracture of their lower extremity or individuals with migraine [25]. Another population-based case-control study of 1799 cases with first acute MI found that epilepsy was linked to a higher risk for MI and that there was a graded positive relation between number of hospitalizations for epilepsy and risk of MI [26]. Our study offers an alternative perspective, trying to assess patients with early cardiovascular disease using MPI SPECT. We did not manage to show that any of epilepsy characteristics, such as the age of epilepsy onset, epilepsy duration, epilepsy type, or seizures type are associated with the presence of perfusion deficits on MPI, probably due to the small number of the patients.

Several mechanisms may explain why epilepsy and cardiovascular disease tend to coexist including causal associations, shared risk factors, and those resulting from epilepsy or its treatment [1]. In patients with epilepsy, various vascular risk biomarkers that get worse could be attributed to epilepsy itself and/or its antiepileptic medications. Predictors of asymptomatic atherosclerosis in adult patients with epilepsy were assessed in a case-control study of 225 patients with epilepsy showing that the intima-media thickness (IMT) was significantly thickened in various groups of patients with epilepsy and the levels of total homocysteine (tHcy), von Willbrand factor (vWF), malondialdehyde (MDA), thiobarbituric acid reactive substances (TBARs) and Ox-LDL levels were increased [4].

An experimental PTZ-induced model in rats showed increased myocardial injury and increased incidence of vertical tachycardia episodes in myocardial ischemia, implying that seizures in epilepsy may increase ventricular arrhythmia and myocardial injury during heart attack [27]. Patients with epilepsy may have troponin I value as high as 5.5 ng/mL and 6.3 ng/mL after generalized or temporal seizures [28, 29], indicating some degree of ischemic myocardial injury due to sympathetic overactivity elicited by the generalized seizure [30, 31]. An increase in mean serum levels of heart-type fatty acid-binding protein (H-FABP), a sensitive biomarker for myocardial ischemia, has been reported in children with intractable epilepsy either in the ictal or interictal periods [32], while in patients with known CAD myocardial infarction may follow an epileptic convulsive seizure [33].

Sudden unexpected death in epilepsy (SUDEP) is a well-known phenomenon of the ongoing investigation. Sudden death may be more frequent in individuals with epilepsy which is refractory to most medications. A study in 23 patients with epileptic seizures demonstrated that 40% of them had ST-segment depression during active seizures, indicating an increased risk of cardiovascular disease in patients with frequent, not well-controlled seizures [34]. A case-control study of all SUDEP cases in Denmark showed that SUDEP cases had significant fibrosis of the myocardium, possibly related to frequent bouts of myocardial ischemia secondary to repetitive epileptic seizures, which, associated with the ictal sympathetic storm, may lead to lethal arrhythmias causing SUDEP [35].

The literature reports that various AEDs may themselves affect cardiovascular risk in patients with epilepsy [1]. The treatment with some AEDs can increase levels of cholesterol, such as carbamazepine, and lead to MI [5, 36]. VPA may cause weight gain, insulin resistance, and metabolic syndrome [5, 37] and increase the risk for MI [38], although, in comparison with carbamazepine, VPA had a reduced risk of MI [39]. In the present study, we provide some evidence the SDS scores of inadequately compensated myocardial ischemia differed between patients treated with enzyme-inducers and patients treated with VPA.

Apart from the small number of participants, other limitations of the present study include the limited number of females and lack of other information in the databases such as physical activity, alcohol intake, etc. Furthermore, no conventional coronary angiography was performed for comparison with the MPI. However, MPI is considered as acceptable noninvasive method to diagnose myocardial abnormalities compared to conventional coronary angiography [40].

Our findings demonstrate that epilepsy patients, predominantly males, with atypical cardiac symptomatology exhibit increased myocardial silent ischemia compared to control individuals with similar symptoms. In our study there was no difference in the risk factors between patients and controls, to explain the difference in MPI results, suggesting that epilepsy itself may sometimes generate an additional risk factor for cardiovascular diseases, possibly if the seizures are refractory to medications. The early identification and treatment of cardiovascular comorbidity in epilepsy deserves further attention [23].

Single-photon emission computer tomography (SPECT) may detect increased risk for coronary artery disease and further cardiovascular events in patients with epilepsy. Our findings favor the conclusion that SPECT could be used for the early identification of cardiovascular comorbidity in epilepsy. Although many studies have investigated the risk of MI in patients with epilepsy, we believe to the best of our knowledge this is the first attempt to provide some evidence for MPI SPECT use for early myocardial disease in patients with epilepsy.

Conclusions

In conclusion, SPECT MPI in patients with epilepsy may reveal increased myocardial silent ischemia. However, further clinical trials could delineate the role of MPI SPECT in the evaluation of myocardial ischemia in patients with epilepsy.

Conflict of interest

The authors have no conflicts of interest to declare.

References

1. Chen Z, Liew D, Kwan P. Excess mortality and hospitalized morbidity in newly treated epilepsy patients. Neurology. 2016; 87(7): 718–725, doi: 10.1212/WNL.0000000000002984, indexed in Pubmed: 27421539.
2. Montepietra S, Cattaneo L, Granella F, et al. Myocardial infarction following convulsive and nonconvulsive seizures. Seizure. 2009; 18(5): 379–381, doi: 10.1016/j.seizure.2008.11.004, indexed in Pubmed: 19111478.
3. Téllez-Zenteno JF, Matijevic S, Wiebe S. Somatic comorbidity of epilepsy in the general population in Canada. Epilepsia. 2005; 46(12): 1955–1962, doi: 10.1111/j.1528-1167.2005.00344.x, indexed in Pubmed: 16393162.
4. Hamed SA, Hamed EA, Hamdy R, et al. Vascular risk factors and oxidative stress as independent predictors of asymptomatic atherosclerosis in adult patients with epilepsy. Epilepsy Res. 2007; 74(2-3): 183–192, doi: 10.1016/j.eplepsyres.2007.03.010, indexed in Pubmed: 17448640.

5. Lopinto-Khoury C, Mintzer S. Antiepileptic drugs and markers of vascular risk. Curr Treat Options Neurol. 2010; 12(4): 300–308, doi: 10.1007/s11940-010-0080-y, indexed in Pubmed: 20842589.
6. Fotopoulos A, Petrikis P, Iakovou I, et al. The impact of depression and anxiety in prognosis of patients undergoing myocardial perfusion imaging with 99mTc tetrofosmin SPECT for evaluation of possible myocardial ischemia. Nucl Med Rev Cent East Eur. 2020; 23(2): 58–62, doi: 10.5603/NMR.a2020.0014, indexed in Pubmed: 33007091.
7. Verberne HJ, Acampa W, Anagnostopoulos C, et al. European Association of Nuclear Medicine (EANM). EANM procedural guidelines for radionuclide myocardial perfusion imaging with SPECT and SPECT/CT: 2015 revision. Eur J Nucl Med Mol Imaging. 2015; 42(12): 1929–1940, doi: 10.1007/s00259-015-3139-x, indexed in Pubmed: 26290421.
8. Sioka C, Nikas D, Tsoumani A, et al. Transient myocardial ischemia due to corticosteroid use in a patient with multiple sclerosis diagnosed with myocardial perfusion imaging. J Nucl Cardiol. 2021; 28(4): 1805–1808, doi: 10.1007/s12350-020-02185-2, indexed in Pubmed: 32394408.
9. Fotopoulos A, Papadimitropoulos K, Papadopoulos A, et al. Myocardial ischemia in female patients with rheumatoid arthritis assessed with single photon emission tomography-myocardial perfusion imaging. Nucl Med Rev Cent East Eur. 2019; 22(1): 8–13, doi: 10.5603/NMR.2019.0001, indexed in Pubmed: 31482536.
10. Sioka C, Moulias C, Voulgari PV, et al. Single photon emission computed tomography myocardial perfusion imaging in patients with moderate to severe psoriosissis. Nucl Med Rev Cent East Eur. 2021; 24(2): 46–50, doi: 10.5603/NMR.2021.0014, indexed in Pubmed: 34382667.
11. Schuijf JD, Poldermans D, Shaw LJ, et al. Diagnostic and prognostic value of non-invasive imaging in known or suspected coronary artery disease. Eur J Nucl Med Mol Imaging. 2006; 33(1): 93–104, doi: 10.1007/s00259-005-1965-y, indexed in Pubmed: 16320016.
12. Ogino Y, Horiguchi Y, Ueda T, et al. A myocardial perfusion imaging system using a multifocal collimator for detecting coronary artery disease: validation with invasive coronary angiography. Ann Nucl Med. 2015; 29(4): 366–370, doi: 10.1007/s12149-015-0955-9, indexed in Pubmed: 25663393.
13. Cerqueira MD, Weissman NJ, Dilsizian V, et al. Standardized myocardial segmentation and nomenclature for tomographic imaging of the heart. A statement for healthcare professionals from the Cardiac Imaging Committee of the Council on Clinical Cardiology of the American Heart Association. Circulation. 2002; 105(4): 539–542, doi: 10.1161/hc0402.102975, indexed in Pubmed: 11815441.
14. Giannopoulos S, Markoula S, Sioka C, et al. Detecting myocardial ischemia with 99m technetium-tetrofosmin myocardial perfusion imaging in ischemic stroke. Neurohospitalist. 2017; 7(4): 164–168, doi: 10.1177/1941874417704752, indexed in Pubmed: 28974994.
15. Kotsalou I, Georgoulias P, Karydas I, et al. A rare case of myocardial infarction and ischemia in a cannabis-addicted patient. Clin Nucl Med. 2007; 32(2): 130–131, doi: 10.1097/01.rlu.0000252218.04088.ff, indexed in Pubmed: 17242569.
16. Sioka C, Exarchopoulos T, Tasiou I, et al. Myocardial perfusion imaging with (99 m)Tc-tetrofosmin SPECT in breast cancer patients that received postoperative radiotherapy: a case-control study. Radiat Oncol. 2011; 6: 151, doi: 10.1186/1748-717X-6-151, indexed in Pubmed: 22067743.
17. Sioka C, Papadimitropoulos K, Michalis L, et al. Myocardial ischemia with normal coronary angiography in a chronic kidney disease patient. Cardiol J. 2019; 26(5): 620–621, doi: 10.5603/CJ.2019.0107, indexed in Pubmed: 31701518.
18. Xiao-Rong Z, Hui-Rong Z, Mei Li, et al. Risk of silent myocardial ischemia detected by single photon emission computed tomography (SPECT) among asymptomatic Chinese patients with type 2 diabetes. Medicine (Baltimore). 2019; 98(20): e15618, doi: 10.1097/MD.0000000000015618, indexed in Pubmed: 31096471.
19. Sioka C, Baldouma A, Papadopoulos A, et al. Co-Existence of depression, low bone mineral density, and vitamin d deficiency in patients with multiple sclerosis. Psychiatr Danub. 2021; 33(2): 201, indexed in Pubmed: 34185750.
20. Sioka C, Georgiou G, Katsouras C, et al. Silent severe myocardial ischemia in a past illicit drug user imaged with myocardial perfusion scintigraphy. Perfusion. 2021 [Epub ahead of print]: 2676591211028175, doi: 10.1177/02676591211028175, indexed in Pubmed: 34192980.
21. Batsi C, Gkika E, Astrakas L, et al. Vitamin D deficiency as a risk factor for myocardial ischemia. Medicina (Kaunas). 2021; 57(8): 774, doi: 10.3390/medicina57080774, indexed in Pubmed: 34440979.
22. Ding D, Wang W, Wu J, et al. Premature mortality in people with epilepsy in rural China: a prospective study. Lancet Neurol. 2006; 5(10): 823–827, doi: 10.1016/s1474-4422(06)70528-2, indexed in Pubmed: 16987728.
23. Kaiboriboon K, Schiltz NK, Bakaki PM, et al. Premature mortality in poor health and low income adults with epilepsy. Epilepsia. 2014; 55(11): 1781–1788, doi: 10.1111/epi.12789, indexed in Pubmed: 25244361.
24. Olesen JB, Abildstrøm SZ, Erdal J, et al. Effects of epilepsy and selected antiepileptic drugs on risk of myocardial infarction, stroke, and death in patients with or without previous stroke: a nationwide cohort study. Pharmacoepidemiol Drug Saf. 2011; 20(9): 964–971, doi: 10.1002/pds.2186, indexed in Pubmed: 21766386.
25. Wilson DA, Wannamaker BB, Malek AM, et al. Myocardial infarction after epilepsy onset: A population-based retrospective cohort study. Epilepsy Behav. 2018; 88: 181–188, doi: 10.1016/j.yebeh.2018.09.009, indexed in Pubmed: 30292053.
26. Janszky I, Hallqvist J, Tomson T, et al. Increased risk and worse prognosis of myocardial infarction in patients with prior hospitalization for epilepsy--the Stockholm Heart Epidemiology Program. Brain. 2009; 132(Pt 10): 2798–2804, doi: 10.1093/brain/awp216, indexed in Pubmed: 19717532.
27. Gonca E, Barut F, Şahin D. The effect of generalized seizure activity on ischemia-induced cardiac arrhythmias and myocardial injury with histopathological evaluation in anesthetized rats. Turk J Med Sci. 2018; 48(6): 1293–1301, doi: 10.3906/sag-1807-99, indexed in Pubmed: 30543084.
28. Brobbey A, Ravakhah K. Elevated serum cardiac troponin I level in a patient after a grand mal seizure and with no evidence of cardiac disease. Am J Med Sci. 2004; 328(3): 189–191, doi: 10.1097/00000441-200409000-00012, indexed in Pubmed: 15367881.
29. Chatzikonstantinou A, Ebert AD, Hennerici MG. Temporal seizure focus and status epilepticus are associated with high-sensitive troponin I elevation after epileptic seizures. Epilepsy Res. 2015; 115: 77–80, doi: 10.1016/j.eplepsyres.2015.05.013, indexed in Pubmed: 26220381.
30. Fawaz A, Nasreddine W, Makke Y, et al. Association of cardiovascular risk factors and troponin elevation after generalized tonic-clonic seizures. Seizure. 2014; 23(2): 146–150, doi: 10.1016/j.seizure.2013.11.006, indexed in Pubmed: 24326042.
31. Nass RD, Meiling S, Andrié RP, et al. Laboratory markers of cardiac and metabolic complications after generalized tonic-clonic seizures. BMC Neurol. 2017; 17(1): 187, doi: 10.1186/s12883-017-0965-4, indexed in Pubmed: 28927394.
32. El Shorbagy HH, Elsayed MA, Kamal NM, et al. Heart-type fatty acid-binding protein as a predictor of cardiac ischemia in intractable seizures in children. J Pediatr Neurosci. 2016; 11(3): 175–181, doi: 10.4103/1817-1745.193364, indexed in Pubmed: 27857782.
33. Bonmassari R, Zeni P, Spadaro R, et al. Myocardial infarction due to late stent thrombosis following epileptic convulsive seizures. J Thromb Thrombolysis. 2010; 29(4): 512–515, doi: 10.1007/s11239-009-0380-9, indexed in Pubmed: 19655091.
34. Tigaran S, Mølgaard H, McClelland R, et al. Evidence of cardiac ischemia during seizures in drug refractory epilepsy patients. Neurology. 2003; 60(3): 492–495, doi: 10.1212/01.wnl.0000042090.13247.48, indexed in Pubmed: 12578934.
35. P-Codrea Tigaran S, Dalager-Pedersen S, Baandrup U, et al. Sudden unexpected death in epilepsy: is death by seizures a cardiac disease?

Am J Forensic Med Pathol. 2005; 26(2): 99–105, indexed in Pubmed: 15897710.

36. de Chadarévian JP, Legido A, Miles DK, et al. Epilepsy, atherosclerosis, myocardial infarction, and carbamazepine. J Child Neurol. 2003; 18(2): 150–151, doi: 10.1177/08830738030180021301, indexed in Pubmed: 12693787.
37. Pylvänen V, Knip M, Pakarinen AJ, et al. Fasting serum insulin and lipid levels in men with epilepsy. Neurology. 2003; 60(4): 571–574, doi: 10.1212/01.wnl.0000048209.07526.86, indexed in Pubmed: 12601094.
38. Dregan A, Charlton J, Wolfe CDA, et al. Is sodium valproate, an HDAC inhibitor, associated with reduced risk of stroke and myocardial infarction? A nested case-control study. Pharmacoepidemiol Drug Saf. 2014; 23(7): 759–767, doi: 10.1002/pds.3651, indexed in Pubmed: 24890032.
39. Olesen JB, Hansen PR, Abildstrøm SZ, et al. Valproate attenuates the risk of myocardial infarction in patients with epilepsy: a nationwide cohort study. Pharmacoepidemiol Drug Saf. 2011; 20(2): 146–153, doi: 10.1002/pds.2073, indexed in Pubmed: 21254285.
40. Tanabe Y, Kido T, Uetani T, et al. Differentiation of myocardial ischemia and infarction assessed by dynamic computed tomography perfusion imaging and comparison with cardiac magnetic resonance and single-photon emission computed tomography. Eur Radiol. 2016; 26(11): 3790–3801, doi: 10.1007/s00330-016-4238-1, indexed in Pubmed: 26852220.

Original
Nuclear Medicine Review 2022, 25, 2: 112–118
DOI: 10.5603/NMR.a2022.0035

ISSN 1506–9680, e-ISSN 1644–4345

VIA MEDICA

Value of diffusion MRI versus [18F]FDG PET/CT in detection of cervical nodal metastases in differentiated thyroid cancer patients

Ahmed M. Shalash[1], Mai Amr Elahmadawy[2], Samia Y. Heikal[1], Ayman A. Amin[3], Ayda A. Youssef[1]
[1]Department of Diagnostic Radiology, National Cancer Institute, Cairo University, Egypt
[2]Nuclear Medicine Unit, National Cancer Institute, Cairo University, Egypt
[3]Department of surgery, National Cancer Institute, Cairo University, Egypt

[Received: 3 I 2022; Accepted: 30 VI 2022]

Abstract

Background: In differentiated thyroid cancer (DTC) patients, cervical nodal metastasis is a negative prognostic factor. Preoperative imaging plays an important role in treatment planning for nodal metastasis and recurrence.

The aim of the study is to compare the diagnostic performance of the diffusion-weighted magnetic resonance imaging (DW-MRI) and the F-18 flurodeoxyglucose positron emission computed tomography ([18F]FDG PET/CT) in detection of cervical nodal deposits in DTC patients.

Materal and methods: The study was conducted on 30 patients, each performed both modalities just before the surgery. The gold standard was the pathological specimens with post-operative clinico-radiological follow-up, to assess the diagnostic performance of each modality.

Results: Based on pathological and post-operative clinico-radiological follow up data. Sensitivity, specificity, negative predictive value (NPV), positive predictive value (PPV) and accuracy were 84%, 80%, 50%, 95% and 83% for PET/CT compared to 84%, 60%, 42.8%, 91.3% and 80% for DW-MRI.

On comparing the diagnostic performance of combined DW-MRI and PET/CT to each modality alone, the sensitivity and NPV were improved to 96% and 80% respectively.

Conclusions: [18F]FDG PET/CT study is a valuable diagnostic modality for the assessment of cervical nodal deposits in DTC patients, surpassing DW-MRI. Combined PET/CT and DW-MRI techniques seemed to have synergistic performance, mainly in terms of sensitivity and NPV, for detection of nodal metastases.

KEY words: DW-MRI; PET/CT; DTC; cervical nodal metastasis

Nucl Med Rev 2022; 25, 2: 112–118

Introduction

Differentiated cancer thyroid (DTC) has shown an increasing incidence over the last few decades [1]. It is distinguished by its multimodal therapeutic approach which is individualized and risk-adapted [2]. Surgery is considered a cornerstone of initial management followed by adjuvant radioactive iodine in indicated cases [3].

High-risk DTC is also known for its high rate of local recurrence and lymph node or soft tissue metastases; roughly calculated range is between 20% and 30%, other studies stated that the recurrence rate may reach up to 40% [4]. Distant metastases develop in up to 15% of cases, primarily as pulmonary metastases followed by bone metastases [5]. Prognosis mainly is depending on the site of recurrence. Whenever feasible, surgical re-intervention

Correspondence to: Mai Amr Elahmadawy, Nuclear Medicine Unit, National Cancer Institute (NCI), Cairo University, Foam Elkhalig, 11026 Cairo, Egypt, e-mail: Mai.elahmadawy@nci.cu.edu.eg

is the treatment of choice in cases of cervical nodal metastases and loco-regional recurrence before considering radioactive iodine or radiation therapy [5].

Differentiated cancer thyroid (DTC) risk stratification is a dynamic process that depends on using multiple staging systems and targets precise therapy tailoring with prediction of risk for recurrence and disease-relatedmortality [6]. Therefore, cervical nodal metastasis identification by preoperative imaging efficiently contributes to treatment planning [7].

[^{18}F]FDG PET/CT was shown to be an efficient imaging study in disease localization in patients with elevated thyroglobulin (Tg) levels, negative US, and I-WBS [5]. It was quickly surpassed by [^{18}F]FDG PET/CT, which combined the advantages of metabolic and morphologic imaging. [^{18}F]FDG PET/CT is accepted as the study of choice for post thyroidectomy patients with increased Tg blood levels and negative I-WBS [8]. However, recurrent, residual, or metastatic tissue does not always accumulate [^{18}F]FDG and consequently remains undetectable by [^{18}F]FDG PET/CT. As a consequence, supplementary imaging modalities performance may be needed to be also assessed in this aspect [5].

Magnetic resonance imaging (MRI) is the primary imaging modality for soft tissue neoplasms owing to its superior soft tissue contrast, additional functional imaging abilities, and reduced dental metal artifacts as compared to [^{18}F]FDG PET/CT [9].

Diffusion-weighted imaging (DWI) and apparent diffusion coefficient (ADC) measurements are being considered potentially useful in the assessment and characterization of head and neck different lesions. DWI can differentiate the viable and necrotic portions of head and neck tumors. The ADC can discriminate benign lesions from malignant tumors and tumor necrosis from abscesses [10].

Although DW-MR is not a routine investigation when evaluating thyroid cancer, it may become one of the choices owing to the efficiency of MRI for tumor diagnosis [11]. So, in the current study, we compared DW-MRI *vs.* [^{18}F]FDG PET/CT for the detection of cervical nodal metastases either in initially assessed patients with pathologically proven DTC or those with suspected loco-regional recurrence.

Material and methods

This prospective study included 30 adult patients represented between the period of December 2017 and January 2020. All patients were referred to perform MRI and DW-MRI as well as [^{18}F]FDG PET/CT respectively, either for initial nodal staging or detection of clinico-laboratory suspected nodal recurrence in pathologically proven differentiated thyroid cancer (DTC).

Clinical information was extracted from the medical records. The study has been approved by the ''Ethical Committee", with Institutional Review Board (IRB) number (201617077.3).

Inclusion criteria

- adults (>18 years),
- pathologically proven DTC Patients with initially high-risk clinico-pathological criteria,
- patients with clinical suspicion for local nodal deposits based on radiological (e.g.: sonography) and/or elevated tumour markers (rising Tg with negative I-131 WBS),
- patients eligible for surgical management.

Exclusion criteria

- pediatrics patients (<18 years old),
- double primary patients,
- contraindicated surgical management (i.e.: palliative inoperable or not fit for anesthesia or surgery),
- patients previously treated with local radiation therapy,
- general contraindications for performing PET/CT or MRI.

Patients' preparation and imaging techniques

[^{18}F]FDG PET/CT

- patients were instructed to fast for at least 4–6 h before the study,
- the fasting blood glucose level was determined with preferred fasting blood glucose below 150 mg/dL,
- [^{18}F]FDG PET/CT study was done using a dedicated Discovery PET/CT scanner (GE Medical System, USA),
- scanning started 45–60 min after tracer injection of about 0.15 mCi/kg,
- no CT contrast agents were administered,
- the images were interpreted by 1 experienced nuclear medicine physician blinded to the results of histopathology,
- images were interpreted through visual qualitative (visual) assessment where any regional lymph node regardless of the CT size exhibiting focal FDG uptake, superior to physiological background activity was interpreted as a positive node,
- quantitative assessment was performed by recording the maximum standardized uptake values (SUV_{max}) for the node with the highest activity.

DW-MRI

- the patients had their MRI done on a high field system (1.5 Tesla) closed magnet unit (Phillips Achieva XR),
- the MRI technique included multiplanar MR imaging sequences without contrast including T1, T2, and STIR WIs as well as DW sequence with multiple b-values (b-0, 400 and 800),
- the DW-MRI was visually interpreted (qualitative assessment) by three experienced radiologists. "Positive" was diagnosed when a definite abnormal localized area of diffusion restriction was noted as a high signal lesion confirmed by histopathological examination.
- regarding the quantitative analysis of DWIs, we measured the ADC at the most restricted area within the lesions.

Both DW-MRI and [^{18}F]FDG PET/CT findings were verified on the basis of

- histopathological data (obtained from surgical specimens),
- operative data and post-operative CT, MRI, and/or [^{18}F]FDG PET/CT imaging findings.

Statistical analysis

Continuous data are summarized in terms of mean and standard deviation. Categorical data is represented in terms of frequency and percentage (%). Sensitivity, specificity, positive predictive value (PPV), and negative predictive value (NPV) were calculated for each modality. We used the McNemar test to compare the discriminatory performance of two different modalities. ROC curve was used to assign the most appropriate cutoff value. We used R version 4.0.0 in this analysis.

Results

The 30 enrolled patients were 10 males and 20 females with age ranged 22–77 years, with pathologically proven DTC, referred either for initial nodal staging (in 4 patients) or detection of clinico-laboratory suspected nodal recurrence (in 26 patients) with rising Tg serum level and negative I-131 WBS. Serum TG levels for our group — under TSH suppression — was (median 25.20 ng/mL, range, 2–85 ng/mL). All patients performed both DWI-MRI and [^{18}F]FDG PET/CT techniques to assess the ability of each modality to detect cervical nodal metastasis. The main clinico-pathological characteristics of the study group are illustrated in (Supplementary Tab. 1).

Based on histopathology and post-operative clinico-radiological data and follow-up, out of the 30 investigated patients, 25 patients were positive for cervical nodal metastases (23 metastatic papillary carcinoma and 2 metastatic follicular carcinoma) while the remaining 5 patients revealed benign hyperplastic, inflammatory changes or primary disease without nodal metastasis. The time to recurrence ranged from 2 to 90 months.

Most of the cases were assessed radiologically by ultrasound neck examination (27 cases) and the remaining 3 cases were assessed by CT. Though the Ultrasound showed relatively reasonable sensitivity, PPV, and accuracy of 77%, 85% and 70.3% respectively, however, its specificity and NPV were as low as 40% and 28% respectively.

Comparison of diagnostic performance between different modalities

Based on the obtained pathological data, an attempt to compare the diagnostic performance of [^{18}F]FDG PET/CT and DW-MRI was performed.

Sensitivity, specificity, NPVand PPV were 84%, 80%, 50%, 95% for [^{18}F]FDG PET/CT compared to 84%, 60%, 42.8% and 91.3% for DW-MRI. Relatively higher specificity indices were noted with [^{18}F]FDG PET/CT compared to DW-MRI; however, it was not statistically significant ($p = 0.31$), but reflected in the diagnostic accuracy, which was 83% for [^{18}F]FDG PET/CT compared to 80% with diffusion MRI (Tab. 1).

Agreement of results was tested between [^{18}F]FDG PET/CT and DW-MRI. True positive agreement was found in 18 patients out of 25 (Supplementary Fig. 1). False-negative agreement was noted in 1 patient, while disagreement was found in 6 patients with equal share in false-negative results by both modalities (Fig. 1).

Among the 5 patients who were pathologically proven to be free from nodal metastases, when comparing [^{18}F]FDG PET/CT and DW-MRI were in agreement in 3 true negative patients. One false-positive agreement noted and one case of disagreement between both modalities was found which was truly negative with [^{18}F]FDG PET/CT and falsely positive with DW-MRI (Fig. 2).

Table 1. Diagnostic performance of [^{18}F]FDG PET/CT versus DW-MRI in nodal assessment (No. of patients = 30)

Modality	[^{18}F]FDG PET/CT	DW-MRI	p-value
True positive	21 (70%)	21 (70%)	
False positive	1 (3.3%)	2 (6.7%)	
True negative	4 (13.3%)	3 (10%)	
False negative	4 (13.3%)	4 (13.3%)	
Sensitivity	84%	84%	1
Specificity	80%	60%	0.31
Accuracy	83%	80%	
PPV	95%	91.3%	0.32
NPV	50%	42.8%	0.67

[^{18}F]FDG PET/CT — F-18 flurodeoxyglucose positron emission computed tomography; DW-MRI — diffusion-weighted magnetic resonance imaging; NPV — negative predictive value; PPV — positive predictive value

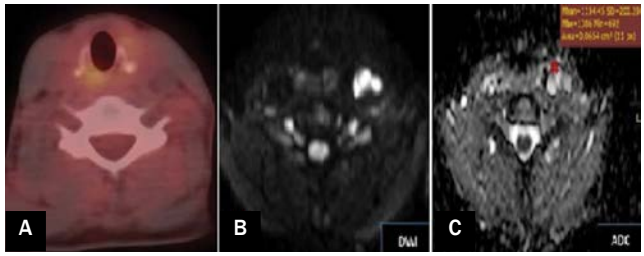

Figure 1. 31-year-old woman presented with PTC, underwent total thyroidectomy. Follow up assessment (3 months post-thyroidectomy): revealed rising TG level reached 7.1 ng/mL. PET/CT showed no FDG avid lesions (**A**). Conventional MRI showed left cervical level IV lymph node with suspicious features with bright signal on diffusion mostly T2 shine through effect (**B**), high ADC value = 1.1×10^{-3} mm^2/s (**C**). Pathological assessment revealed: metastatic papillary carcinoma

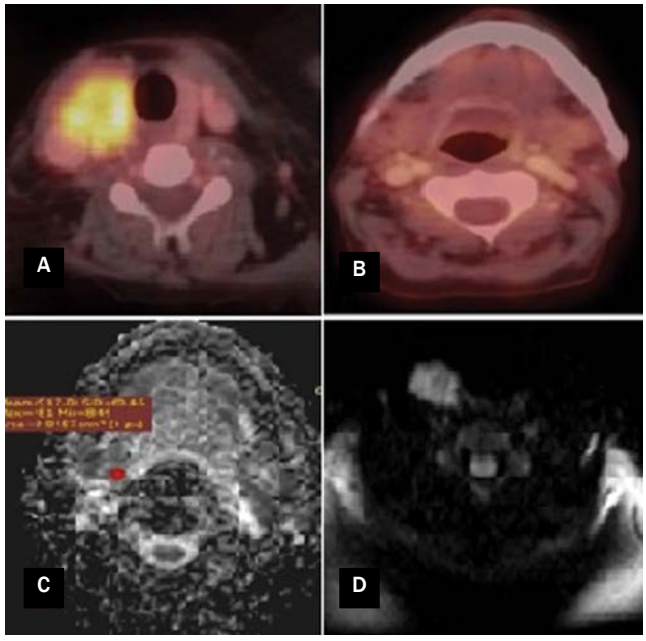

Figure 2. 50-year-old woman initially presented with de-novo neck swelling. PET/CT revealed: right thyroid lobe FDG avid focal lesion (**A**). Non-FDG avid right upper deep cervical nodes (level II; **B**). MRI showed right thyroid lobe focal nodular lesion, eliciting low T1 and intermediate T2 signal intensities. Clustering Right upper deep cervical lymph nodes (level II) with effaced fatty hilum, some of them are rounded & globular shape with irregular boarder, eliciting low T1 and intermediate T2 signal intensities. DWI and ADC map revealed Restricted diffusion for the thyroid nodular lesion as well as restricted diffusion and reduced ADC value (0.9×10^{-3} mm^2/s) for the nodal lesion (**C**). The patient underwent surgical interference with total thyroidectomy and right radical neck dissection. Pathology revealed papillary thyroid carcinoma and inflammatory changes of the upper deep cervical lymph nodes

The total fore mentioned disagreement of modalities in 6 patients out of 25 patients with positive nodal metastasis can be explained by the different diagnostic positive criteria on which different modalities rely. Such observation called for a further need to analyze the synergistic diagnostic potential that could be obtained through combining both modalities.

Diagnostic performance of Single versus combined modalities

On comparing the diagnostic performance of combined DWI-MRI and PET/CT compared to [^{18}F]FDG PET/CT alone, it was noted that only one true positive case was missed, which was consequently reflected in sensitivity indices that were notably higher with combined modalities, where the sensitivity of 96% and NPV of 80% was obtained compared to 84% and 50% with [^{18}F]FDG PET/CT alone. A trend for statistical significance was noted with p-value 0.08 and 0.07 for sensitivity and NPV respectively (Tab. 2).

Higher sensitivity indices were also noted when comparing DWI-MRI to combined DWI-MRI and [^{18}F]FDG PET/CT modalities, with the sensitivity of 84% and 96% and NPV 42.8% and 80% for DWI-MRI versus combined modalities respectively, which was statistically significant (p-value = 0.04) for NPV and shows a trend for statistical significance (p-value = 0.08) was noted for sensitivity (Tab. 3).

Table 2. Diagnostic performance of [^{18}F]FDG PET/CT versus combined DW-MRI and PET/CT in detection of nodal metastases (No. of patients = 30)

Modality	[^{18}F]FDG PET/CT	Combined DWI-MRI and PET/CT	p-value
True positive	21 (70%)	24 (80%)	
False positive	1 (3.3%)	1 (3.3%)	
True negative	4 (13.3%)	4 (16.6%)	
False negative	4 (13.3%)	1 (3.3%)	
Sensitivity	84%	96%	0.08
Specificity	80%	80%	1
Accuracy	83%	93%	
PPV	95%	96%	0.08
NPV	50%	80%	0.07

[^{18}F]FDG PET/CT — F-18 flurodeoxyglucose positron emission computed tomography; DW-MRI — diffusion-weighted magnetic resonance imaging; NPV — negative predictive value; PPV — positive predictive value

Table 3. Diagnostic performance of DW-MRI versus combined DW-MRI and PET/CT in detection of nodal metastases (No. of patients = 30)

Modality	DWI-MRI	Combined DWI-MRI and PET/CT	p-value
True positive	21 (70%)	24 (80%)	
False positive	2 (6.7%)	1 (3.3%)	
True negative	3 (10%)	4 (16.6%)	
False negative	4 (13.3%)	1 (3.3%)	
Sensitivity	84%	96%	0.08
Specificity	60%	80%	0.31
Accuracy	80%	93%	
PPV	91.3%	96%	0.23
NPV	42.8%	80%	0.04

[^{18}F]FDG PET/CT — F-18 flurodeoxyglucose positron emission computed tomography; DW-MRI — diffusion-weighted magnetic resonance imaging; NPV — negative predictive value; PPV — positive predictive value

Quantitative-based image analysis

DW-MRI ADC cut-off value

A cut-off value is defined as the criterion value range that predicts a positive condition. It was calculated by evaluating 71 nodes at different neck levels. The minimum and maximum ADC values were found to be 0.53 and 2 respectively, eliciting 1.04 as a mean ADC value, with a 0.26 standard deviation.

Receiver operating characteristic (ROC) analysis showed that the area under the curve was 0.69 and the optimum threshold for the ADC was 1.01 $\times$ 10^{-3}mm^2/s with sensitivity, specificity, accuracy, and PPV of 61%, 80%, 68%, and 85% respectively being plotted on ROC curve with p = 0.001, denoting the significance of the applied data (Fig. 3).

[18F]FDG PET/CT cut-off value

A cut-off value indicates the identification of the value range that predicts a positive condition. It was calculated by evaluating 54 nodes at different neck levels. The minimal and maximal SUV were found to be 1.6 and 46.3 respectively, with a mean value of 8.6 and a standard deviation of 9.9.

ROC analysis showed that the area under the curve was 0.88 and the optimum threshold for the SUV was 3.1 with sensitivity, specificity, accuracy, and PPV of 81%, 83%, 81% and 98% respectively, being plotted on ROC curve (Fig. 4), with p = 0.002, denoting the significance of the applied data.

Discussion

So far only a few published studies conducted Head-to-Head Comparison of [^{18}F]FDG PET/CT and DW-MRI in the detection of initial or recurrent regional nodal metastases from DTC [11].

In the current study, 21 patients out of 30 patients were detected by DW-MRI as true positive patients eliciting 70% as detectability, while Nagamachi S et al. [11], whose study was conducted on 59 patients with DTC, from which, 34 patients with positive nodal deposits were detected by DW-MRI and thus eliciting (57.6%) as detectability.

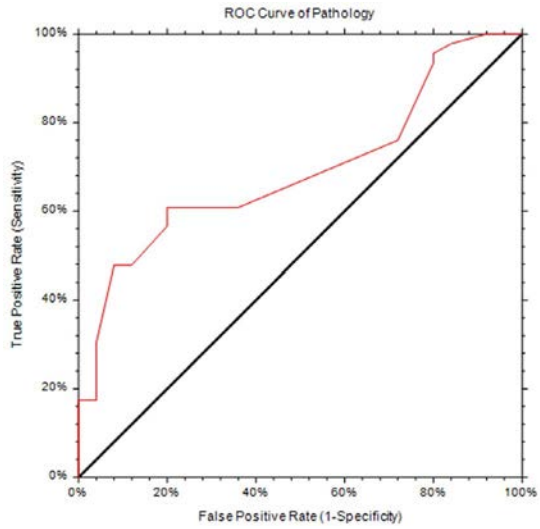

Figure 3. ROC curve for ADC cutoff; AUC = 69% and p-value = 0.001

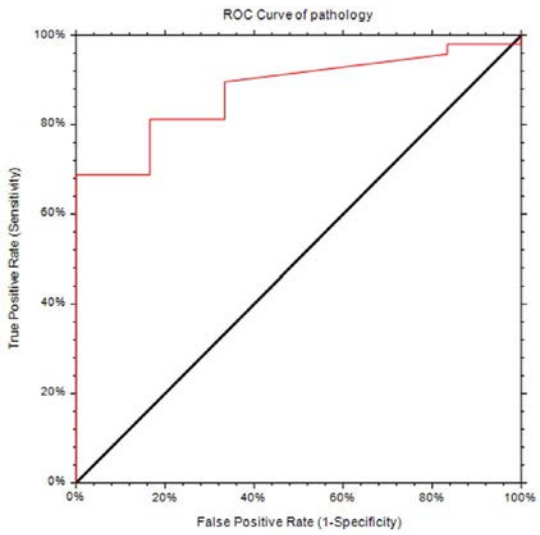

Figure 4. ROC curve for SUV cutoff, AUC = 80% and p-value = 0.002

Regarding [^{18}F]FDG PET/CT; our study showed prominent sensitivity of 84% and specificity of 80% for regional nodal metastases during initial assessment or detection of recurrence. Meanwhile, a study performed by Weber T et al. [12], evaluating the role of [^{18}F]FDG PET/CT for pre-surgical assessment of patients with persistent or recurrent DTC, showed a relatively higher sensitivity (93%) and lower specificity (75%) than our study. However, it is worth mentioning that their study group included only 18 patients who were candidate for cervical re-exploration.

Also, Hempel J et al. [5], who studied 46 DTC patients, concluded a relatively higher sensitivity than our study (88%) and a non-concordant lower specificity (67%). Considering the retrospective nature of their study, beside their dependency on the retrieved original scan reports for clinical decisions, there is a strong limiting element for neutral patients' evaluation and standardized criteria-based diagnosis.

In agreement with our study, close results were obtained from a previous meta-analysis carried out by Kim S et al. [13]; that was performed across 9 studies with 515 patients, aiming at assessing the diagnostic performance of [^{18}F]FDG PET/CT for detection of recurrent and/or metastatic DTC patients. This metanalysis revealed pooled sensitivity and specificity of 84% and 78% respectively.

In the same pace, another meta-analysis done by Caetano R et al. [14] evaluated the accuracy of [^{18}F]FDG PET/CT and [^{18}F]FDG PET/CT for detecting recurrence of DTC where pooled sensitivity showed relatively higher results eliciting 93%, and nearly similar pooled specificity 81%.

Comparing DW-MRI to [^{18}F]FDG PET/CT, our study revealed higher specificity for [^{18}F]FDG PET/CT surpassing DW-MRI with the specificity of 80% and 60% respectively. This was not the same as regards sensitivity which was congruent for both modalities (84%). Meanwhile, Nagamachi S et al. [11] revealed superiority for the capability of [^{18}F]FDG PET/CT for detection of nodal metastasis or recurrence compared to DW-MRI with the sensitivity of 84.2% and 57.6% respectively.

Recently, combined PET and MRI have come into existence as a major hybrid imaging modality. Such modality provided both the quantifiable functional and molecular information through PET combined to the unique tissue characterization of MRI [15].

By attempting to investigate such synergistic diagnostic performance that could be obtained from combined DW-MRI and [^{18}F]FDG PET/CT, our study revealed increased sensitivity that reached 96% compared to 84% when using either DW-MRI or PET/CT alone. However, the specificity (80%) was equivalent to that obtained using [^{18}F]FDG PET/CT alone.

Reliability on different diagnostic imaging-based criteria for PET and DW-MRI may point to the need for assessing their complementary diagnostic role. It may stand behind the higher detection rate that could be achieved using combined modalities, with subsequently higher sensitivity than that obtained in our study. Such opinion was also supported by the notable incidence of disagreement between [^{18}F]FDG PET/CT and DW-MRI which represented 24% of the pathologically proven group with nodal metastases (6 out of 25 patients).

Close sensitivity of 94% was obtained by Hempel J et al. [5], who investigated the diagnostic performance of the combined conventional MRI and PET/CT modalities, however, it is worth mentioning that their study lacks evaluation of MRI diffusion sequences.

Quantitative-based Image Analysis

Regarding DW-MRI ADC cut-off value, in the present study the optimum threshold for the ADC was 1.01×10^{-3} mm^2/s with sensitivity, specificity, accuracy, and PPV of 61%, 80%, 68%, and 85% respectively with p-value = 0.001, denoting significance of the applied data.

Kanmaz L et al. [16] had studied the role of DW-MRI in the differentiation of head and neck masses and found that when the ADC value of 1.13×10^{-3} mm^2/s or less was used to predict malignancy, the best results were achieved with sensitivity, specificity, accuracy and PPV of 93.33%, 82.35%, 87.5%, and 82.35% respectively.

Another study was carried out to assess the role of the ADC in the differentiation between benign and malignant neck masses held by Salem F et al. [10]. They found that the optimum threshold for the ADC was 1.25×10^{-3} mm^2/s, resulting in a sensitivity, specificity, and accuracy of 95.4%, 83.3% and 92% respectively.

According to Razek A. et al [17], which have also studied the role of DW-MRI in cervical lymphadenopathy, if an ADC value of 1.38×10^{-3} mm^2/s was used as a threshold value for differentiating malignant from benign lymph nodes, the best results were obtained with an accuracy, sensitivity, specificity, PPV and NPV as 96%, 98%, 88%, 98.5%, and 83.7% respectively.

Many reasons can be related to the large variations between studies on ADC values. For example, the choice of the b values, as a lower b values, increases the signal-to-noise ratio for being in stage but makes the sensitivity to diffusion worse. Also, the choice of the region of interest on ADC maps and the use of sequences that minimize artifacts to make the calculation of the area of interest more accurate are other considerations [18].

Very limited studies have used SUV_{max} cutoff value either for assessment of nodal metastases in DTC. In our study ROC marked SUV_{max} 3.1 as a discriminating diagnostic value with sensitivity,

specificity, accuracy, and PPV as 81%, 83%, 81%, and 98% respectively, with significance was noted (p-value = 0.002).

Chong et al. [19] compare the diagnostic performance of [^{18}F]FDG PET/CT versus CT in pre-operative detection of regional nodal metastases from papillary thyroid carcinoma, concluded that better sensitivity for [^{18}F]FDG PET/CT could be achieved when using SUV_{max} 2 as a diagnostic cutoff value exceeding the sensitivity of conventional CT. In agreement with the previous study, Jeong et al. [20] also used SUV_{max} 2.0 as the cutoff value for nodal metastases.

Other authors tried to predict the regional nodal metastatic potentiality in papillary thyroid carcinoma by deducing a cutoff point from the primary tumor itself, where Jung et al [21] marked SUV_{max} 4.6 to be an optimum cutoff point associated with cervical nodal deposits. Lower cutoff point of 2.6 was reported by Byun et al [22]. Variation in deduced cutoffs is likely technically related due to different machines that may influence SUV_{max} values.

Study limitations

The study enrolled a relatively small population of DTC patients. However, the prospective nature of the study together with the mandated pathological verification of the whole group stood behind it. MRI studies lack using of contrast media which may influence its sensitivity. The current study also lacks a direct correlation between TG level and scans findings.

Conclusions

[^{18}F]FDG PET/CT study is a valuable diagnostic modality for the assessment of DTC patients, who are at risk or with suspected recurrent regional nodal metastases with reasonable specificity surpassing DW-MRI. Combined [^{18}F]FDG PET/CT and DW-MRI have synergistic diagnostic performance for nodal metastases detection in DTC, associated with better sensitivity than using a single modality.

Recommendations

Further studies with a larger population may allow detailed per level/compartmental nodal-based analysis. Beside its established role in other head and neck malignancies, PET/MRI should be furtherly investigated in DTC patients considering the combined value that could be obtained from both functional and tissue characterizing techniques. Semi-quantitative and quantitative methods of image analysis are essential and should be standardized to lower inter-observer variability with higher reproducibility while providing a range of values for comparison with other indicators of disease extent and response.

Conflict of interest

Authors have no conflicts of interest and have nothing to disclose.

References

1. Furuya-Kanamori L, Sedrakyan A, Onitilo AA, et al. Differentiated thyroid cancer: millions spent with no tangible gain? Endocr Relat Cancer. 2018; 25(1): 51–57, doi: 10.1530/ERC-17-0397, indexed in Pubmed: 29042396.
2. Schmidbauer B, Menhart K, Hellwig D, et al. Differentiated thyroid cancer-treatment: state of the art. Int J Mol Sci. 2017; 18(6), doi: 10.3390/ijms18061292, indexed in Pubmed: 28629126.
3. Shokoohi A, Berthelet E, Gill S, et al. Treatment for recurrent differentiated thyroid cancer: a canadian population based experience. Cureus. 2020; 12(2): e7122, doi: 10.7759/cureus.7122, indexed in Pubmed: 32257668.
4. Hollenbeak CS, Boltz MM, Schaefer EW, et al. Recurrence of differentiated thyroid cancer in the elderly. Eur J Endocrinol. 2013; 168(4): 549–556, doi: 10.1530/EJE-12-0848, indexed in Pubmed: 23337385.
5. Hempel JM, Kloeckner R, Krick S. Impact of combined FDG-PET/CT and MRI on the detection of local recurrence and nodal metastases in thyroid cancer. Cancer Imaging. 2016; 16(1): 37, doi: 10.1186/s40644-016-0096-y, indexed in Pubmed: 27809936.
6. Papaleontiou M, Haymart MR. New insights in risk stratification of differentiated thyroid cancer. Curr Opin Oncol. 2014; 26(1): 1–7, doi: 10.1097/cco.0000000000000022, indexed in Pubmed: 24285100.
7. Chen Q, Raghavan P, Mukherjee S, et al. Accuracy of MRI for the diagnosis of metastatic cervical lymphadenopathy in patients with thyroid cancer. Radiol Med. 2015; 120(10): 959–966, doi: 10.1007/s11547-014-0474-0, indexed in Pubmed: 25725789.
8. Treglia G, Muoio B, Giovanella L, et al. The role of positron emission tomography and positron emission tomography/computed tomography in thyroid tumours: an overview. Eur Arch Otorhinolaryngol. 2013; 270(6): 1783–1787, doi: 10.1007/s00405-012-2205-2, indexed in Pubmed: 23053387.
9. Platzek I, Beuthien-Baumann B, Schneider M, et al. PET/MRI in head and neck cancer: initial experience. Eur J Nucl Med Mol Imaging. 2013; 40(1): 6–11, doi: 10.1007/s00259-012-2248-z, indexed in Pubmed: 23053322.
10. Salem F, Elshafey R, Elmahalawy M, et al. Apparent diffusion coefficient measurements in the differentiation between benign and malignant neck masses. Egyptian J Radiol Nucl Med. 2014; 45(2): 367–375, doi: 10.1016/j.ejrnm.2014.01.011.
11. Nagamachi S, Wakamatsu H, Kiyohara S, et al. Comparison of diagnostic and prognostic capabilities of ^{18}F-FDG-PET/CT, ^{131}I-scintigraphy, and diffusion-weighted magnetic resonance imaging for postoperative thyroid cancer. Jpn J Radiol. 2011; 29(6): 413–422, doi: 10.1007/s11604-011-0572-z, indexed in Pubmed: 21786097.
12. Weber T, Ohlhauser D, Hillenbrand A, et al. Impact of FDG-PET computed tomography for surgery of recurrent or persistent differentiated thyroid carcinoma. Horm Metab Res. 2012; 44(12): 904–908, doi: 10.1055/s-0032-1316351, indexed in Pubmed: 22791600.
13. Kim SJ, Lee SW, Pak K, et al. Diagnostic performance of PET in thyroid cancer with elevated anti-Tg Ab. Endocr Relat Cancer. 2018; 25(6): 643–652, doi: 10.1530/ERC-17-0341, indexed in Pubmed: 29559552.
14. Caetano R, Bastos C, Oliveira Ide, et al. Accuracy of positron emission tomography and positron emission tomography-CT in the detection of differentiated thyroid cancer recurrence with negative^{131}I whole-body scan results: A meta-analysis. Head & Neck. 2015; 38(2): 316–327, doi: 10.1002/hed.23881.
15. Rosenkrantz AB, Friedman K, Chandarana H, et al. Current Status of Hybrid PET/MRI in Oncologic Imaging. AJR Am J Roentgenol. 2016; 206(1): 162–172, doi: 10.2214/ajr.15.14968.
16. Kanmaz L, Karavas E. The role of diffusion-weighted magnetic resonance imaging in the differentiation of head and neck masses. J Clin Med. 2018; 7(6): 130, doi: 10.3390/jcm7060130, indexed in Pubmed: 29844262.
17. Razek AK, Soliman NY, Elkhamary S, et al. Role of diffusion-weighted MR imaging in cervical lymphadenopathy. Eur Radiol. 2006; 16(7): 1468–1477, doi: 10.1007/s00330-005-0133-x, indexed in Pubmed: 16557366.
18. Perrone A, Guerrisi P, Izzo L, et al. Diffusion-weighted MRI in cervical lymph nodes: differentiation between benign and malignant lesions. Eur J Radiol. 2011; 77(2): 281–286, doi: 10.1016/j.ejrad.2009.07.039, indexed in Pubmed: 19716671.
19. Chong A, Ha JM, Han YH, et al. Preoperative lymph node staging by FDG PET/CT with contrast enhancement for thyroid cancer: a multicenter

study and comparison with neck CT. Clin Exp Otorhinolaryngol. 2017; 10(1): 121–128, doi: 10.21053/ceo.2015.01424, indexed in Pubmed: 27334517.

20. Jeong HS, Baek CH, Son YI, et al. Integrated 18F-FDG PET/CT for the initial evaluation of cervical node level of patients with papillary thyroid carcinoma: comparison with ultrasound and contrast-enhanced CT. Clin Endocrinol (Oxf). 2006; 65(3): 402–407, doi: 10.1111/j.1365-2265.2006.02612.x, indexed in Pubmed: 16918964.
21. Jung Jh, Kim CY, Son SH, et al. Preoperative prediction of cervical lymph node metastasis using primary tumor suvmax on 18F-FDG PET/CT in patients with papillary thyroid carcinoma. PLoS One. 2015; 10(12): e0144152, doi: 10.1371/journal.pone.0144152, indexed in Pubmed: 26636824.
22. Byun BH, Jeong UG, Hong SP, et al. Prediction of central lymph node metastasis from papillary thyroid microcarcinoma by 18F-fluorodeoxyglucose PET/CT and ultrasonography. Ann Nucl Med. 2012; 26(6): 471–477, doi: 10.1007/s12149-012-0594-3, indexed in Pubmed: 22467230.

VIA MEDICA

Nuclear Medicine Review 2022, 25, 2: 119–126
DOI: 10.5603/NMR.a2022.0025

ISSN 1506–9680, e-ISSN 1644–4345

Review

Myocardial perfusion imaging using single-photon emission computed tomography with cadmium-zinc-telluride technology

Sonia J. Konsek-Komorowska[1], Mariola Peczkowska[2], Jaroslaw B. Cwikla[1, 3]

[1]Department of Cardiology and Internal Medicine, School of Medicine, Collegium Medicum, University of Warmia and Mazury in Olsztyn, Olsztyn, Poland
[2]Department of Hypertension, The Cardinal Stefan Wyszynski National Institute of Cardiology, Warsaw, Poland
[3]Diagnostic and Therapeutic Center — Gammed, Warsaw, Poland

[Received 21 I 2022; Accepted 9 VI 2022]

Abstract

Myocardial perfusion imaging (MPI) with single-photon emission computed tomography (SPECT) is a well-established diagnostic approach for patients with suspected or confirmed coronary artery disease (CAD). In the present century, nuclear cardiology has benefited immensely from advances in imaging instrumentation and technology. Dedicated cardiac SPECT cameras incorporating novel, highly efficient cadmium-zinc-telluride (CZT) detectors, collimators, and system designs have evolved as a result of the expansion of nuclear cardiology. A vast amount of evidence is emerging, demonstrating the new technology's advantages over the traditional gamma cameras. Myocardial perfusion imaging (MPI) using gamma-cameras with CZT detectors may be performed with the limited injected activity of radiotracer and recorded times. The use of CZT's dynamic acquisition of myocardial perfusion imaging in clinical practice may help cardiologists in detecting hemodynamically significant CAD. In this article, we present the current state of knowledge on cardiac CZT-SPECT scanners, a summary of the literature published on validation studies, radiation dose reduction, and dynamic acquisition, as well as a comparison of conventional myocardial perfusion imaging with invasive coronary angiography.

KEY words: myocardial perfusion imaging; CZT; coronary artery disease; CAD; cadmium-zinc-telluride single-photon emission computed tomography; CZT-SPECT; CZT; nuclear cardiology

Nucl Med Rev 2022; 25, 2: 119–126

Introduction

Myocardial perfusion imaging (MPI) is a useful approach for identifying coronary artery disease (CAD) which is a pathological condition defined by atherosclerotic plaque formation in the epicardial arteries, and can be obstructive or non-obstructive [1]. Functional non-invasive test such as single-photon emission computed tomography (SPECT) for the diagnosis of obstructive CAD is designed to detect perfusion changes. Exercise or pharmacological stressors can cause ischemia by increasing cardiac work and oxygen requirement or by heterogeneity in myocardial perfusion caused by the widening of blood vessels [2]. Invasive coronary angiography (CAG) has been the gold standard in the diagnosis of CAD for many years. However, one of the major drawbacks of this approach is that it only gives anatomical evaluation. MPI is superior to anatomical evaluation alone in terms of providing information regarding myocardial viability and function [3, 4]. When compared to invasive functional testing fractional flow reserve (FFR), non-invasive functional tests are linked with high accuracy in the diagnosis of flow-limiting coronary stenosis. According to the European Society of Cardiology Guidelines for the diagnosis and

Correspondence to: Sonia J. Konsek-Komorowska
Department of Cardiology and Internal Medicine, School of Medicine, Collegium Medicum, University of Warmia and Mazury in Olsztyn, Warszawska 30, 10-082 Olsztyn, Poland
phone: +48 89 524 53 89
e-mail: sonia.konsek@interia.pl

management of chronic coronary syndromes from 2019, non-invasive functional imaging for myocardial ischemia such as SPECT or coronary computed tomography angiography (CTA) is indicated as the initial test for identifying CAD in symptomatic individuals in whom clinical examination alone cannot rule out obstructive CAD. Myocardial perfusion imaging (MPI) with SPECT may be used in conjunction with dynamic exercise testing and can be chosen if extra information from the exercise test, for example, heart rate response to activity or exercise tolerance, is deemed significant [2]. MPI use has increased significantly over the last decade, and it is currently the most widely utilized non-invasive imaging method for risk stratification in patients with suspected or known CAD [5].

Nowadays, there is a trend for identifying strategies and protocols to minimize radiation exposure for patients as well as for standard laboratory operating procedures. Weighing the dosimetry of currently used cardiac imaging procedures would be a first step toward implementing a test choice technique to reduce overall risk to individuals while retaining excellent diagnostic data [6]. From a clinical standpoint, a few important matters should be well-thought-out when approaching diagnostic imaging: the first is the need to take close notice of the issue of radiation exposure and associated hazards, and the second is the recognition that imaging techniques must demonstrate a solid ability to affect patient supervision by enhancing clinical outcomes. This attention points to the selection of a lower-radiation-dose imaging modality among those available, based on the clinical benefit for a specific patient.

Several attempts to enhance the MPI approach through the use of iterative reconstruction algorithms [7, 8], early-imaging protocols [9], or new tracers [10] yielded excellent discoveries but no breakthroughs that turned into applications that improved everyday clinical practice [4]. New low-dose procedures and new technology have been developed to address these issues, expanding the use of MPI in clinical practice [1]. Detectors based on cadmium zinc telluride (CZT) have been used in SPECT imaging systems since the first decade of the 21st century [11, 12]. When compared to typical gamma cameras, myocardial perfusion scintigraphy may be conducted more quickly and with less radiation exposure [3, 11]. These devices have more sensitive solid-state CZT detectors and have greater spatial and energy resolution than the conventional type of camera which employs the use of a scintillation detector, applying natrium iodide crystal activated by thallium (NaI [Tl]) [11, 12].

In this review article, we aim to present a detailed description of the diagnostic value of CZT-SPECT and a number of technical points associated with image acquisition, data post-processing, and as well as interpretation. A brief summary of prior accomplished investigations with CZT-SPECT cameras is also given.

Cadmium-zinc-telluride SPECT scanners

The CZT detector functions as a semiconductor, converting gamma radiation directly to an electric signal. This mechanism improves spatial resolution and sensitivity, resulting in a lower given dose of radiopharmaceuticals and/or a quicker acquisition time [12]. There are now two commercially available CZT-SPECT scanners: D-SPECT (Spectrum Dynamics, Caesarea, Israel) and Discovery 530 or Discovery 570c (GE Healthcare, Waukesha, Wi, USA) [11]. Both systems employ solid-state CZT detector assemblies, which are made up of smaller units that individually produce projection data in a 16 $\times$16 matrix with 2.46 $\times$ 2.46 mm pixels. The cadmium zinc telluride thickness is 5 mm, and both scanners utilize identical CZT modules. Each pair producing current is separated by the voltage across the crystal. There is no scintillation and no photomultipliers, unlike traditional Anger cameras [13]. D-SPECT, which employs pixelated cadmium zinc telluride detector arrays in nine vertical columns arranged in a 90° gantry geometry, is one of the most often used systems. Tungsten is used to make the parallel hole high sensitivity collimators. Discovery 530 or Discovery 570c model is built on a multi-pinhole collimator system and a pixelated array of 19 cadmium zinc telluride detectors [12]. Image quality has improved in both systems due to increased sensitivity in detecting cardiac activity [1]. The spatial resolution of the GE Discovery was stated to be superior (6.7 mm) compared to D-SPECT (8.6 mm). On the contrary, the count sensitivity of the D-SPECT was reported to be higher (850 counts per second per MBq) compared to GE Discovery (460 counts per second per MBq). Those two parameters outperform the standard SPECT mean values (15.3 mm of spatial resolution and sensitivity of 130 counts per second per MBq) [12, 14]. These results show a significant improvement in image quality, owing to a decreased amount of Compton photons inside the acquisition energy window [1]. D-SPECT and GE Discovery use iterative reconstruction, but with different filters as well as reconstruction parameters, such as the number of iterations and subsets employed [11]. The creation of a specific three-dimensional iterative reconstruction technique based on maximum likelihood expectation maximization, which adjusted for the loss in spatial resolution caused by the collimator's line response function, enhanced CZT picture quality even more [15].

Clinical validation tests revealed that the innovative CZT camera allowed for a more than five-fold decrease in scan duration while providing clinical information comparable to typical SPECT MPI [16, 17]. In the first study comparing ultrafast versus traditional cameras for detecting obstructive coronary artery disease, using CAG as the gold standard, the CZT scanner detected a greater number of vessels with obstructive CAD, regardless of comparable diagnostic confidence on a per-patient basis [18]. According to these findings, an ultrafast device provides a more precise assessment of the extent and severity of myocardial ischemia in individuals with coronary artery disease [19]. Accordingly, the greatest improvement has been recorded in the left circumflex (LCX) and right coronary artery (RCA) territories, resulting in a clearer demarcation of multi-vessel CAD and highlighting the tremendous relevance for therapeutic application in subjects with severe coronary artery disease, as verified by many investigations [16–18].

Radiation dose reduction

The possibility of carcinogenesis from radiation connected with medical imaging examinations is still being debated in the literature. The radiation linked with SPECT MPI comes from a gamma-emitting isotope administered intravenously usually in two doses. The majority of patients showed no genotoxic effects following SPECT MPI, but a minority (about one-third) exhibited both protein phosphorylation and elevated expression of DNA damage genes, indicating a heightened vulnerability to radiation effects [20]. In addition, it became clear that it is extremely challenging to objectively show any impairment that low doses of radiation can possibly cause on patients [1].

Radiation dosage reduction is currently amongst the most common pitfalls in diagnostic procedures. Although nuclear medicine procedures are not the primary source of radiation exposure in medical management when compared to computed tomography, reducing provided dosages of radiopharmaceuticals is beneficial for both patients and nuclear cardiology personnel [12].

Preliminary reports [21] and early clinical studies [22, 23] demonstrated the possibility of reducing acquisition time for stress and rest myocardial perfusion imagining. Based on these initial findings, the device with efficient cadmium-zinc-telluride detectors rendered a significant milestone for the everyday use of myocardial perfusion imagining in clinical practice [1].

Duvall et al. [24] reported the clinical experience with a CZT scanner and dosage reduction. The authors retrospectively analyzed images of 717 patients, which were obtained using ^{99m}Tc- sestamibi stress gated SPECT MPI studies done on a CZT camera (Discovery NM 530c). The MPI procedures were carried out within a four-month period, and subjects were categorized into three groups depending on the protocol: low-dose stress-only, high-dose stress-only, and low-dose rest high-dose stress. The ^{99m}Tc stress dosage for the low-dose protocol was 462.5 MBq, whereas the high dose ranged from 925–1332 MBq depending on the patient's weight. The low-dose rest dose was 296–481 MBq which was likewise weight-adjusted. In comparison to the standard rest-stress doses, radiation activity was reduced by 70% in the low-dose stress-only group and 30% in the high-dose stress-only group. In comparison to standard rest-stress doses, the effective dose in the low-dose stress-only group was reduced by 64% on average and by 32% in the high-dose stress-only group. A comparable number of total counts were obtained after MPI for 5 minutes in low-dose stress-only subjects and 3 minutes in high-dose stress-only and rest-stress patients. The low-dose stress-only group had a 57% isotope dose reduction in comparison to the high-dose stress-only subjects, resulting in identical picture quality in all three groups [24].

In further research, compared to a scintillation camera, image quality or diagnostic accuracy were not affected by lowering acquisition time with a low administered dose. On the CZT camera, acquisition times were five and eight minutes for rest, three and five minutes for stress images, and fifteen minutes for stress on traditional SPECT. There was no significant difference between CZT and conventional cameras concerning ejection fraction (EF), mean perfusion deficit, or left ventricular (LV) volumes assessed by the acquisition time (short versus long). Despite the shorter time and lower total impulse count, the pictures acquired by CZT SPECT were of substantially higher quality [25].

According to a report by Einstein et al. [26] the picture quality, EF, and total perfusion deficit (TPD) acquired by the CZT device were all in satisfactory correlation using an ultra-low-dose protocol (with radiation exposure of about 1 mSv).

Diagnostic value of CZT-SPECT in coronary artery disease

The integrated technique, which combines cardiac imaging with gated SPECT to measure perfusion and function, has been proved to be beneficial in tissue characterization and prognosis, giving essential data for clinical management in subjects with suspected or confirmed coronary artery disease [1]. The results of perfusion images acquired with the CZT-SPECT and Anger SPECT cameras were found to be very consistent. Esteves et al. [22] compared images acquired with the Discovery NM 530c and conventional gamma cameras in multicenter research involving 168 patients. The images had a 91.9% concordance in detecting or excluding ischemia in comparison to a 92.5% agreement when the same examinations performed with a conventional camera were reviewed twice, $p = 0.99$. Sharir et al. [27] revealed, in a multicenter analysis including 238 subjects, high agreement of quantitative evaluation of TPDs (linear correlation coefficients for D-SPECT and Anger SPECT in the stress and rest examinations equaled 0.95 and 0.97, respectively) with a strong concordance in areas supplied by three main vessels (kappa coefficients for the left anterior descending coronary artery (LAD) and left circumflex coronary artery (LCX) were 0.73, and for right coronary artery (RCA) was 0.70, the agreement in identifying ischemia in each of the three territories supplied by LAD, LCX and RCA exceeded 90%).

Cantoni et al. [28] revealed, in relation to CAG, that MPI using SPECT with CZT detectors is a beneficial tool that can be used appropriately in the identification of CAD in a meta-analysis of 40 studies involving a total of 7734 patient studies on the diagnostic efficacy of SPECT using CZT detectors and Anger SPECT. Its diagnostic efficacy was marginally higher than that of a conventional SPECT camera in comparison to CAG [sensitivity 89% versus 85%, specificity 69% versus 66%, areas under the ROC curve (AUC) 0.89 versus 0.83]. The accuracy of SPECT using CZT detectors studies was minimally, but statistically significant, greater than that of Anger SPECT examinations ($p = 0.05$). This may be explained by the increased contrast of images generated with semiconductor gamma cameras due to improved spatial resolution. Earlier meta-analyses concerning studies on semiconductor cameras combined with CAG conducted by Nudi et al. [29] on 2092 subjects and Zhang et al. [30] on 2350 subjects found comparable outcomes in terms of study sensitivity and specificity in the detection of CAD, with no significant alterations between the two CZT devices utilized in the study.

Gimelli et al. [31] demonstrated, using data from 695 individuals, that a CZT camera may identify coronary artery disease in subjects with multivessel disease. The AUCs determined using semi-quantitative measures — summed stress scores (SSS) — in patients with two- and three-vessel disease, 0.83 and 0.79, respectively, did not differ substantially from the area under the ROC curve in single-vessel patients — 0.80. In 64% of patients, this approach correctly detected the severity of CAD. Regional perfusion abnormalities associated with the location of the three main coronary arteries were recognized with high efficiency (AUC for LAD was 0.90, for LCX was 0.88, and for RCA was 0.87). The research by Gimelli et al. [31] reveals that semiconductor cameras outperform conventional cameras in terms of detecting patients with multivessel disease.

Attempts are undertaken to correct image attenuation to increase the quality of studies. According to Esteves et al. [32], attenuation correction of CZT SPECT images has no significant effect on their visual interpretation. Another method for improving study quality is to rotate the patient during data acquisition, expecting that the filling of perfusion deficits caused by a modification in subject position shows their incorrect origin. Only the Discovery

NM 530c camera allows for study acquisition in the prone and supine positions. In a meta-analysis of investigations employing conventional and semiconductor cameras, Mirshavalad et al. [33] revealed that the prone position study which included 1490 patients compared to the supine position study which included 1138 patients has similar sensitivity (83% versus 8%) and better specificity (79% versus 67%). The prone position has a pooled sensitivity and specificity of 70% and 84% in identifying right coronary artery territory defects, respectively. Nishiyama et al. [34] analyzed 276 subjects and indicated that using data from supine and prone position significantly enhances perfusion interpretation concerning specificity ($p = 0.02$) and accuracy ($p = 0.04$) when compared to the supine position: sensitivity, specificity, and accuracy were as follow: 85% versus 78%, 85% versus 50%, and 85% versus 76%, respectively. In the case of D-SPECT, studies may be obtained in the upright, supine, and biker-like positions. A study by Nakazato et al. [35] combined evaluation of images obtained in the upright and supine position, compared to the outcomes of invasive CAG, yielded a sensitivity of 94% and specificity of 86%, in comparison to examinations obtained only in the upright (91% and 59%) or only supine (88% and 73%) positions; AUCs varied statistically significantly (0.94 versus 0.88 and 0.89, $p < 0.05$). In comparison to the upright and supine positions, the forward-leaning biker-like position reduced the distance between the heart and the detector and removed attenuation artifacts [36].

Diagnostic value of CZT-SPECT in the assessment of left ventricular contractility

Various published data highlight the significance of CZT cameras for LV function evaluation, offering crucial data on the feasibility of using the new cameras for a combined assessment. Gated acquisition of an MPI with SPECT and a patient electrocardiogram signal (G-SPECT) improves the study's diagnostic usefulness by assessing regional and global LV contractility [37]. CZT-G-SPECT has been compared to gold standard magnetic resonance imaging (MRI) and Anger G-SPECT concerning LV functional parameters (end-systolic volume — ESV, end-diastolic volume — EDV, and EF) [38–40]. In studies on this topic, Cochet et al. [38], Giorgetti et al. [39], and Claudin et al. [40] found a high or moderately high correlation between the findings of EDV assessment (0.71; 0.90; 0.94, respectively) and ESV (0.88; 0.94; 0.96, respectively) in comparison to MRI [38–40]. Giorgetti et al. [39] found that reported volumes were greatly underestimated due to the lower resolution of CZT-SPECT cameras compared to MRI. Nonetheless, these changes had no significant impact on global EF evaluation. In general, strong correlations were found between the EF values acquired from G-SPECT using CZT detectors and MRI (0.81, 0.84, and 0.88, respectively) [38–40]. It is important to emphasize that because CZT cameras have a superior resolution, the values of LV volume estimates are less underestimated than with standard devices.

Sala et al. [41] compared LV volume and EF measurements using the Discovery device and MRI. Although the volume and EF were greatly correlated with magnetic resonance outcomes (EDV, ESV, and EF 0.91, 0.95, and 0.86, respectively), the ejection fraction was consistently significantly undervalued [48 (15%) versus 55 (18%); $p = 0.001$], while the ESV was consistently exaggerated [84 (71) versus 72 (63) mL; $p = 0.001$]. Alterations between findings and what has been reported in those previous investigations are problematic to interpret.

The first clinical validation of MPI utilizing a CZT camera to assess regional and global left ventricular function shows outstanding concordance between cadmium-zinc-telluride technology and cardiac magnetic resonance (CMR). The low systematic bias (−2.7 percent) has been shown to have negligible clinical importance, and full wall thickening and wall motion estimates utilizing CZT devices may similarly be used to identify myocardial scarring, as determined by delayed enhancement in CMR. Myocardial perfusion imagining using CZT-SPECT scanners and quantitative gated SPECT analysis precisely quantifying the EF. However, in accordance with prior research comparing CMR and standard SPECT MPI, utilizing CZT cameras resulted in a considerable underestimate of ventricular volumes even with 16-frame gating [38].

According to research by Bailliez et al. [42] regional wall thickening was underestimated using CZT (Discovery 530 NMc) camera, particularly in individuals with higher wall thickness.

Coupez et al. [43] discovered the utility of segmental evaluation of LV myocardium thickening in the identification of post-infarction scarring, owing to a strong association of extreme deficiency of thickening found with the device with cadmium zinc telluride detectors and delayed post-contrast segment enhancement in magnetic resonance imagining.

Claudin et al. [40] found high concordance (kappa coefficient 0.72, strict agreement 87%) among the G-SPECT examination using the CZT device and the MRI when comparing LV contractility in 17 segments and assessed visually on a three-point scale: akinesis or dyskinesis, hypokinesis, and normal contractility.

The measurements of LV filling dynamics acquired using CZT camera correspond with echocardiographic diastolic function parameters obtained by echocardiography, boosting the sensitivity in detecting significant ischemic heart disease [44, 45].

Dynamic CZT-SPECT in coronary artery disease

Positron emission tomography (PET) with ^{15}O-water, ^{13}N-ammonia, and ^{82}Rb is the gold standard for assessing myocardial blood flow (MBF) and myocardial flow reserve (MFR) which are reliable indicators of the severity of coronary artery disease. Unfortunately, PET is not generally accessible because of exorbitant costs or the requirement of an on-site cyclotron (for ^{13}N-ammonia and ^{15}O-water) [11]. As a result, techniques based on single-photon emitting radiotracers were proposed as an alternative to PET. The viability of these approaches was demonstrated in several studies using dynamic planar and static SPECT methods [46–48]. Human studies showed that SPECT measurement of MBF and MFR using NaI-based general-purpose SPECT devices is possible [48–52]. Several articles were concentrated on the practicality of dynamic SPECT using CTZ detectors and the association of fractional flow reserve measurements with cardiac PET and invasive coronary angiography [11]. Several investigations have found that MBF and MFR measurements have acceptable intra- and inter-operator repeatability [53–58].

Patients with left main and three-vessel disease (3VD) had the highest risk of mortality due to CAD. The major purpose of noninvasive assessment is to detect this high-risk for whom

revascularization leads to improved symptoms and survival. Lima et al. [59] reported that adjunctive evaluation of function and perfusion by gated SPECT MPI improves identification of abnormalities in multiple vascular areas in patients with severe 3VD without reducing specificity.

It has been established that dynamic SPECT utilizing a CZT camera can help with coronary flow reserve (CFR) evaluation and characterization of high-risk coronary anatomy [60]. The use of dynamic imaging allows for the assessment of blood flow and CFR, which may be employed to diagnose the illness sooner and patients prevent misinterpreting three-vessel disease as normal [61]. Ben Bouallègue et al. [62] analyzed selected high-risk patients with multivessel diseases. They discovered that scintigraphic estimates of global and regional myocardial perfusion reserve in multivessel patients utilizing a CZT camera appear to correspond well with invasive angiographic results such as maximal stenosis and FFR values. According to current evidence, assessing MBF and MFR using a SPECT camera with CZT detectors is more appropriate than semi-quantitative MPI analysis and hence more precise in subjects with multivessel disease [11]. Several investigations utilizing FFR as the reference technique found a high level of concordance between FFR and a SPECT camera with CZT detectors measured MFR values, indicating that these two indices represent the same physiological processes [53, 55, 56, 62, 63]. However, unlike FFR, MFR is known to be affected by both conductive coronary artery stenosis and microvascular resistance [11]. MFR, as opposed to FFR, measures flow in the epicardial arteries and microvasculature. It should be emphasized that an abnormal MFR with a low FFR implies microvascular dysfunction or widespread CAD [3].

Miyagawa et al. [55] observed MFR index (K1 stress/K1 rest) values of 1.57 in the range of 1.45–1.68 for ^{99m}Tc-Tetrofosmin in 16 subjects and 1.61 in the range of 1.46–1.76 for ^{99m}Tc-MIBI in 17 subjects in low-risk of CAD patients. In patients with non-obstructive CAD, the global MFRi was 1.63 in the range of 1.22–2.04. Ben-Haim et al. [64] discovered comparable MFRi values of 1.58 (IQR 1.30–1.75) for the same patient subgroup. These findings are based on limited patient populations. In various studies, the estimates of the quantitative indexes varied between subjects with low-risk and non-obstructive coronary artery disease, indicating the need for more multicenter and multivendor research to establish normal values of CZT-SPECT-derived MBF and MFR [11].

Several researches have shown that regional MFR is reduced in left ventricle regions supplied by coronary arteries having more than 50% obstructive lesion [57, 62, 64]. Ben Bouallegue et al. [62] observed that for flow ratios with a threshold value of 2, regional MFR for diagnosing obstructive lesions had a sensitivity, specificity, and accuracy of 80%, 85%, and 81%, respectively. In diagnosing an obstructive lesion in the corresponding artery, De Souza et al. [57] found a regional MFR sensitivity of 63.2% and specificity of 74.1% with a cutoff of 2.2. In contrast, Nudi et al. [65] discovered no link between MFR and significant obstruction in coronary arteries in CAG.

The gold standard of anatomically diagnosed CAD is quantitative coronary angiography (QCA), which is frequently utilized for risk stratification. The occurrence of a link between QCA and CZT-SPECT is of important clinical relevance. It should be noted that this form of assessment does not entirely correspond to coronary physiology. Obstruction greater than 50% is not necessarily linked with ischemia as shown by invasive FFR. These findings suggest that the appearance of normal MBF and MFR results in locations fed by coronary arteries with lesions of more than 50% does not always represent a false-negative result [11].

The link between regional and global MBF and MFR measurements and other factors, such as coronary artery burden indexes and obstruction severity, the existence of myocardial perfusion deficits, obtained using SPECT camera with CZT detectors and MBF estimated by positron emission tomography, have been studied. Nonetheless, standardization of acquisition and post-processing protocols, also software upgrades, are required to decrease inter-center variability and boost the clinical robustness of the SPECT camera with CZT outcomes [11].

Sympathetic innervation imaging

The link between measurements of regional myocardial adrenergic innervation heterogeneity, mechanical function, and also myocardial perfusion in subjects with CAD has been examined, utilizing a low-dose imaging protocol with a CZT-SPECT camera. A simultaneous assessment of myocardial perfusion and cardiac adrenergic innervations has been done with good image quality, short acquisition time, and a low radiation dose. When obtained using CZT-SPECT, measurements of adrenergic innervation heterogeneity were compared to standard planar indexes and improved the identification of individuals at increased cardiovascular risk by attaching meaningful regional data on myocardial adrenergic nerve activity [66].

The majority of the research is based on pictures obtained with ordinary Anger cameras, with an energy window of 159 keV ± 20% and without attenuation correction. ^{123}I-mIBG imaging using a CZT solid-state camera enables shorter acquisition time and improved energy resolution, allowing for simultaneous capture of adrenergic and perfusion images [67].

CZT-SPECT acquisition in obese patients

Unfortunately, the development of CZT cameras, which have benefits over traditional SPECT devices, does not solve the problem of image quality deterioration caused by obesity [1]. The Discovery NM 530c camera is prone to artifacts in extremely obese individuals due to its limited field of view and pinhole collimation geometry [68, 69]. Fiechter et al. [68] analyzed 81 patients, including 61 obese subjects. In patients with a BMI greater than 40 kg/m^2, image quality was nondiagnostic in 81% of cases, after implementation of CT-based attenuation correction in 55%, respectively. As a result, in the case of The Discovery NM 530c individuals with a BMI of 40 kg/m^2 or higher should be referred for MPI scanning with a standard SPECT camera [1, 68].

This problem does not exist with the D-SPECT camera, and in uncertain cases is generated by diaphragmatic artifacts. It is worth reemphasizing that D-SPECT allows for examinations in two positions: upright and supine [35].

Conclusions

Nuclear cardiac imaging methods continue to be of significant practical importance to cardiologists, thanks to rapid and continuing technological progress and expansion. In comparison to gold

standards used in clinical practice, CZT-SPECT MPI, especially with the dynamic acquisition has excellent diagnostic sensitivity and specificity for CAD diagnosis. While MPI has several advantages in the assessment of coronary artery disease, it does expose individuals to ionizing radiation. Adherence to radiation safety best practices varied greatly amongst laboratories, although the ability to employ CZT-SPECT devices in nuclear cardiology enabled a significant decrease in radiation dose without sacrificing accuracy. To conclude, CZT-SPECT offers good image quality, low radiation dose and quick imaging acquisition for a more effective workflow, resulting in better patient comfort and more imaging protocol flexibility.

Conflict of interest

None declared.

References

1. Acampa W, Buechel RR, Gimelli A. Low dose in nuclear cardiology: state of the art in the era of new cadmium-zinc-telluride cameras. Eur Heart J Cardiovasc Imaging. 2016; 17(6): 591–595, doi: 10.1093/ehjci/jew036, indexed in Pubmed: 26985078.
2. Knuuti J, Wijns W, Saraste A, et al. ESC Scientific Document Group. 2019 ESC Guidelines for the diagnosis and management of chronic coronary syndromes. Eur Heart J. 2020; 41(3): 407–477, doi: 10.1093/eurheartj/ehz425, indexed in Pubmed: 31504439.
3. Panjer M, Dobrolinska M, Wagenaar NRL, et al. Diagnostic accuracy of dynamic CZT-SPECT in coronary artery disease. A systematic review and meta-analysis. J Nucl Cardiol. 2021 [Epub ahead of print], doi: 10.1007/s12350-021-02721-8, indexed in Pubmed: 34350553.
4. Herzog BA, Buechel RR, Katz R, et al. Nuclear myocardial perfusion imaging with a cadmium-zinc-telluride detector technique: optimized protocol for scan time reduction. J Nucl Med. 2010; 51(1): 46–51, doi: 10.2967/jnumed.109.065532, indexed in Pubmed: 20008999.
5. Marcassa C, Bax JJ, Bengel F, et al. European Council of Nuclear Cardiology (ECNC), European Society of Cardiology Working Group 5 (Nuclear Cardiology and Cardiac CT), European Association of Nuclear Medicine Cardiovascular Committee. Clinical value, cost-effectiveness, and safety of myocardial perfusion scintigraphy: a position statement. Eur Heart J. 2008; 29(4): 557–563, doi: 10.1093/eurheartj/ehm607, indexed in Pubmed: 18202253.
6. Picano E, Vañó E, Rehani MM, et al. The appropriate and justified use of medical radiation in cardiovascular imaging: a position document of the ESC Associations of Cardiovascular Imaging, Percutaneous Cardiovascular Interventions and Electrophysiology. Eur Heart J. 2014; 35(10): 665–672, doi: 10.1093/eurheartj/eht394, indexed in Pubmed: 24401558.
7. Borges-Neto S, Pagnanelli RA, Shaw LK, et al. Clinical results of a novel wide beam reconstruction method for shortening scan time of Tc-99m cardiac SPECT perfusion studies. J Nucl Cardiol. 2007; 14(4): 555–565, doi: 10.1016/j.nuclcard.2007.04.022, indexed in Pubmed: 17679065.
8. DePuey EG, Gadiraju R, Clark J, et al. Ordered subset expectation maximization and wide beam reconstruction "half-time" gated myocardial perfusion SPECT functional imaging: a comparison to "full-time" filtered backprojection. J Nucl Cardiol. 2008; 15(4): 547–563, doi: 10.1016/j.nuclcard.2008.02.035, indexed in Pubmed: 18674723.
9. Giorgetti A, Rossi M, Stanislao M, et al. Myoview Imaging Optimization Group. Feasibility and diagnostic accuracy of a gated SPECT early-imaging protocol: a multicenter study of the Myoview Imaging Optimization Group. J Nucl Med. 2007; 48(10): 1670–1675, doi: 10.2967/jnumed.106.039107, indexed in Pubmed: 17873126.
10. Kapur A, Latus KA, Davies G, et al. A comparison of three radionuclide myocardial perfusion tracers in clinical practice: the ROBUST study. Eur J Nucl Med Mol Imaging. 2002; 29(12): 1608–1616, doi: 10.1007/s00259-002-0998-8, indexed in Pubmed: 12458395.
11. Zavadovsky KV, Mochula AV, Maltseva AN, et al. The current status of CZT SPECT myocardial blood flow and reserve assessment: Tips and tricks. J Nucl Cardiol. 2021 [Epub ahead of print], doi: 10.1007/s12350-021-02620-y, indexed in Pubmed: 33939162.
12. Kincl V, Drozdová A, Vašina J, et al. Cadmium-zinc-telluride SPECT scanners - New perspectives in nuclear cardiology. Cor et Vasa. 2015; 57(3): e214–e218, doi: 10.1016/j.crvasa.2015.01.001.
13. Ben-Haim S, Kennedy J, Keidar Z. Novel Cadmium Zinc Telluride Devices for Myocardial Perfusion Imaging-Technological Aspects and Clinical Applications. Semin Nucl Med. 2016; 46(4): 273–285, doi: 10.1053/j.semnuclmed.2016.01.002, indexed in Pubmed: 27237438.
14. Imbert L, Poussier S, Franken PR, et al. Compared performance of high-sensitivity cameras dedicated to myocardial perfusion SPECT: a comprehensive analysis of phantom and human images. J Nucl Med. 2012; 53(12): 1897–1903, doi: 10.2967/jnumed.112.107417, indexed in Pubmed: 23139084.
15. Hudson HM, Larkin RS. Accelerated image reconstruction using ordered subsets of projection data. IEEE Trans Med Imaging. 1994; 13(4): 601–609, doi: 10.1109/42.363108, indexed in Pubmed: 18218538.
16. Buechel RR, Herzog BA, Husmann L, et al. Ultrafast nuclear myocardial perfusion imaging on a new gamma camera with semiconductor detector technique: first clinical validation. Eur J Nucl Med Mol Imaging. 2010; 37(4): 773–778, doi: 10.1007/s00259-009-1375-7, indexed in Pubmed: 20107783.
17. Fiechter M, Ghadri JR, Kuest SM, et al. Nuclear myocardial perfusion imaging with a novel cadmium-zinc-telluride detector SPECT/CT device: first validation versus invasive coronary angiography. Eur J Nucl Med Mol Imaging. 2011; 38(11): 2025–2030, doi: 10.1007/s00259-011-1877-y, indexed in Pubmed: 21761267.
18. Gimelli A, Bottai M, Giorgetti A, et al. Comparison between ultrafast and standard single-photon emission CT in patients with coronary artery disease: a pilot study. Circ Cardiovasc Imaging. 2011; 4(1): 51–58, doi: 10.1161/CIRCIMAGING.110.957399, indexed in Pubmed: 21068188.
19. Verger A, Djaballah W, Fourquet N, et al. Comparison between stress myocardial perfusion SPECT recorded with cadmium-zinc-telluride and Anger cameras in various study protocols. Eur J Nucl Med Mol Imaging. 2013; 40(3): 331–340, doi: 10.1007/s00259-012-2292-8, indexed in Pubmed: 23184308.
20. Soman P, Einstein AJ. Biologic effects of radiation from cardiac imaging: New insights from proteomic and genomic analyses. J Nucl Cardiol. 2016; 23(4): 754–757, doi: 10.1007/s12350-016-0517-0, indexed in Pubmed: 27151300.
21. Gambhir SS, Berman DS, Ziffer J, et al. A novel high-sensitivity rapid-acquisition single-photon cardiac imaging camera. J Nucl Med. 2009; 50(4): 635–643, doi: 10.2967/jnumed.108.060020, indexed in Pubmed: 19339672.
22. Esteves FP, Raggi P, Folks RD, et al. Novel solid-state-detector dedicated cardiac camera for fast myocardial perfusion imaging: multicenter comparison with standard dual detector cameras. J Nucl Cardiol. 2009; 16(6): 927–934, doi: 10.1007/s12350-009-9137-2, indexed in Pubmed: 19688410.
23. Berman DS, Kang X, Tamarappoo B, et al. Stress thallium-201/rest technetium-99m sequential dual isotope high-speed myocardial perfusion imaging. JACC Cardiovasc Imaging. 2009; 2(3): 273–282, doi: 10.1016/j.jcmg.2008.12.012, indexed in Pubmed: 19356571.
24. Duvall WL, Croft LB, Godiwala T, et al. Reduced isotope dose with rapid SPECT MPI imaging: initial experience with a CZT SPECT camera. J Nucl Cardiol. 2010; 17(6): 1009–1014, doi: 10.1007/s12350-010-9215-5, indexed in Pubmed: 21069489.
25. Duvall WL, Croft LB, Ginsberg ES, et al. Reduced isotope dose and imaging time with a high-efficiency CZT SPECT camera. J Nucl Cardiol. 2011; 18(5): 847–857, doi: 10.1007/s12350-011-9379-7, indexed in Pubmed: 21528422.
26. Einstein AJ, Blankstein R, Andrews H, et al. Comparison of image quality, myocardial perfusion, and left ventricular function between standard imaging and single-injection ultra-low-dose imaging using a high-efficiency SPECT

camera: the MILLISIEVERT study. J Nucl Med. 2014; 55(9): 1430–1437, doi: 10.2967/jnumed.114.138222, indexed in Pubmed: 24982439.
27. Sharir T, Ben-Haim S, Merzon K, et al. High-Speed Myocardial Perfusion Imaging. JACC: Cardiovascular Imaging. 2008; 1(2): 156–163, doi: 10.1016/j.jcmg.2007.12.004, indexed in Pubmed: 19356422.
28. Cantoni V, Green R, Acampa W, et al. Diagnostic performance of myocardial perfusion imaging with conventional and CZT single-photon emission computed tomography in detecting coronary artery disease: A meta-analysis. J Nucl Cardiol. 2021; 28(2): 698–715, doi: 10.1007/s12350-019-01747-3, indexed in Pubmed: 31089962.
29. Nudi F, Iskandrian AE, Schillaci O, et al. Diagnostic Accuracy of Myocardial Perfusion Imaging With CZT Technology: Systemic Review and Meta-Analysis of Comparison With Invasive Coronary Angiography. JACC Cardiovasc Imaging. 2017; 10(7): 787–794, doi: 10.1016/j.jcmg.2016.10.023, indexed in Pubmed: 28330657.
30. Zhang YQ, Jiang YF, Hong Lu, et al. Diagnostic value of cadmium-zinc-telluride myocardial perfusion imaging versus coronary angiography in coronary artery disease: A PRISMA-compliant meta-analysis. Medicine (Baltimore). 2019; 98(9): e14716, doi: 10.1097/MD.0000000000014716, indexed in Pubmed: 30817614.
31. Gimelli A, Liga R, Duce V, et al. Accuracy of myocardial perfusion imaging in detecting multivessel coronary artery disease: A cardiac CZT study. J Nucl Cardiol. 2017; 24(2): 687–695, doi: 10.1007/s12350-015-0360-8, indexed in Pubmed: 26846367.
32. Esteves FP, Galt JR, Folks RD, et al. Diagnostic performance of low-dose rest/stress Tc-99m tetrofosmin myocardial perfusion SPECT using the 530c CZT camera: quantitative vs visual analysis. J Nucl Cardiol. 2014; 21(1): 158–165, doi: 10.1007/s12350-013-9827-7, indexed in Pubmed: 24287713.
33. Mirshahvalad SA, Chavoshi M, Hekmat S. Diagnostic performance of prone-only myocardial perfusion imaging versus coronary angiography in the detection of coronary artery disease: A systematic review and meta-analysis. J Nucl Cardiol. 2022; 29(3): 1339–1351, doi: 10.1007/s12350-020-02376-x, indexed in Pubmed: 33025477.
34. Nishiyama Y, Miyagawa M, Kawaguchi N, et al. Combined supine and prone myocardial perfusion single-photon emission computed tomography with a cadmium zinc telluride camera for detection of coronary artery disease. Circ J. 2014; 78(5): 1169–1175, doi: 10.1253/circj.cj-13-1316, indexed in Pubmed: 24572492.
35. Nakazato R, Tamarappoo BK, Kang X, et al. Quantitative upright-supine high-speed SPECT myocardial perfusion imaging for detection of coronary artery disease: correlation with invasive coronary angiography. J Nucl Med. 2010; 51(11): 1724–1731, doi: 10.2967/jnumed.110.078782, indexed in Pubmed: 20956478.
36. Perrin M, Roch V, Claudin M, et al. Assessment of Myocardial CZT SPECT Recording in a Forward-Leaning Bikerlike Position. J Nucl Med. 2019; 60(6): 824–829, doi: 10.2967/jnumed.118.217695, indexed in Pubmed: 30389818.
37. Abidov A, Germano G, Hachamovitch R, et al. Gated SPECT in assessment of regional and global left ventricular function: major tool of modern nuclear imaging. J Nucl Cardiol. 2006; 13(2): 261–279, doi: 10.1007/BF02971251, indexed in Pubmed: 16580963.
38. Cochet H, Bullier E, Gerbaud E, et al. Absolute quantification of left ventricular global and regional function at nuclear MPI using ultrafast CZT SPECT: initial validation versus cardiac MR. J Nucl Med. 2013; 54(4): 556–563, doi: 10.2967/jnumed.112.110577, indexed in Pubmed: 23385955.
39. Giorgetti A, Masci PG, Marras G, et al. Gated SPECT evaluation of left ventricular function using a CZT camera and a fast low-dose clinical protocol: comparison to cardiac magnetic resonance imaging. Eur J Nucl Med Mol Imaging. 2013; 40(12): 1869–1875, doi: 10.1007/s00259-013-2505-9, indexed in Pubmed: 23884280.
40. Claudin M, Imbert L, Djaballah W, et al. Routine evaluation of left ventricular function using CZT-SPECT, with low injected activities and limited recording times. J Nucl Cardiol. 2018; 25(1): 249–256, doi: 10.1007/s12350-016-0615-z, indexed in Pubmed: 27677613.
41. Sala M, Kincl V, Kamínek M, et al. Assessment of left ventricular volumes and ejection fraction using ultra-low-dose thallium-201 SPECT on a CZT camera: a comparison with magnetic resonance imaging. J Nucl Cardiol. 2022; 29(1): 181–187, doi: 10.1007/s12350-020-02161-w, indexed in Pubmed: 32410056.
42. Bailliez A, Blaire T, Mouquet F, et al. Segmental and global left ventricular function assessment using gated SPECT with a semiconductor Cadmium Zinc Telluride (CZT) camera: phantom study and clinical validation vs cardiac magnetic resonance. J Nucl Cardiol. 2014; 21(4): 712–722, doi: 10.1007/s12350-014-9899-z, indexed in Pubmed: 24810429.
43. Coupez E, Merlin C, Tuyisenge V, et al. Validation of cadmium-zinc-telluride camera for measurement of left ventricular systolic performance. J Nucl Cardiol. 2018; 25(3): 1029–1036, doi: 10.1007/s12350-017-0816-0, indexed in Pubmed: 28194726.
44. Gimelli A, Liga R, Pasanisi EM, et al. Evaluation of left ventricular diastolic function with a dedicated cadmium-zinc-telluride cardiac camera: comparison with Doppler echocardiography. Eur Heart J Cardiovasc Imaging. 2014; 15(9): 972–979, doi: 10.1093/ehjci/jeu037, indexed in Pubmed: 24618658.
45. Gimelli A, Liga R, Bottai M, et al. Diastolic dysfunction assessed by ultra-fast cadmium-zinc-telluride cardiac imaging: impact on the evaluation of ischaemia. Eur Heart J Cardiovasc Imaging. 2015; 16(1): 68–73, doi: 10.1093/ehjci/jeu166, indexed in Pubmed: 25187611.
46. Gullberg GT, Di Bella EV, Sinusas AJ. Estimation of coronary flow reserve: can SPECT compete with other modalities? J Nucl Cardiol. 2001; 8(5): 620–625, doi: 10.1067/mnc.2001.118121, indexed in Pubmed: 11593228.
47. Iida H, Eberl S, Kim KM, et al. Absolute quantitation of myocardial blood flow with (201)Tl and dynamic SPECT in canine: optimisation and validation of kinetic modelling. Eur J Nucl Med Mol Imaging. 2008; 35(5): 896–905, doi: 10.1007/s00259-007-0654-4, indexed in Pubmed: 18202845.
48. Hsu B, Hu LH, Yang BH, et al. SPECT myocardial blood flow quantitation toward clinical use: a comparative study with N-Ammonia PET myocardial blood flow quantitation. Eur J Nucl Med Mol Imaging. 2017; 44(1): 117–128, doi: 10.1007/s00259-016-3491-5, indexed in Pubmed: 27585576.
49. Sugihara H, Yonekura Y, Kataoka K, et al. Estimation of coronary flow reserve with the use of dynamic planar and SPECT images of Tc-99m tetrofosmin. J Nucl Cardiol. 2001; 8(5): 575–579, doi: 10.1067/mnc.2001.115934, indexed in Pubmed: 11593222.
50. Klein R, Hung GU, Wu TC, et al. Feasibility and operator variability of myocardial blood flow and reserve measurements with mTc-sestamibi quantitative dynamic SPECT/CT imaging. J Nucl Cardiol. 2014; 21(6): 1075–1088, doi: 10.1007/s12350-014-9971-8, indexed in Pubmed: 25280761.
51. Winant CD, Aparici CM, Zelnik YR, et al. Investigation of dynamic SPECT measurements of the arterial input function in human subjects using simulation, phantom and human studies. Phys Med Biol. 2012; 57(2): 375–393, doi: 10.1088/0031-9155/57/2/375, indexed in Pubmed: 22170801.
52. Shrestha U, Sciammarella M, Alhassen F, et al. Measurement of absolute myocardial blood flow in humans using dynamic cardiac SPECT and Tc-tetrofosmin: Method and validation. J Nucl Cardiol. 2017; 24(1): 268–277, doi: 10.1007/s12350-015-0320-3, indexed in Pubmed: 26715603.
53. Agostini D, Roule V, Nganoa C, et al. First validation of myocardial flow reserve assessed by dynamic Tc-sestamibi CZT-SPECT camera: head to head comparison with O-water PET and fractional flow reserve in patients with suspected coronary artery disease. The WATERDAY study. Eur J Nucl Med Mol Imaging. 2018; 45(7): 1079–1090, doi: 10.1007/s00259-018-3958-7, indexed in Pubmed: 29497801.
54. Otaki Y, Manabe O, Miller RJH, et al. Quantification of myocardial blood flow by CZT-SPECT with motion correction and comparison with O-water PET. J Nucl Cardiol. 2021; 28(4): 1477–1486, doi: 10.1007/s12350-019-01854-1, indexed in Pubmed: 31452085.
55. Miyagawa M, Nishiyama Y, Uetani T, et al. Estimation of myocardial flow reserve utilizing an ultrafast cardiac SPECT: Comparison with coronary angiography, fractional flow reserve, and the SYNTAX score. Int J Cardiol. 2017; 244: 347–353, doi: 10.1016/j.ijcard.2017.06.012, indexed in Pubmed: 28622946.

56. Han S, Kim YH, Ahn JM, et al. Feasibility of dynamic stress Tl/rest Tc-tetrofosmin single photon emission computed tomography for quantification of myocardial perfusion reserve in patients with stable coronary artery disease. Eur J Nucl Med Mol Imaging. 2018; 45(12): 2173–2180, doi: 10.1007/s00259-018-4057-5, indexed in Pubmed: 29858614.
57. de Souza AC, Gonçalves BKD, Tedeschi AL, et al. Quantification of myocardial flow reserve using a gamma camera with solid-state cadmium-zinc-telluride detectors: Relation to angiographic coronary artery disease. J Nucl Cardiol. 2021; 28(3): 876–884, doi: 10.1007/s12350-019-01775-z, indexed in Pubmed: 31222529.
58. Wells RG, Radonjic I, Clackdoyle D, et al. Test-Retest Precision of Myocardial Blood Flow Measurements With Tc-Tetrofosmin and Solid-State Detector Single Photon Emission Computed Tomography. Circ Cardiovasc Imaging. 2020; 13(2): e009769, doi: 10.1161/CIRCIMAGING.119.009769, indexed in Pubmed: 32069116.
59. Lima R, Watson D, Goode A, et al. Incremental value of combined perfusion and function over perfusion alone by gated SPECT myocardial perfusion imaging for detection of severe three-vessel coronary artery disease. J Am Coll Cardiol. 2003; 42(1): 64–70, doi: 10.1016/s0735-1097(03)00562-x, indexed in Pubmed: 12849661.
60. Slomka PJ, Berman DS, Germano G. Absolute myocardial blood flow quantification with SPECT/CT: is it possible? J Nucl Cardiol. 2014; 21(6): 1092–1095, doi: 10.1007/s12350-014-0002-6, indexed in Pubmed: 25294433.
61. Shiraishi S, Sakamoto F, Tsuda N, et al. Prediction of left main or 3-vessel disease using myocardial perfusion reserve on dynamic thallium-201 single-photon emission computed tomography with a semiconductor gamma camera. Circ J. 2015; 79(3): 623–631, doi: 10.1253/circj.CJ-14-0932, indexed in Pubmed: 25746547.
62. Ben Bouallègue F, Roubille F, Lattuca B, et al. SPECT Myocardial Perfusion Reserve in Patients with Multivessel Coronary Disease: Correlation with Angiographic Findings and Invasive Fractional Flow Reserve Measurements. J Nucl Med. 2015; 56(11): 1712–1717, doi: 10.2967/jnumed.114.143164, indexed in Pubmed: 26338893.
63. Zavadovsky KV, Mochula AV, Boshchenko AA, et al. Absolute myocardial blood flows derived by dynamic CZT scan vs invasive fractional flow reserve: Correlation and accuracy. J Nucl Cardiol. 2021; 28(1): 249–259, doi: 10.1007/s12350-019-01678-z, indexed in Pubmed: 30847856.
64. Ben-Haim S, Murthy VL, Breault C, et al. Quantification of Myocardial Perfusion Reserve Using Dynamic SPECT Imaging in Humans: A Feasibility Study. J Nucl Med. 2013; 54(6): 873–879, doi: 10.2967/jnumed.112.109652, indexed in Pubmed: 23578996.
65. Nudi F, Biondi-Zoccai G, Nudi A, et al. Comparative analysis between myocardial perfusion reserve and maximal ischemia score at single photon emission computed tomography with new-generation cadmium-zinc-telluride cameras. J Nucl Cardiol. 2021; 28(3): 1072–1084, doi: 10.1007/s12350-019-01764-2, indexed in Pubmed: 31152316.
66. Gimelli A, Liga R, Giorgetti A, et al. Assessment of myocardial adrenergic innervation with a solid-state dedicated cardiac cadmium-zinc-telluride camera: first clinical experience. Eur Heart J Cardiovasc Imaging. 2014; 15(5): 575–585, doi: 10.1093/ehjci/jet258, indexed in Pubmed: 24351314.
67. Wan N, Travin MI. Cardiac Imaging With I-meta-iodobenzylguanidine and Analogous PET Tracers: Current Status and Future Perspectives. Semin Nucl Med. 2020; 50(4): 331–348, doi: 10.1053/j.semnuclmed.2020.03.001, indexed in Pubmed: 32540030.
68. Fiechter M, Gebhard C, Fuchs TA, et al. Cadmium-zinc-telluride myocardial perfusion imaging in obese patients. J Nucl Med. 2012; 53(9): 1401–1406, doi: 10.2967/jnumed.111.102434, indexed in Pubmed: 22870823.
69. Budzyńska A, Osiecki S, Mazurek A, et al. Feasibility of myocardial perfusion imaging studies in morbidly obese patients with a cadmium-zinc-telluride cardiac camera. Nucl Med Rev Cent East Eur. 2019; 22(1): 18–22, doi: 10.5603/NMR.2019.0003, indexed in Pubmed: 31482538.

VIA MEDICA

Nuclear Medicine Review 2022, 25, 2: 127–128
DOI: 10.5603/NMR.a2022.0026

ISSN 1506–9680, e-ISSN 1644–4345

Clinical vignette

^{99m}Tc-Vitamin C SPECT/CT imaging in SARS-CoV-2 associated pneumonia

Haluk B. Sayman[1], Kubra N. Toplutas[1], James Tunick[2], Omer Aras[3]

[1]Cerrahpasa Medical Faculty, Department of Nuclear Medicine, Istanbul University-Cerrahpasa, Istanbul,Turkey
[2]The IMC Lab, New York, United States
[3]Departament of Radiology, Memorial Sloan Kettering Cancer Center, New York, United States

[Received 5 IX 2021; Accepted 5 IV 2022]

Abstract

We present the first ^{99m}Tc-Vitamin C single-photon emission computed tomography/computed tomography (SPECT/CT) images obtained in patients with SARS-CoV-2 (COVID-19) infection. The CT portion of SPECT/CT images showed mostly peripheral patchy and ground-glass opacities in both lungs, which are consistent with a diagnosis of SARS-CoV-2–associated pneumonia in both patients. ^{99m}Tc-Vitamin C SPECT images showed increased tracer uptake corresponding to abnormal lung findings seen on CT in patient 1 who was newly diagnosed and treatment naïve. However, no abnormal uptake corresponding to lung CT findings was seen in patient 2 who received anti-SARS-CoV-2 treatment.

KEY words: ^{99m}Tc-Vitamin C; SPECT/CT; SARS-Cov-2, pneumonia

Nucl Med Rev 2022; 25, 2: 127–128

High-dose intravenous vitamin C may reduce systemic inflammation by decreasing cytokine surge and preventing lung injury in severe sepsis and acute respiratory distress syndrome [1]. It may also be beneficial in patients with severe acute respiratory syndrome coronavirus 2 (SARS-CoV-2; COVID-19) infection; we present the first lung ^{99m}Tc-Vitamin C SPECT/CT images in these patients [2]. Patient 1, a 31-year-old woman, was diagnosed with severe acute respiratory syndrome coronavirus 2 (SARS-CoV-2) infection based on a nasopharyngeal and oropharyngeal swab taken for SARS-CoV-2 during a screening, which was performed due to close contact with a positive case. She was mildly symptomatic, complaining of chest pain and cough without fever, cyanosis, clubbing, pursed lips expiration, use of accessory respiratory muscles, and nasal flaring. The patient was admitted and monitored. Results of the physical examination, including the chest examination, were unremarkable. On day 1 of admission, CT images showed mostly peripheral patchy and ground-glass opacities in both lungs (Fig. 1A: 3D colored volume-rendered images of CT, lung findings on CT, black arrows), consistent with SARS-CoV-2–associated pneumonia. ^{99m}Tc-Vitamin C SPECT images showed increased tracer uptake corresponding to abnormal lung findings (fused images of SPECT/CT: top image, with physiologic blood pool uptake; bottom image, with digitally suppressed blood pool). After treatment, findings resolved with no abnormal uptake on follow-up SPECT/CT at 3 months (Fig. 1B). Patient 2, a 20-year-old woman with dry cough, and chest and muscle pain, was found positive for SARS-CoV-2 based on real-time RT-PCR testing of a nasopharyngeal swab specimen obtained on the day of admission. She had similar lung findings on CT as patient 1 although she had already been receiving standard anti-viral and anti-inflammatory treatment; however, on the 5th day of hospitalization, ^{99m}Tc-Vitamin C SPECT images showed no abnormal uptake corresponding to lung CT findings (Fig. 1C), indicating that anti-SARS-CoV-2 treatment inhibited Vitamin C uptake.

There are several cases reported of SARS-CoV-2 pneumonia and the accumulation of different nuclear medicine tracers, including ^{18}F-FDG, ^{18}F-Fluorocholine, ^{68}Gal PSMA, ^{68}Ga-DOTANOC, ^{99m}Tc-leukocyte, and ^{99m}Tc-MAA [3–8].

Vitamin C could be beneficial as a supportive treatment of sepsis and septic shock, which are common complications associated with SARS-CoV-2, by suppressing the excessive cytokine release which leads to sepsis-induced organ dysfunction and by protecting the lungs against oxidative stress. The results from these cases suggest that it could also have a detrimental effect on the SARS CoV-2 virus given its local uptake in lung lesions that are typical of SARS CoV-2 induced pneumonitis. Therefore, these cases suggest that ^{99m}Tc-Vitamin C imaging is a promising non-invasive approach to identify the presence of lung damage as well as to potentially monitor the persistence and progression of lung damage.

Correspondence to: Omer Aras, Departament of Radiology, Memorial Sloan Kettering Cancer Center, 300 East 66th Street, Suite 1511, New York, NY 10065, United States
e-mail: dromeraras@gmail.com or araso@mskcc.org

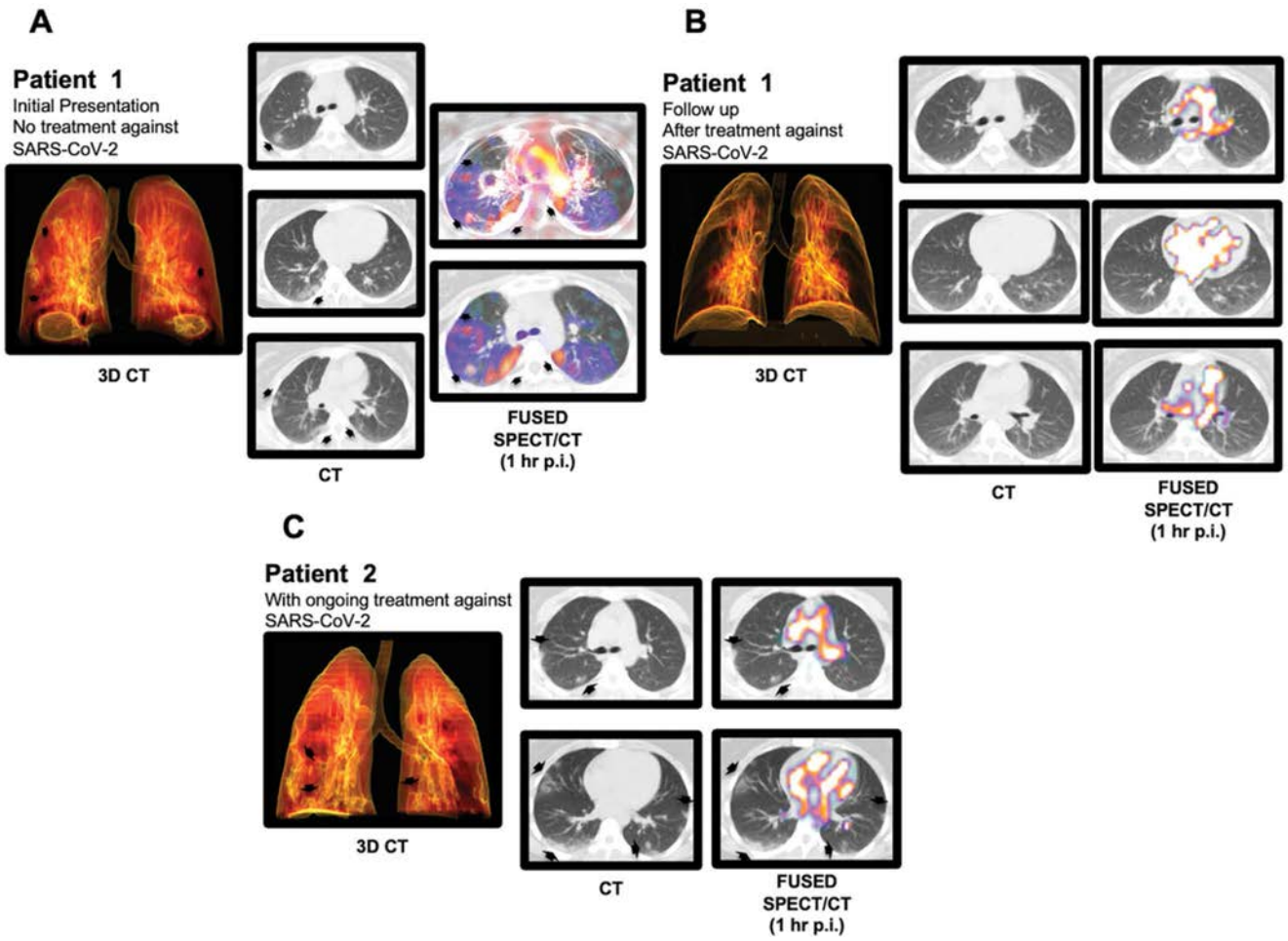

Figure 1. 3D and axial CT images showed pulmonary findings consistent with SARS-CoV-2–associated pneumonia in patient 1 and ^{99m}Tc-Vitamin C SPECT images showed increased tracer uptake corresponding to abnormal lung findings (**A**) and resolution of both CT and SPECT imaging findings on the follow-up study (**B**). In patient 2, 3D and axial CT images showed similar lung findings as patient 1; however, ^{99m}Tc-Vitamin C SPECT images showed no abnormal uptake corresponding to lung CT findings in patient 2 (**C**)

Conflict of interest

The authors declare no competing interests.

Funding

This research was also funded in part through the NIH/NCI Cancer Center Support Grant P30 CA008748.

References

1. Boretti A, Banik BK. Intravenous vitamin C for reduction of cytokines storm in acute respiratory distress syndrome. PharmaNutrition. 2020; 12: 100190, doi: 10.1016/j.phanu.2020.100190, indexed in Pubmed: 32322486.
2. Zhang J, Rao X, Li Y, et al. Pilot trial of high-dose vitamin C in critically ill COVID-19 patients. Ann Intensive Care. 2021; 11(1): 5, doi: 10.1186/s13613-020-00792-3, indexed in Pubmed: 33420963.
3. Albano D, Bertagna F, Bertoli M, et al. Incidental Findings Suggestive of COVID-19 in Asymptomatic Patients Undergoing Nuclear Medicine Procedures in a High-Prevalence Region. J Nucl Med. 2020; 61(5): 632–636, doi: 10.2967/jnumed.120.246256, indexed in Pubmed: 32238429.
4. García Vicente AM, Soriano Castrejón Á. Incidental COVID-19 Pneumonia on 18F-Fluorocholine PET/CT. Clin Nucl Med. 2020; 45(8): e376–e377, doi: 10.1097/RLU.0000000000003189, indexed in Pubmed: 32520514.
5. Stasiak CE, Cardoso FR, de Almeida SA, et al. Incidental finding of COVID-19 infection after [Ga]Ga-PSMA-11 PET/CT imaging in a patient with prostate cancer. Eur J Nucl Med Mol Imaging. 2021; 48(2): 653–654, doi: 10.1007/s00259-020-04932-6, indexed in Pubmed: 32710224.
6. Morón S, González E, Rojas J. 68Ga-DOTANOC PET/CT With Lung Involvement in the Era of COVID-19 Pandemic. Clin Nucl Med. 2021; 46(2): 166–167, doi: 10.1097/RLU.0000000000003473, indexed in Pubmed: 33234942.
7. Zheng J, Liu Y. 99mTc-Leukocyte Scintigraphy Revealed Viral Pulmonary Infection in a COVID-19 Patient. Clin Nucl Med. 2020; 45(10): 821–823, doi: 10.1097/RLU.0000000000003219, indexed in Pubmed: 32701817.
8. Burger IA, Niemann T, Patriki D, et al. Lung perfusion [Tc]-MAA SPECT/CT to rule out pulmonary embolism in COVID-19 patients with contraindications for iodine contrast. Eur J Nucl Med Mol Imaging. 2020; 47(9): 2209–2210, doi: 10.1007/s00259-020-04862-3, indexed in Pubmed: 32451602.

VIA MEDICA

Nuclear Medicine Review 2022, 25, 2: 129–130
DOI: 10.5603/NMR.a2022.0027

ISSN 1506–9680, e-ISSN 1644–4345

Clinical vignette

Radiopharmaceutical for detecting PSMA — positive metastatic colon cancer: Matched-pair comparison of ^{18}F-BF3-Cy3-ACUPA and ^{68}Ga-PSMA PET/MRI

Omer Aras[1], Cetin Demirdag[2], Harikrishna Kommidi[3], Richard Ting[3], Haluk B. Sayman[4]

[1]Departament of Radiology, Memorial Sloan Kettering Cancer Center, New York, United States
[2]Department of Urology, Cerrahpasa Medical Faculty, Istanbul, Turkey
[3]Department of Radiology, Weill Cornell Medicine, New York, United States
[4]Department of Nuclear Medicine, Cerrahpasa Medical Faculty, Istanbul University-Cerrahpasa, Istanbul,Turkey

[Received 5 IX 2021; Accepted 1 IV 2022]

Abstract

Prostate-specific membrane antigen (PSMA) — based radiopharmaceuticals are promising for the evaluation of PSMA-positive non-prostate cancers. In this case study, ^{18}F-BF3-Cy3-ACUPA and ^{68}Ga-PSMA positron emission tomography/magnetic resonance imaging (PET/MRI) were compared in a patient with metastatic colon cancer. Both ^{18}F-BF3-Cy3-ACUPA and ^{68}Ga-PSMA PET/MRI showed biopsy-proven metastatic left external iliac adenopathy, highlighting the feasibility of PSMA uptake in PET/MRI of metastatic nodal disease from colon cancer. Along with imaging evaluation, PSMA-based radiopharmaceuticals may also be used as a surrogate imaging tracer for potential theranostic applications using alpha or beta emitters in the context of PSMA-directed radiopharmaceutical therapy in advanced and progressive colorectal cancer.

KEY words: ^{18}F-BF3-Cy3-ACUPA; ^{68}Ga-PSMA; colorectal cancer; PET/MRI; PSMA

Nucl Med Rev 2022; 25, 2: 129–130

Prostate-specific membrane antigen (PSMA) — based radiopharmaceuticals are promising for the evaluation of PSMA-positive non-prostate cancers. In this case study, ^{18}F-BF3-Cy3-ACUPA and ^{68}Ga-PSMA positron emission tomography/magnetic resonance imaging (PET/MRI) were compared in a patient with metastatic colon cancer. A 57-year-old man underwent prostate-specific membrane antigen (PSMA) imaging for restaging of his colon cancer. Previously, he had been diagnosed with adenocarcinoma in the colon, undergone resection, and received chemotherapy; he developed nodal metastatic disease and received immunotherapy prior to PSMA imaging. To further evaluate the metastatic disease, he was enrolled in and provided informed consent for a clinical trial of ^{18}F-BF3-Cy3-ACUPA and ^{68}Ga-PSMA positron emission tomography/magnetic resonance imaging (PET/MRI) approved by the institutional review board. ^{68}Ga-PSMA PET/MRI for metastatic workup showed mildly increased radiotracer avidity in the left external iliac region on the

Correspondence to: Omer Aras, Departament of Radiology, Memorial Sloan Kettering Cancer Center, 300 East 66th Street, Suite 1511, New York, NY 10065, United States
e-mail: dromeraras@gmail.com or araso@mskcc.org

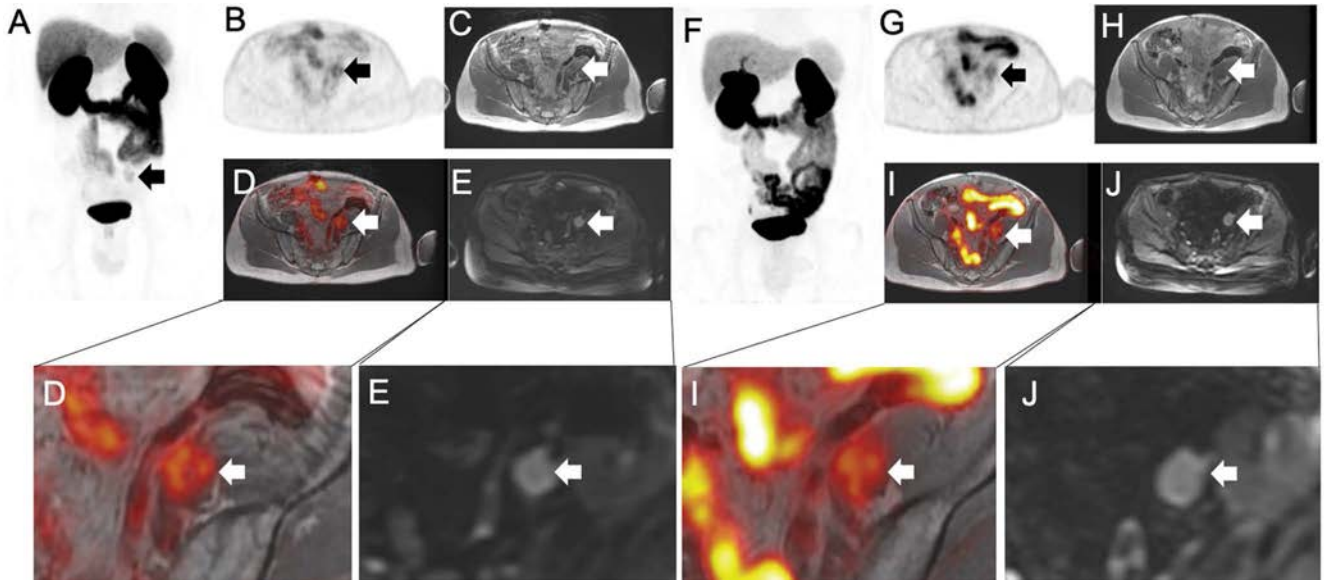

Figure 1. ^{68}Ga-PSMA PET/MRI showed mildly increased radiotracer avidity in the left external iliac region on the body maximum intensity projection (MIP) image (**A**, arrow), which was localized to moderate radiotracer uptake (**B**, arrow, PET) in the enlarged left external iliac node (**C**, MRI) (**D**, fused PET/MRI) with restricted diffusion (**E**, arrow, diffusion-weighted imaging (DWI)). ^{18}F-BF3-Cy3-ACUPA PET/MRI showed increased abnormal radiotracer avidity in the left iliac node (**F**, body MIP; difficult to delineate due to overlying bowel activity; **G**, arrow, PET and **H**, MRI and **I**, fused PET/MRI) with restricted diffusion (**J**, arrow, DWI MRI).

body maximum intensity projection (MIP) image (Fig. 1A, arrow), which was localized to moderate radiotracer uptake (Fig. 1B, arrow, PET; SUVmax, 3.4; liver background activity, SUV mean, 4.6 and blood pool activity, SUV mean, 0.7) in the enlarged left external iliac node (Fig. 1C, MRI) (Fig. 1D, fused PET/MRI) with restricted diffusion [Fig. 1E, arrow, diffusion-weighted imaging (DWI)]. Two weeks later, ^{18}F-BF3-Cy3-ACUPA was performed to confirm the previous findings on ^{68}Ga-PSMA PET/MR [1]. ^{18}F-BF3-Cy3-ACUPA PET/MRI showed increased abnormal radiotracer avidity in the left iliac node (Fig. 1F, body MIP; difficult to delineate due to overlying bowel activity; Fig. 1G, arrow, PET and Fig. 1H, MRI and Fig. 1I, fused PET/MRI; SUVmax, 3.2; liver background activity, SUV mean, 3.5 and blood pool activity, SUV mean, 0.8) with restricted diffusion (Fig. 1J, arrow, DWI MRI). To our knowledge, we here display the first clinical images of matched-pair comparison of ^{18}F-BF3-Cy3-ACUPA and ^{68}Ga-PSMA PET/MRI in a patient with metastatic colon cancer. Several case reports have reported PSMA avidity in colorectal cancer, potentially supporting PSMA-targeted peptide receptor radionuclide therapy (PRRT) in advanced colorectal cancer [2–4] However, in a recent report with 10 patients with metastatic colorectal cancer, ^{68}Ga-PSMA-11 PET/CT was not sensitive enough to detect metastatic colorectal cancer, indicating that it is not as promising for PSMA-PRRT [5]. Along with imaging evaluation, PSMA-based radiopharmaceuticals may also be used as a surrogate imaging tracer for potential theranostic applications using alpha or beta emitters in the context of PSMA-directed radiopharmaceutical therapy in advanced and progressive colorectal cancer.

Conflict of interest

Richard Ting and Omer Aras are minor stakeholders in Trace Imaging Technologies. The other authors declare that they have no conflict of interest.

Funding

Omer Aras was partially funded by NIH/NCI Cancer Center Support Grant P30 CA008748

References

1. Aras O, Demirdag C, Kommidi H, et al. Simultaneous injection of 18 F-BF3- Cy3-ACUPA and non-radioactive Cy7-ACUPA probes: a promising pre-biopsy PET and ex vivo fluorescence imaging approach to evaluate prostate cancer . Eur J Nucl Med Mol Imaging. 2021; 48(11): 3732–3733, doi: 10.1007/s00259-021-05344-w, indexed in Pubmed: 33860854.
2. Hangaard L, Jochumsen MR, Vendelbo MH, et al. Metastases From Colorectal Cancer Avid on 68Ga-PSMA PET/CT. Clin Nucl Med. 2017; 42(7): 532–533, doi: 10.1097/RLU.0000000000001700, indexed in Pubmed: 28525451.
3. Huang YTT, Fong W, Thomas P. Rectal Carcinoma on 68Ga-PSMA PET/CT. Clin Nucl Med. 2016; 41(3): e167–e168, doi: 10.1097/RLU.0000000000001072, indexed in Pubmed: 26571447.
4. Cuda TJ, Riddell AD, Liu C, et al. PET Imaging Quantifying Ga-PSMA-11 Uptake in Metastatic Colorectal Cancer. J Nucl Med. 2020; 61(11): 1576–1579, doi: 10.2967/jnumed.119.233312, indexed in Pubmed: 32358088.
5. Salas Fragomeni RA, Amir T, Sheikhbahaei S, et al. Imaging of Nonprostate Cancers Using PSMA-Targeted Radiotracers: Rationale, Current State of the Field, and a Call to Arms. J Nucl Med. 2018; 59(6): 871–877, doi: 10.2967/jnumed.117.203570, indexed in Pubmed: 29545375.

VIA MEDICA

Nuclear Medicine Review 2022, 25, 2: 131–133
DOI: 10.5603/NMR.a2022.0028

ISSN 1506–9680, e-ISSN 1644–4345

Clinical vignette

A crying liver: a scan pattern mimicking spontaneous perforation of the biliary ducts

Somaye Barashki[1], Hadis Mohammadzadeh Kosari[1], Emran Askari[1], Zahra Bakhshi Golestani[1], Mehran Hiradfar[2], Ramin Sadeghi[1]

[1]Nuclear Medicine Research Center, Mashhad University of Medical Sciences, Mashhad, Iran
[2]Department of Pediatric Surgery, Mashhad University of Medical Sciences, Mashhad, Iran

[Received 27 IV 2021; Accepted 27 IV 2022]

Abstract

A 2-month-old infant was referred for hepatobiliary scintigraphy due to ascites of unknown cause. The top differential diagnosis was spontaneous perforation of the biliary ducts. Delayed images up to 4 hours were against this diagnosis showing normal distribution of the radiotracer throughout the bowel. However, on delayed images, the scan showed mild tracer retention in the ascites confirmed by SPECT/CT images. Surprisingly, the exploratory abdominal surgery revealed an intact hepatobiliary system, pointing toward other possible etiologies. Second-review surgery was performed due to uncontrolled progressive ascites showing congestive hepatopathy and biliary leak from the hepatic surface suggestive of the "crying liver".

KEY words: hepatobiliary scintigraphy; crying liver; biliary leak

Nucl Med Rev 2022; 25, 2: 131–133

Hepatobiliary scintigraphy (HBS) is a well-known diagnostic method for the evaluation of bile duct disease and biliary leak. Several studies have reported that HBS has played an important role in diagnosing spontaneous biliary leak, especially when associated with single photon emission computed tomography/computed tomography (SPECT/CT) [1–6].

A 2-month-old female pediatric patient presenting with abdominal distension since 5 days ago and suspicion of spontaneous perforation of the common bile duct was referred to the nuclear medicine department for hepatobiliary scintigraphy (HBS). Laboratory examination showed elevated total and direct bilirubin levels (4.1 and 2.1 mg/dL, respectively) and high alkaline phosphatase (556 IU/L). Abdominal ultrasonography showed ascites with a normal appearance of liver parenchyma, gallbladder, biliary ducts, and portal vein. Ascites fluid analysis was inconclusive for biliary ascites showing borderline elevation of the total bilirubin (1.5 mg/dL) [7]. Hepatobiliary scintigraphy (HBS) was performed after an intravenous injection of 37 MBq of ^{99m}Tc-mebrofenin. Dynamic imaging showed normal hepatic uptake and normal intra- and extra-hepatic ducts (Fig. 1A). Delayed static images 2 and 4 hours after injection demonstrated no abnormal radiotracer activity outside the biliary system and intestinal tract (Fig. 1B, C). To increase the sensitivity for detection of bile leakage, 24-hour delayed imaging was also performed showing an accumulation of the tracer throughout the peritoneum (Fig. 1D) [8, 9].

Single photon emission computed tomography/computed tomography (SPECT/CT) images from the abdominal region confirmed the presence of activity in the ascites fluid (Fig. 2). The presence of radiotracer activity in the ascites fluid on the delayed images raised the possibility of biliary tract perforation. During the exploratory abdominal surgery, the hepatobiliary system was intact but there was a large omental cyst as well as intestinal malrotation with a large amount of yellowish free fluid in the peritoneal cavity. Surgical correction was done by resecting the omental cyst with correction of the intestinal malrotation. Owing to progressive abdominal distention, further, work-up was carried out showing increased ascites in the abdominal cavity. The patient underwent second-look surgery. No culprit pathology was found in the exploratory surgery except for superficial bile leak from the hepatic surface and the appearance of liver congestion suggestive of the "crying liver" [10, 11]. The final diagnosis was in favor of

Correspondence to: Ramin Sadeghi, Nuclear Medicine Research Center, Mashhad University of Medical Sciences, Mashhad, Iran, phone: +985138012794, e-mail: sadeghir@mums.ac.ir; raminsadeghi1355@yahoo.com

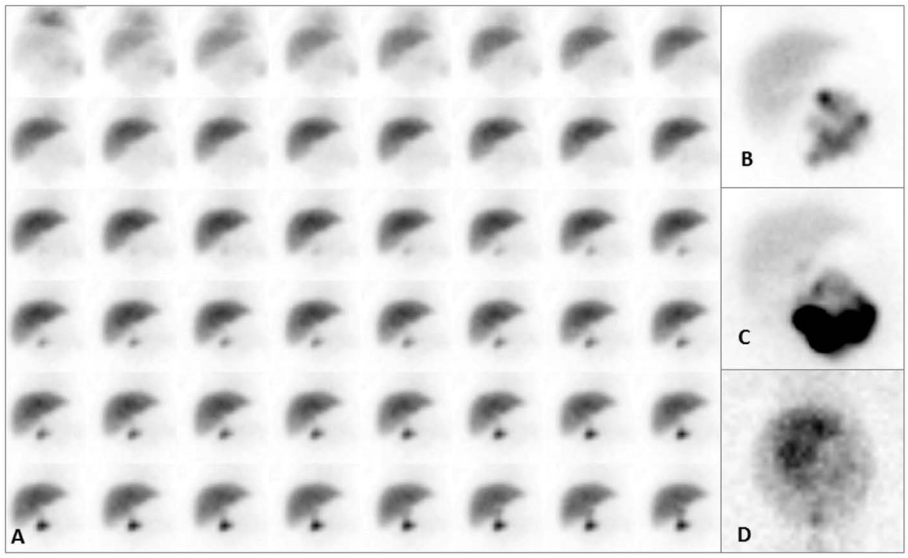

Figure 1. (**A**) Dynamic imaging from the abdominal region in anterior view showed normal hepatic uptake and biliary ducts with normal excretion of the radiotracer into the intestine; (**B**) Static image 2 hours after injection; (**C**) Static image 4 hours after injection;(**D**) Static image 24 hours after injection in anterior view showing accumulation of the tracer throughout the peritoneum

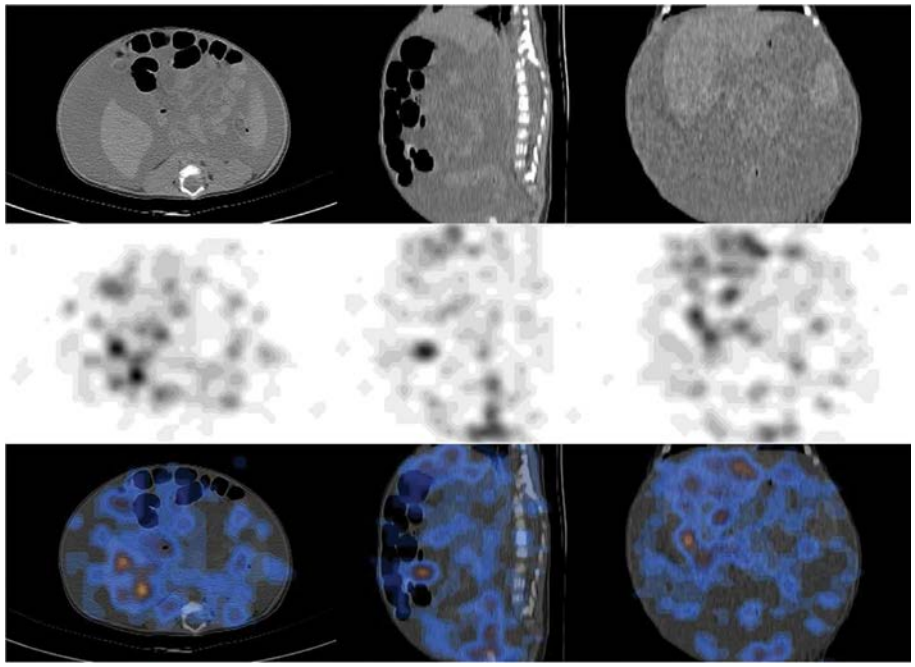

Figure 2. Computed tomography (CT) scan (top row); SPECT images (middle row) and single photon emission computed tomography/computed tomography SPECT/CT images (bottom row) in axial, sagittal, and coronal views confirmed the presence of activity in the peritoneal cavity

Budd-Chiari syndrome. The patient died 12 days after the second explorative laparotomy.

The most probable reason for radiotracer appearance in the ascites fluid on the delayed HBS images was due to oozing of the radiotracer from the liver surface. The present case highlights the usefulness of HBS to narrow the differential diagnosis of ascites of unknown cause in pediatric patients. Delayed imaging is useful in doubtful and challenging cases.

Conflict of interest

The authors declare no conflict of interest.

References

1. Tulchinsky M, Ciak BW, Delbeke D, et al. Society of Nuclear Medicine. SNM practice guideline for hepatobiliary scintigraphy 4.0. J Nucl Med Technol.

2010; 38(4): 210–218, doi: 10.2967/jnmt.110.082289, indexed in Pubmed: 21078782.

2. Snyder ST, Banks KP. Hepatobiliary Scintigraphy. Treasure Island (FL): StatPearls Publishing. 2019(12).
3. Joodi M, Norouzbeigi N, Rad MA, et al. Spontaneous perforation of common bile duct in a pediatric patient: application of hepatobiliary scintigraphy. Clin Nucl Med. 2012; 37(10): 1006–1008, doi: 10.1097/RLU.0b013e318263928f, indexed in Pubmed: 22955078.
4. Sood A, Parihar AS, Thapa BR, et al. Hepatobiliary Scintigraphy Findings Lead to the Diagnosis of Spontaneous Common Bile Duct Rupture in an Infant. Clin Nucl Med. 2017; 42(3): 223–224, doi: 10.1097/RLU.0000000000001509, indexed in Pubmed: 28045732.
5. Vijay BB, Kumar R, Gupta DK, et al. Spontaneous biliary perforation in an infant: an unusual chronic presentation. Clin Nucl Med. 2008; 33(4): 273–275, doi: 10.1097/RLU.0b013e3181662adb, indexed in Pubmed: 18356667.
6. Arun S, Santhosh S, Sood A, et al. Added value of SPECT/CT over planar Tc-99m mebrofenin hepatobiliary scintigraphy in the evaluation of bile leaks. Nucl Med Commun. 2013; 34(5): 459–466, doi: 10.1097/MNM.0b013e3283601098, indexed in Pubmed: 23503002.
7. Huda F, Naithani M, K Singh S, et al. Ascitic Fluid/Serum Bilirubin Ratio as an aid in Preoperative Diagnosis of Choleperitoneum in a Neglected Case of Spontaneous Common Bile Duct Perforation. Euroasian J Hepatogastroenterol. 2017; 7(2): 185–187, doi: 10.5005/jp-journals-10018-1246, indexed in Pubmed: 29201807.
8. Brugge WR, Rosenberg DJ, Alavi A. Diagnosis of postoperative bile leaks. Am J Gastroenterol. 1994; 89(12): 2178–2183, indexed in Pubmed: 7977237.
9. Gupta V. Bile leak detection by radionuclide scintigraphy. Kathmandu Univ Med J (KUMJ). 2006; 4(1): 82–85, indexed in Pubmed: 18603875.
10. Bourgeois, F. John, and John B. Hanks: Color Atlas of Laparoscopy. Annals of Surgery 1984: 330.
11. Tandon K, Dabage N, Rodriguez M. A Crying Liver: Complication of Endoscopic Retrograde Cholangiopancreatography. American Journal of Gastroenterology. 2017; 112: S733, doi: 10.14309/00000434-201710001-01352.

Clinical vignette

Nuclear Medicine Review 2022, 25, 2: 134–135
DOI: 10.5603/NMR.a2022.0029

ISSN 1506–9680, e-ISSN 1644–4345

VIA MEDICA

COVID-19 pneumonia detected by parathyroid scintigraphy

Mehrosadat Alavi[1, 2], Yalda Moafpourian[2]

[1]Ionizing and Non-Ionizing Radiation Protection Research Center (INIRPRC), Shiraz University of Medical Sciences, Shiraz, Iran
[2]Nuclear Medicine Department, Medical School, Shiraz University of Medical Science, Shiraz, Iran

[Received 7 XII 2021; Accepted 27 IV 2022]

Abstract

We report a case of incidental diagnosis of COVID-19 pneumonia by parathyroid scintigraphy. A 53-year-old woman who had severe fatigue, and mild dyspnea underwent parathyroid scintigraphy due to increased serum parathyroid hormone (PTH) and serum calcium levels. Parathyroid scan was negative for abnormal parathyroid tissue. Although the patient had three negative results of COVID-19 PCR tests, significant 99m Tchexakis-2-methoxyisobutylisonitrile ([^{99m}Tc]MIBI) uptake is noticed in both lungs that was suspicious for Covid-19 pneumonia. The patient underwent CT scan of the chest for further evaluation. Diffuse ground-glass opacities were identified in both lungs which were interpreted as typical feature for COVID-19 pneumonia.

KEY words: COVID-19; [^{99m}Tc]MIBI; primary hyperparathyroidism

Nucl Med Rev 2022; 25, 2: 134–135

We report a case of incidental diagnosis of COVID-19 pneumonia by parathyroid scintigraphy. A 53-year-old woman who had severe fatigue, and mild dyspnea underwent parathyroid scintigraphy due to increased serum PTH and serum calcium levels.The parathyroid scan was negative for abnormal parathyroid tissue. Although the patient had three negative results of COVID-19 PCR tests, significant ^{99m}Tc-hexakis-2-methoxyisobutylisonitrile ([^{99m}Tc]MIBI) uptake is noticed in both lungs that were suspicious for Covid-19 pneumonia (Fig. 1, 2) [1, 2]. The patient underwent computed tomography (CT) scan of the chest for further evaluation (Fig. 3) [3–5]. Diffuse ground-glass opacities were identified in both lungs which were interpreted as a typical feature of COVID-19 pneumonia (Fig. 3) [6–8].

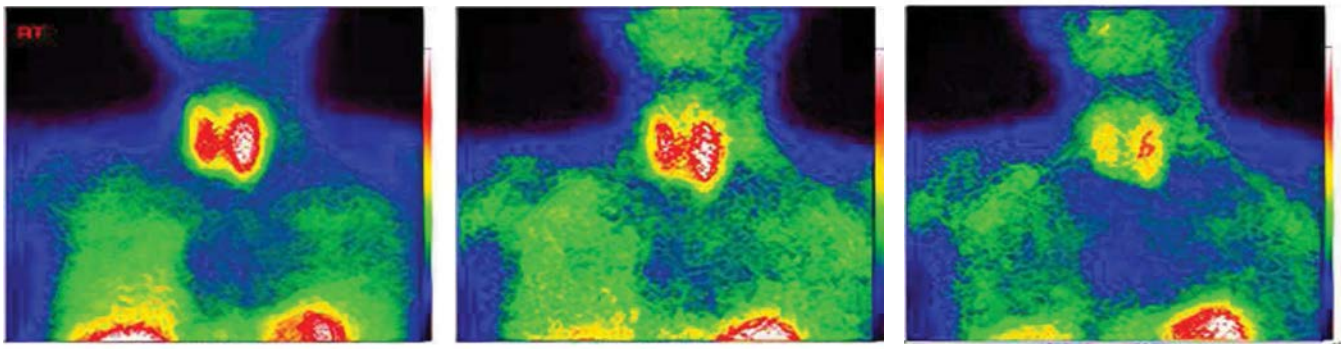

Figure 1. 53-year-old woman was consulted for hyperparathyroidism due to severe fatigue and mild dyspnea. Individuals are more often diagnosed today through routine biochemical laboratory testing done for other purposes [1]. Laboratory assays showed hypercalcemia: 10 mg/dL, high serum level of parathyroid hormone: (80 pmol/L), and normal serum phosphorus level 3 mg/dL. [^{99m}Tc]MIBI parathyroid scintigraphy was performed. ^{99m}Tc-sestamibi assessment has a well-defined clinical role in the surgical management of patients with primary hyperparathyroidism [2]. The scan was negative for abnormal parathyroid tissue. Significant diffuse uptake in both lung fields especially on the right side is noticed incidentally

Correspondence to: Yalda Moafpourian, Nuclear Medicine Department, Medical School, Shiraz University of Medical Science, Shiraz, Iran, e-mail: moafpourian@gmail.com

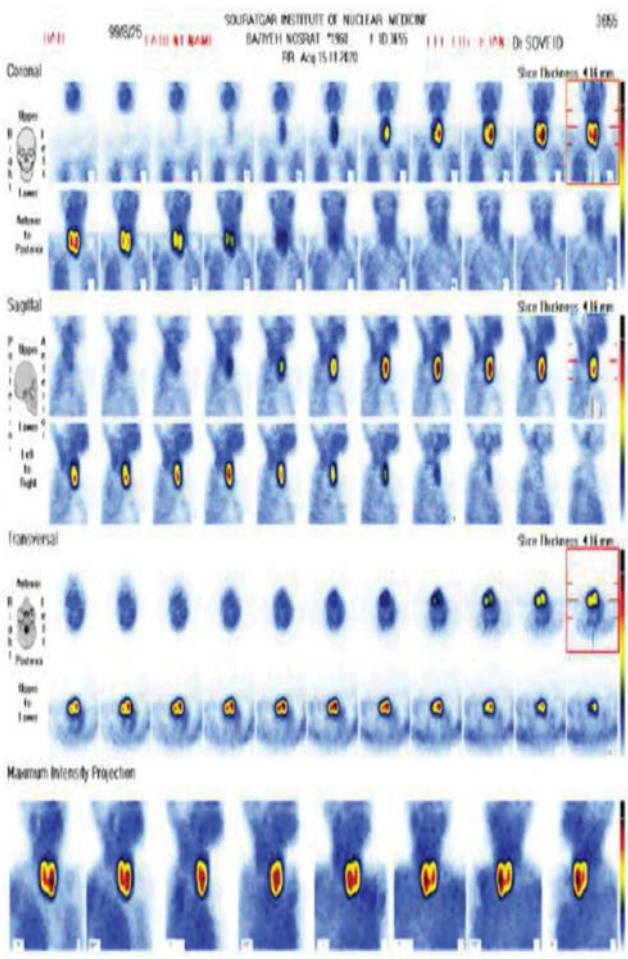

Figure 2. Parathyroid single photon emission computed tomography (SPECT) images, revealed diffuse bilateral lung uptake

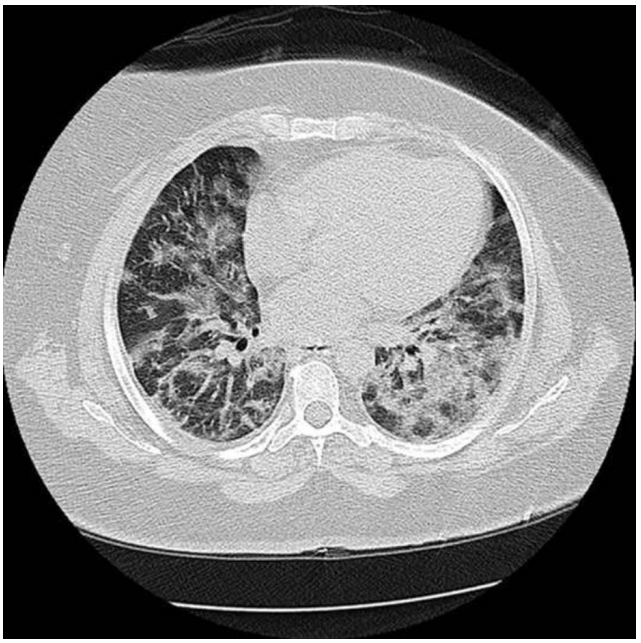

Figure 3. Transaxial computed tomography (CT) scan of the chest. Due to the primary involvement of the respiratory system, chest computed tomography is strongly recommended in suspected COVID-19 cases, for both initial evaluation and follow-up evaluation [3]. Recent studies addressed the importance of chest CT examination in COVID-19 patients with false-negative RT-PCR results [4]. Patients affected by COVID-19 pneumonia usually showed on chest CT some typical features, such as Bilateral ground-glass opacities characterized by multilobe involvement with posterior and peripheral distribution; parenchymal consolidations with or without air bronchogram; interlobular septal thickening; crazy paving pattern, represented by interlobular and intralobular septal thickening surrounded by ground-glass opacities; subsegmental pulmonary vessels enlargement (> 3 mm) [5]. The CT scan in this patient is demonstrating multiple peripherally distributed ground-glass opacities and some other typical features in both lung fields which are in favor of pneumonia induced by COVID-19 [6–8]

Conflict of interest

The authors have no conflicts of interest to declare.

REFERENCES

1. Madkhali T, Alhefdhi A, Chen H, et al. Primary hyperparathyroidism. Ulus Cerrahi Derg. 2016; 32(1): 58–66, doi: 10.5152/UCD.2015.3032, indexed in Pubmed: 26985167.
2. Moralidis E. Radionuclide parathyroid imaging: a concise, updated review. Hell J Nucl Med. 2013; 16(2): 125–133, doi: 10.1967/s002449910083, indexed in Pubmed: 23687643.
3. Jin YH, Cai L, Cheng ZS. A rapid advice guideline for the diagnosis and treatment of 2019 novel coronavirus (2019-nCoV) infected pneumonia (standard version) . Mil Med Res. 2020; 7(1): 4, doi: 10.1186/s40779-020-0233-6 , indexed in Pubmed: 32029004.
4. Xie X, Zhong Z, Zhao W, et al. Chest CT for Typical Coronavirus Disease 2019 (COVID-19) Pneumonia: Relationship to Negative RT-PCR Testing. Radiology. 2020; 296(2): E41–E45, doi: 10.1148/radiol.2020200343, indexed in Pubmed: 32049601.
5. Caruso D, Polidori T, Guido G, et al. Typical and atypical COVID-19 computed tomography findings. World J Clin Cases. 2020; 8(15): 3177–3187, doi: 10.12998/wjcc.v8.i15.3177, indexed in Pubmed: 32874972.
6. Stasiak CE, Cardoso FR, de Almeida SA, et al. Incidental finding of COVID-19 infection after [68Ga]Ga-PSMA-11 PET/CT imaging in a patient with prostate cancer . Eur J Nucl Med Mol Imaging. 2021; 48(2): 653–654, doi: 10.1007/s00259-020-04932-6, indexed in Pubmed: 32710224.
7. Malek H, Maghsudi M, Yaghoobi N. Extra-cardiac multifocal lung uptake of Tc-sestamibi in myocardial perfusion imaging: An asymptomatic case with coronavirus infection features. J Nucl Cardiol. 2020 [Epub ahead of print], doi: 10.1007/s12350-020-02393-w, indexed in Pubmed: 33083980.
8. Albano D, Bertagna F, Bertoli M, et al. Incidental Findings Suggestive of COVID-19 in Asymptomatic Patients Undergoing Nuclear Medicine Procedures in a High-Prevalence Region. J Nucl Med. 2020; 61(5): 632–636, doi: 10.2967/jnumed.120.246256, indexed in Pubmed: 32238429.

Clinical vignette

Nuclear Medicine Review 2022, 25, 2: 136–137
DOI: 10.5603/NMR.a2022.0030

ISSN 1506–9680, e-ISSN 1644–4345

VIA MEDICA

Amino acid extravasation: a rare red flag to keep in mind during peptide receptor radioligand therapy (PRRT) with [^{177}Lu]Lu-DOTATATE

Ghasemali Divband[1], Seyed Hootan Alavi[2], Zohre Adinehpour[3], Forough Kalantari[4], Soroush Zarehparvar Moghadam[5]

[1]Nuclear Medicine Center, Jam Hospital, Tehran, Iran
[2]Department of Surgery, Khatam-al-Anbia Hospital, Tehran, Iran
[3]Khatam PET/CT center, Khatam-al-Anbia Hospital, Tehran, Iran
[4]Department of Nuclear Medicine, Hazrat-e-Rasool General Hospital, Iran University of Medical Sciences, Tehran, Iran
[5]Nuclear Medicine Center, Velayat Hospital, Qazvin University of Medical Sciences, Qazvin, Iran

[Received 11 I 2022; Accepted 27 IV 2022]

Abstract

A 64 years-old woman with intestinal neuroendocrine tumor (NET) and multiple liver metastases was referred for peptide receptor radioligand therapy (PRRT) with [^{177}Lu]Lu-DOTATATE. A few days after the third cycle of PRRT, erythema and swelling in the injection site is occurred which progressed up to one-month post-therapy. The cutaneous lesion was managed by a plastic surgeon with topical treatment. Amino acid extravasation could have devastating effects and should always be considered in patients who underwent PRRT and who receive amino acids for nephroprotection.

KEY words: NET; PRRT; cutaneous; extravasation; [^{177}Lu]Lu-DOTATATE

Nucl Med Rev 2022; 25, 2: 136–137

A 64 years-old woman with intestinal neuroendocrine tumor (NET) and multiple progressive liver metastases underwent 3 cycles of peptide receptor radioligand therapy (PRRT) with [^{177}Lu]Lu-DOTATATE. She had only received long-acting somatostatin analogs before. After two cycles of PRRT, the patient had a stable disease. In the third course of PRRT, 6.3 GBq [^{177}Lu]Lu-DOTATATE was injected thirty minutes after starting the infusion of the amino acid solution (25 g lysine and 25 arginine diluted with 2000 cc normal saline during 6 hours). Like previous treatment courses, a three-way valve catheter was inserted in the right antecubital fossa to administer amino acids and [^{177}Lu]Lu-DOTATATE via the same venous access. The patient did not report any discomfort or side effects; while blood pressure and pulse rate monitoring was performed throughout the treatment period. The -post-therapy whole-body scan was performed after 24 hours using the Siemens Symbia Intevo SPECT/CT dual-head gamma camera with a matrix size of 1024 × 256 and speed of 10 cm/min and showed a primary tumor in the small intestine with intense [^{177}Lu]Lu-DOTATATE uptake as well as several [^{177}Lu]Lu-DOTATATE avid metastases throughout the liver (Fig. 1).

Three days after the therapy the patient felt a burning sensation in the injection site with erythema and tenderness which deteriorates up to one month after PRRT at the time the patient informed us about this problem (Fig. 2). The post-therapy [^{177}Lu]Lu-DOTATATE whole-body scan was reviewed again and only a minimal focus of [^{177}Lu]Lu-DOTATATE extravasation was noted in the right antecubital fossa which could not be the cause of the large skin lesion.

Correspondence to: Soroush Zarehparvar Moghadam, Nuclear Medicine Department, Velayat hospital, Qazvin, Iran
phone: +98 2833792144, e-mail: sorooshzm@gmail.com

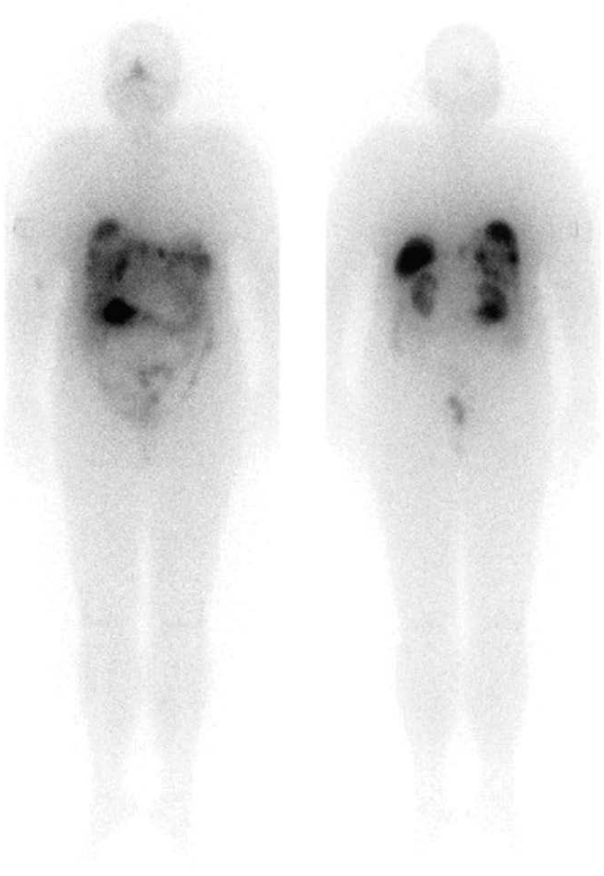

Figure 1. Post therapy whole body [^{177}Lu]Lu-DOTATATE scan performed 24 hours after therapy

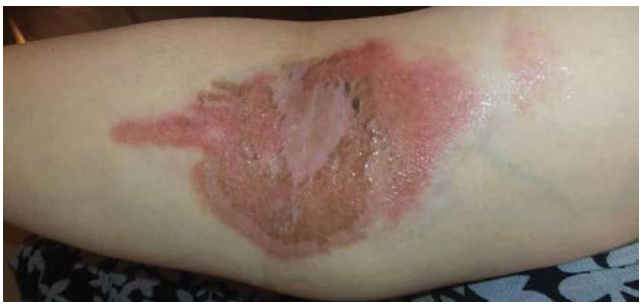

Figure 2. The lesion is an erythematous and erosive plaque with a sharp margin in the anterior cubital fold of the right hand with some degrees of secretion

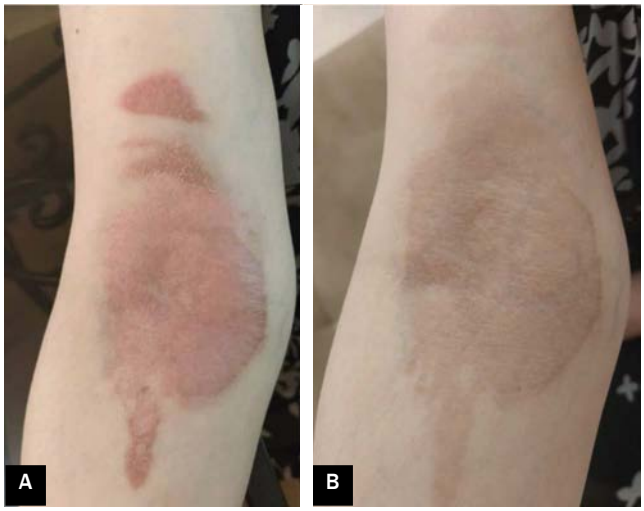

Figure 3. The left picture (**A**) shows the lesion 2 months after PRRT and the right picture (**B**) is 4 months after PRRT which showed near-complete healing of the lesion

The patient was referred to a plastic surgeon and topical therapies were administered and the skin lesion healed within four months (Fig. 3). We concluded that since there was no sign of [^{177}Lu]Lu-DOTATATE extravasation on post-therapy whole-body scan, this side effect is most likely due to the amino acid extravasation. Due to the high osmolarity of the Amino acid solution, its extravasation could cause serious cutaneous damages, even tissue necrosis which may need tissue debridement. This case shows the importance of monitoring the patient during the PRRT course and especially early physical examinations during the course of therapy and in the first week after to evaluate any adverse events that may occur to the patient.

Conflict of interest

The authors declare no conflict of interest.

Letter to Editor

Nuclear Medicine Review 2022, 25, 2: 138–140
DOI: 10.5603/NMR.a2022.0031

ISSN 1506–9680, e-ISSN 1644–4345

VIA MEDICA

A 4.000 € way to improve perceived quality and meet expectations of thyroid cancer patients receiving therapeutic dose of Iodine-131

Evanthia Giannoula[1], Christos Melidis[2, 3], Nikitas Papadopoulos[4], Panagiotis Bamidis[5], Vasilios Raftopoulos[6], Vasiliki Chatzipavlidou[7], Ioannis Iakovou[1]

[1]Nuclear Medicine Department, Academic General Hospital "AHEPA", School of Medicine, Aristotle University of Thessaloniki, Greece
[2]CAP Sante, Radiation Therapy Department, Bastia, France
[3]milliVolt — Radiation Physics, Bastia, France
[4]General Hospital of Thessaloniki "Georgios Gennimatas", Thessaloniki, Greece
[5]Medical Physics Laboratory, School of Medicine, Aristotle University of Thessaloniki, Greece
[6]Division of HIV/AIDS Epidemiological Surveillance, National Public Health Organization (EODY), Athens, Greece
[7]Nuclear Medicine Department, Cancer Hospital of Thessaloniki "Theagenio", Thessaloniki, Greece

[Received 13 XII 2021; Accepted 26 V 2022]

Abstract

Background: Thyroid cancer is the most common malignant disease of the endocrine system and radioiodine therapy (RAIT) is still very often used, resulting in patients staying hospitalized for a few days alone and without visitors, augmenting their stress and discomfort. Our objective was to find simple ways of improving RAIT patients' feelings and perceived quality of the nuclear medicine (NM) department services.

Material and methods: We designed a two-year study in order to enhance RAIT patients' perceived quality of the nuclear medicine (NM) department services and expectations' fulfillment. A questionnaire was used in order to capture patients' perceived quality and expectations from their RAIT.

Results: 549 replies were collected. Many intrinsic and extrinsic determinants were found to be positively or negatively related to the perceived quality and fulfillment of patients' expectations of receiving RAIT. A 1% increase could be achieved by spending 110 € per RAIT room.

Conclusions: In this article, we present some easily implemented changes in both personnel behavior and room amenities that could, at least in theory and based on our results, offer a 37.9% improvement in RAIT patients' perceived quality and expectations' fulfillment at a cost of 4169 €.

KEY words: RAIT; perceived quality; thyroid cancer

Nucl Med Rev 2022; 25, 2: 138–140

Introduction

Thyroid cancer is the most common malignant disease of the endocrine system and one of the few cancers with a rising incidence [1]. Even if treatment protocols evolve, Radioiodine therapy (RAIT) is still used in many cases [2], resulting in patients staying hospitalized for a few days [3] alone and without visitors, due to them being radioactive, augmenting their stress and discomfort [4]. The aim of our study is to capture patients' feelings, perceived quality, and expectations from their RAIT at the Nuclear Medicine (NM) departments and find easy ways to improve them.

Correspondence to: Christos Melidis, CAP Santé, Radiation Therapy Department, 13 Rue Marcel Paul, 20200 Bastia, France and milliVolt.eu, Rue Jean-Mathieu Pekle, 20200 Bastia, France,
phone: 0033 661 54 63 54 and 0032 483 430 260,
e-mail: melichristos@hotmail.com and cmelidis@millivolt.eu

Material and methods

A cross-sectional survey, based on a customized, pre-weighted, and validated questionnaire, as proposed for this type of study [5], has been created and was used on 549 patients over a period of

Table 1. Extrinsic parameters affecting patients' perceived quality and expectations' fulfillment

Personnel related	Provided in depth information	33.3%
	Respect shown	25.1%
	Shown interest in me	17.9%
	Psychological support	17.2%
	Kindness	15.1%
	Human Contact	14.3%
Amenities	Room comforts (internet connection, modern furniture, decoration, etc.)	21.6%
	Quality of food provided	27.1%
All the above		37.9%

two years at both NM departments offering RAIT of Northern Greece. Patients' demographics and cancer (TNM) characteristics were also recorded.

Local Health authorities have given their ethical approval and patients were informed of the survey and its goals and their written approved consent were achieved before filling it in.

Statistical analysis involved the Kolmogorov-Smirnov test, Student's test, χ^2, one-way ANOVA, and Mann-Whitney-Wilcoxon test. IBM SPSS version 26 (IBM Inc., Armonk, NY) was used, and statistical significance was defined at the 95% confidence interval.

Results

Patients' demographics and cancer (TNM) characteristics were found to be in line with data from previous studies on such cohorts [6]. Intrinsic determinants found to be positively related to perceived quality and fulfillment of patients' expectations receiving RAIT are:

— being married or in a relationship versus being divorced ($p = 0.009$),
— being more than 50 years old ($p = 0.017$),
— being of male sex ($p = 0.015$),
— having lower than college/university education ($p = 0.012$),
— being a farmer versus blue-collar ($p = 0.035$) or white-collar ($p = 0.013$),
— having an aggravated TNM stage ($p = 0.043$),
— living in a non-urban environment ($p = 0.041$).

Extrinsic parameters positively determining patients' perceived quality and expectations' fulfillment are:

— being well-informed beforehand about the procedures that will be followed,
— feeling that they are respected,
— being reassured in detail that irradiation is not something to be afraid of and
— feeling that health professionals have a genuine interest in them.

Additionally, patients mentioned that their hospitalization would be much more enjoyable if room service, decoration, facilities, and amenities would be improved. Actually, as can be seen in Table 1, more than a third of the patients would have had a better experience during RAI, if all the above would be true.

Discussion

Intrinsic parameters, given that health should be a commodity accessible to all, are not supposed to be able to be altered, for example by choosing one's patients by age, gender, marital status, etc. However, extrinsic parameters can and should be improved for both personnel and amenities via the:

— Organization of in-house behavior-towards-patients seminars on a periodic basis. These seminars are best to be presented by both health professionals and patient organizations' representatives, since this way patients' needs are not muted, but rather put in conjunction with professionals' experience [7, 8]. These seminars do not need to have an impact on the hospital budget, besides maybe the refreshments offered to participants and the possible traveling expenses of the presenters. If two such seminars are to be organized per year with one presenter flying in and staying one night at a hotel (the most costly scenario), the yearly cost is estimated at 820 €.
— In-depth renovation of facilities. Even in countries where hourly working rates are high, such as the US or UK, a common 9.5 square-meter RAIT room renovation should not cost more than 3.310 € [9], including wall painting, floor and ceiling restoration, simple furniture and decoration emplacement, and internet connection.

Implementing the above improvements in both personnel behavior and room amenities results, at least in theory and based on our results, in a cost of around 110 € per increased percentage of improved perceived quality and expectations' fulfillment. This results in a total cost of 4.169 € for an increase of 37,9%.

Conclusions

To our knowledge, this is the first quantitative proposal on small and inexpensive changes in NM Departments in order to augment positive impressions and feelings of hospitalized thyroid cancer patients undergoing RAIT.

Conflict of interest

The authors have no conflicts of interest to declare.

References

1. Giannoula E, Melidis C, Papadopoulos N, et al. Dynamic Risk Stratification for Predicting Treatment Response in Differentiated Thyroid Cancer. J Clin Med. 2020; 9(9), doi: 10.3390/jcm9092708, indexed in Pubmed: 32825789.
2. Ciarallo A, Rivera J. Radioactive Iodine Therapy in Differentiated Thyroid Cancer: 2020 Update. AJR Am J Roentgenol. 2020; 215(2): 285–291, doi: 10.2214/AJR.19.22626, indexed in Pubmed: 32551904.
3. Borget I, Remy H, Chevalier J, et al. Length and cost of hospital stay of radioiodine ablation in thyroid cancer patients: comparison between preparation with thyroid hormone withdrawal and thyrogen. Eur J Nucl Med Mol Imaging. 2008; 35(8): 1457–1463, doi: 10.1007/s00259-008-0754-9, indexed in Pubmed: 18385999.
4. Banihashem S, Arabzadeh M, Jafarian Bahri RS, et al. Psychological Status and Quality of Life Associated with Radioactive Iodine Treatment of Patients with Differentiated Thyroid Cancer: Results of Hospital Anxiety and Depres-

sion Scale and Short-Form (36) Health Survey. Indian J Nucl Med. 2020; 35(3): 216–221, doi: 10.4103/ijnm.IJNM_14_20, indexed in Pubmed: 33082677.

5. Kaniuka-Jakubowska S, Lewczuk A, Majkowicz M, et al. Nontoxic Goiter (NTG) and Radioiodine: What Do Patients Think About It? Quality of Life in Patients with NTG Before and After 131-I Therapy. Front Endocrinol (Lausanne). 2018; 9: 114, doi: 10.3389/fendo.2018.00114, indexed in Pubmed: 29713309.
6. Giannoula E, Melidis C, Frangos S, et al. Ecological Study on Thyroid Cancer Incidence and Mortality in Association with European Union Member States' Air Pollution. Int J Environ Res Public Health. 2020; 18(1), doi: 10.3390/ijerph18010153, indexed in Pubmed: 33379238.
7. de Lorenzo F, Apostolidis K. The European Cancer Patient Coalition and its central role in connecting stakeholders to advance patient-centric solutions in the mission on cancer. Mol Oncol. 2019; 13(3): 653–666, doi: 10.1002/1878-0261.12448, indexed in Pubmed: 30657631.
8. Melidis C. Possible Impact of a European Agency for the Strategic Management Against Cancer (EASMAC) on Treatment, Diagnosis and EU Politics. Clinics of Oncology. 2020; 03(02), doi: 10.47829/coo.2020.3201.
9. DH Gateway Reviews Estates and Facilities Division. https://www.gov.uk/government/publications/guidance-to-carry-out-cost-estimates-of-healthcare-buildings [Online] (13.12.2021).

VIA MEDICA

Nuclear Medicine Review 2022, 25, 2: 141
DOI: 10.5603/NMR.a2022.0032

ISSN 1506–9680, e-ISSN 1644–4345

Letter to Editor

Multiple benefits of added computed tomography for myocardial perfusion imaging in patients with psoriasis

Joseph C. Lee[1, 2], Alaa Alghamry[2, 3]

[1]Medical Imaging Department, The Prince Charles Hospital, Chermside, Australia
[2]Faculty of Medicine, University of Queensland, Australia
[3]Internal Medicine Services, The Prince Charles Hospital, Chermside, Australia

[Received: 2 XI 20221; Accepted: 30 VI 2022]

KEY words: myocardial perfusion imaging; psoriasis; attenuation correction; computed tomography

We congratulate Sioka et al. [1] for providing an excellent review of the use of single-photon emission computer tomography (SPECT) myocardial perfusion imaging (MPI) in patients with psoriasis. There was quite a little surprise that the images were reconstructed without the assistance of attenuation correction (AC). Low-dose, non-contrast, non-diagnostic computed tomography (CT) can be used for this purpose.

It may have assisted with the diagnosis of myocardial ischaemia, especially in the inferior left ventricular segments, and particularly given that the study ultimately showed no significant difference in the rate of haemodynamically-significant coronary atherosclerosis. It may also assist in identifying coronary artery calcification, which is often used as an anatomical marker for coronary artery stenosis [2]. The prevalence of coronary artery calcification in patients with psoriasis was well studied in a meta-analysis [3].

In addition, psoriasis is associated with many malignancies. A large series specified their respective types [4]. Of these, many would be identified on CT for AC. We found this modality helpful in identifying malignancies (and other significant findings) [5]. This would certainly be relevant for some of the cancers in patients with psoriasis, such as lymphomas, lung cancers, and pancreatic cancers. Thus, CT primarily for AC can contribute significantly to SPECT in patients with psoriasis.

Conflict of interest

No conflicts of interest declared

References

1. Sioka C, Moulias C, Voulgari PV, et al. Single photon emission computed tomography myocardial perfusion imaging in patients with moderate to severe psoriosissis. Nucl Med Rev Cent East Eur. 2021; 24(2): 46–50, doi: 10.5603/NMR.2021.0014, indexed in Pubmed: 34382667.
2. Lee JC, West MJ, Khafagi FA. Myocardial perfusion scans. Aust Fam Physician. 2013; 42(8): 564–567, indexed in Pubmed: 23971065.
3. Kaiser H, Abdulla J, Henningsen KMA, et al. Coronary artery disease assessed by computed tomography in patients with psoriasis: a systematic review and meta-analysis. Dermatology. 2019; 235(6): 478–487, doi: 10.1159/000502138, indexed in Pubmed: 31480039.
4. Chiesa Fuxench ZC, Shin DB, Ogdie Beatty A, et al. The risk of cancer in patients with psoriasis: a population-based cohort study in the health improvement network. JAMA Dermatol. 2016; 152(3): 282–290, doi: 10.1001/jamadermatol.2015.4847, indexed in Pubmed: 26676102.
5. Lee JC, Delaney FT. Prevalence and clinical significance of incidental findings on CT attenuation correction for myocardial perfusion imaging. J Nucl Cardiol. 2021 [Epub ahead of print], doi: 10.1007/s12350-020-02499-1, indexed in Pubmed: 33754302.

Correspondence to: Joseph C. Lee, Medical Imaging Department, The Prince Charles Hospital, 627 Rode Rd, 4032 Chermside, Australia, e-mail: joseph_lee@health.qld.gov.au

Experts' opinion

Nuclear Medicine Review 2022, 25, 2: 142–147
DOI: 10.5603/NMR.a2022.0033

ISSN 1506–9680, e-ISSN 1644–4345

VIA MEDICA

The scintigraphic diagnosis of cardiac amyloidosis. An expert opinion endorsed by the Section of Nuclear Medicine of the Polish Cardiac Society and the Polish Nuclear Medicine Society

Katarzyna Holcman[1, 2], Miroslaw Dziuk[3], Jacek Grzybowski[4], Anna Teresinska[5], Bogdan Malkowski[6], Diana Jedrzejuk[7], Bogna Brockhuis[8], Rafal Czepczynski[9], Lidia Tomkiewicz-Pajak[1], Magdalena Kostkiewicz[1, 2]

[1]Department of Cardiac and Vascular Diseases, Jagiellonian University Medical College, John Paul II Hospital, Krakow, Poland
[2]Department of Nuclear Medicine, John Paul II Hospital, Krakow, Poland
[3]Department of Nuclear Medicine, Military Institute of Medicine, Warsaw, Poland
[4]Department of Cardiomyopathy, National Institute of Cardiology, Warsaw, Poland
[5]Department of Nuclear Medicine, National Institute of Cardiology, Warsaw, Poland
[6]Department of Nuclear Medicine,Nicolaus Copernicus University in Torun, Oncology Center, Bydgoszcz, Poland
[7]Department of Endocrinology, Diabetes and Isotope Therapy, Wroclaw Medical University, Wroclaw, Poland
[8]Department of Nuclear Medicine, Medical University of Gdansk, Gdansk, Poland
[9]Department of Endocrinology, Metabolism and Internal Diseases, Poznan University of Medical Sciences, Poznan, Poland

[Received: 15 V 2022; Accepted: 24 VI 2022]

Abstract

Amyloid transthyretin cardiomyopathy is a progressive disease that confers significant mortality. While it is relatively rare, the frequency of diagnoses has risen with the increased contribution of novel diagnostic approach over the last decade. Traditionally tissue biopsy was considered to be a gold standard for amyloidosis diagnosis. However, there are significant limitations in the wide application of this approach. A noninvasive imaging-based diagnostic algorithm has been substantially developed in recent years. Establishing radionuclide imaging standards may translate into a further enhancement of disease detection and improving prognosis in the group of patients. Therefore we present in the following document current evidence on the scintigraphic diagnosis of cardiac transthyretin amyloidosis. Moreover, we present standardized protocol for the acquisition and interpretation criteria in the scintigraphic evaluation of cardiac amyloidosis.

KEY words: transthyretin amyloidosis; cardiomyopathy; scintigraphy

Nucl Med Rev 2022; 25, 2: 142–147

Transthyretin amyloidosis as an underdiagnosed cause of heart failure

Amyloid cardiomyopathy (CA) is relatively rare, however, the frequency of diagnoses has risen with the increased contribution of novel diagnostic approach over the last decade [1]. There are numerous pathogenic proteins that may cause the disease. Two subtypes account for more than 90% of CA cases — light chain amyloidosis (AL) and transthyretin amyloidosis (ATTR) [2]. Distinguishing between AL and ATTR is critical as these diseases have different pathogenesis and are treated differently by cardiologists (ATTR) and hematologists (AL). Importantly, two main subtypes of ATTR exist wild-type ATTR (wtATTR) and hereditary ATTR (hATTR). In the case of wtATTR, the transthyretin (TTR) protein gradually deposits in form of amyloid fibers over a period of time. In contrast, patients with hATTR are born with a pathologic TTR genetic variant, leading to accelerated amyloid deposition. The mechanism of the disease includes destabilization of the TTR tetramer structure, the misfolded protein then assembles in a highly ordered

Correspondence to: Katarzyna Holcman, John Paul II Hospital, Pradnicka 80, 31-202 Krakow, Poland, phone: +48608214249; e-mail: katarzyna.holcman@gmail.com

fashion to form fibrils that accumulate in the interstitial space. In 70% of ATTR cases, amyloid deposits occur in the heart, leading to the development of CA [3]. For both types of ATTR, the pathomorphological signs include thickened cardiac muscle with alterations of the valves structure, developing as a result of amyloid fibers replacing cardiac tissues. Moreover, common extracardiac sites of involvement and associated manifestations include the kidneys, liver, gastro-intestine tract, tongue, and the nerves of both the autonomous and peripheral nervous systems [4].

The clinical presentation of ATTR CA includes heart failure with preserved ejection fraction (HFpEF), hypertrophic (HCM) ,and restrictive cardiomyopathies (RCM). Despite being considered a rare disease, ATTR amyloidosis may be more prevalent than suspected, particularly in the elderly population. Amyloidosis is often disguised as HCM presenting with increased myocardial thickness, mass, or altered structure of valves. It is essential that cardiologists are aware of this disease because, in most patients, the presentation of the disease is mainly cardiological (HCM/RCM and/or HFpEF). HCM is a complex and relatively common myocardial disorder characterized by primary left ventricular hypertrophy. The guidelines include recommendations for HCM diagnosis, especially the use of bone scintigraphy with 3,3-diphosphono-1,2,-propanodicarboxylic acid (DPD) in patients with symptoms or who have non-invasive test results suggesting ATTR [5]. The degree of heart involvement determines the prognosis of the disease, and thus the earlier it is diagnosed, the better the survival rates for the patients [6].

The history of ATTR CA shows that while it is a rare, progressive disease, it is more common than previously thought. According to recent studies, 13% of hospitalized HFpEF patients had wtATTR [7], 5% of patients diagnosed with HCM had hATTR [8], and 5% of patients with severe low flow aortic stenosis had wtATTR [9]. The prevalence of the disease was also investigated by a population-based study of HFpEF patients and resulted in the diagnosis of ATTR in 7% of patients diagnosed with active isotope screening [10]. Another study revealed that the incidence of wtATTR and hATTR was 155–190 per million and 5 per million, respectively [11]. Until now, all forms of the disease may have been underdiagnosed due to the lack of targeted treatment available, although new therapies that improve survival may change this situation. [12].

In our opinion, it is necessary to further enhance ATTR detection, mainly by raising awareness of the occurrence of the disease. The diagnostic difficulties are a result of the lack of characteristic symptoms in the early phase of the disease that might be called "a great pretender". Symptoms are non-specific, similar to CHF (congestive heart failure). Some factors that serve as clinical guidelines for the diagnosis are referred to as "red flags". The main red flags for wtATTR are cardiological symptoms such as HFpEF, left ventricle hypertrophy, lack of hypertrophy in electrocardiogram (ECG), and cardiac arrhythmias [13]. A vast number of patients present with carpal tunnel syndrome. Most patients suffer from progressive intolerance to standard CHF therapy. Furthermore, there is a disproportion between QRS in ECG and the degree of hypertrophy in echocardiographic examination. Additionally, autonomic nervous system dysfunction appears in the late stage of the disease. To sum up, there should remain a high index of suspicion and diagnostic vigilance during initial diagnosis, patients who present with red flags specific to the disease should be referred for further radioisotope testing. Diagnostic process involves cooperation between cardiologists, hematologists, nephrologists, nuclear medicine specialists, and other specialties. As the nature of the disease is complex, the screening of patients who are genetically burdened or have a family history of amyloidosis is of great significance.

There is significant progress in treatment, as disease-modifying therapies are now available [13]. Tafamidis, a transthyretin stabilizing agent, has been shown to reduce mortality in patients with ATTR cardiomyopathy [12]. The treatment is especially effective if used in the early stage of the disease when the heart has not yet suffered irreversible damage. Hence, early diagnosis is a vital factor. Tafamidis is currently the only drug that has shown efficacy in a randomized trial in patients with ATTR cardiomyopathy, and is recommended in this group of patients in both the hATTR and wtATTR [12, 13]. In selected patients with isolated polyneuropathy tafamidis or gene silencers (patisiran, inotersen) may be considered as treatment options according to current guidelines [13]. Moreover, multiple therapies are currently investigated for ATTR patients [13].

Diagnostic algorithm for ATTR cardiomyopathy

While biomarkers are not included in the diagnostic recommendations, the majority of patients have them checked at the beginning of the diagnostic route. Echocardiography examination is of great importance [13]. Echocardiography may provide incremental information on the current stage of the disease, and show typical lesion associated with CA — increased echogenicity of the heart muscle, thickening of valves and ventricle walls, and impairment of diastolic function [14]. Generally, all echocardiographic abnormalities suggesting cardiac amyloidosis should be the starting point for further research. The most pathognomonic symptom of ATTR visible on echocardiography is the "apical sparing" pattern delivered from the evaluation of the global longitudinal strain (GLS) [15]. Nevertheless, this examination requires high levels of experience. Equally, cardiovascular magnetic resonance imaging (CMR) may be helpful as it enables differentiation between amyloidosis, HCM, and hypertrophy in the course of other diseases [13].

Traditionally tissue biopsy was considered to be a gold standard for amyloidosis diagnosis [16]. However, there are significant limitations in the wide application of this approach — the limited experience of pathologists regarding ATTR, underdiagnoses derived from adipose tissue sampling, the difficulty of immunohistochemical typing, and the low availability of mass spectrometry. In most patients, the presentation of ATTR is including cardiac involvement. Thus, advances in cardiac multimodality imaging were an impetus for the early diagnosis of ATTR. Importantly, there is a new strategy for noninvasive diagnostics [17]. It entails echocardiographic examination, CMR (late gadolinium enhancement, T1-mapping), and radionuclide bone scintigraphy.

Both invasive and non-invasive diagnostic criteria have been proposed. Invasive diagnostic criteria apply to all forms of cardiac amyloidosis, whereas non-invasive criteria are accepted only for ATTR and AL [18]. The distinction is important because testing positive for amyloid deposits does not determine the exact type of cardiac amyloidosis, and hence an array of tests should be performed according to the diagnostic algorithm. In terms of invasive

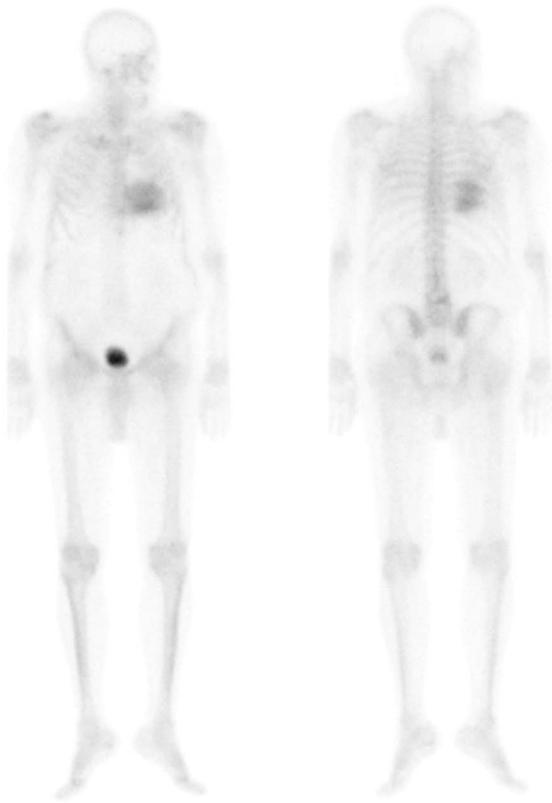

Figure 1. Results of planar whole-body scintigraphy with [^{99m}Tc]Tc-DPD consistent with cardiac amyloidosis (grade 3) in a patient with wtATTR; John Paul II Hospital, Department of Nuclear Medicine, Krakow, Poland

methods, the diagnosis can be confirmed by cardiac biopsy or if amyloid deposits within the tissue from an extracardiac biopsy are accompanied either by the characteristic features of CA by echocardiography or CMR [13]. For the non-invasive methods, ATTR can be confirmed with scintigraphy, serum-free light chain (FLC) assay, serum (SPIE), and urine (UPIE) protein immunofixation. Currently, positive scintigraphy indicates a high probability of ATTR [19]. Regardless, it is always necessary to perform biochemical diagnostics: the evaluation of FLC assay, SPIE and UPIE. Evaluation of those is necessary to differentiate between ATTR (negative results for monoclonal proteins in blood and urine) and AL. However, it is necessary to refer all patients with positive FLC assay, SPIE or UPIE results for hematological evaluation, in order to differentiate MGUS (monoclonal gammopathy of undetermined significance) or AL amyloidosis.

Patients who present with either clinical symptoms or CMR or echocardiography results suggestive of amyloidosis should be referred for scintigraphy with bone-seeking tracers labelled with [^{99m}Tc]Tc. Cardiac scintigraphy with [^{99m}Tc]Tc-PYP (pyrophosphate)/DPD (3.3-diphosphono-1.2-propanodicarboxylic acid)/HMDP (hydroxymethylene diphosphonate) ought to be considered in all patients with unexplained LV hypertrophy, HFpEF, familial amyloid polyneuropathy, family history of amyloidosis and an elderly patient's history of low-grade aortic stenosis. Myocardial imaging with [^{99m}Tc]Tc-PYP/DPD/HMDP is a very sensitive and specific test for the diagnosis of ATTR cardiac involvement and may help in its early detection [13, 18]. Since the uptake of radiotracers is different in normal myocardium and myocardium affected by amyloid, this diagnostic method is highly accurate, especially for ATTR. The Perugini grading scale is a widely recommended method of scoring the tracer uptake (Fig. 1) [20, 21]. Despite the fact that myocardial [^{99m}Tc]Tc-PYP/DPD/HMDP uptake correlates with left ventricle wall thickness and cardiac biomarkers, the visual grading scale has not been shown to be an independent predictor of outcomes [18, 22]. The results scintigraphy test can be assessed according to Perugini grading scale while imaging with [^{99m}Tc]Tc-PYP/DPD/HMDP or heart/contralateral lung (H/CL) uptake ratio for [^{99m}Tc]Tc-PYP, defined as the fraction of heart region of interest (ROI) mean counts to contralateral lung ROI mean counts. Interpretation of the examination may be positive (scale ≥ 2 or H/CL ≥ 1.5 with obligatory SPECT confirmation), neutral (scale 1 with H/CL 1–1.5), or negative (0 with H/L< 1) [18]. In the absence of light chains, heart uptake ≥ 2 eliminates the need for an endomyocardial biopsy and ATTR diagnosis can be confirmed. To distinguish hereditary from wild-type amyloidosis a genetic test should be performed. If there is no cardiac uptake in scintigraphy and monoclonal protein is detected, AL amyloidosis should be ruled out. Otherwise, beyond these two clinical scenarios, an endomyocardial biopsy may be performed for diagnosis confirmation in histopathological tests.

Importantly, pyrophosphate has a high affinity to calcium accumulates in the cells that have been impacted by necrosis. Thus, elevated myocardial tracer uptake can be seen in various conditions of myocardial injury, including pericarditis. Additionally, a regional radiopharmaceutical uptake can be seen in the case of muscle damage induced by commonly used chemotherapy agents, or general drug toxicity, and hence the results might be questionable [18].

It has been shown that [^{123}I]MIBG can detect cardiac denervation in patients with cardiac ATTR amyloidosis [18]. Multiple positron emission tomography (PET) tracers have also been investigated in terms of the possibility of their application in the diagnosis of amyloidosis. Carried studies have confirmed their diagnostic value, although the results are not specific for the type of amyloid [18]. They are not currently recommended to be used in the basic diagnostic algorithm. However, several recent studies suggest a promising role for amyloid PET radiopharmaceuticals to image CA, and several PET tracers are now tested for in vivo detection of amyloid deposits.

Image acquisition and interpretation

Recommendations on the used activities are in line with the guidelines of the American Society of Nuclear Cardiology (ASNC) and the European Association of Nuclear Medicine (EANM) (Tab. 1) [18, 20]. Various activities are recommended by different scientific bodies, with the lowest being 370 MBq and the highest 740 MBq. The guidelines allow that individual centers modify imaging procedures based on local conditions and expertise. The time between injection and acquisition is 2–3 hours, after which a planar whole-body and the SPECT or SPECT/CT is performed (Fig. 2). The specific planar whole-body imaging should be mandatory as it is especially useful for the visual interpretation and quantification of the degree of myocardial uptake. We would like

Table 1. Recommendations for standardized acquisition for scintigraphy with [^{99m}Tc]Tc-PYP/DPD/HMDP for cardiac amyloidosis

Imaging procedures	Recommendation
Preparation	No fasting required
Scan type	Rest scan
Activity of ^{99m}Tc	370–740 MBq (10–20 mCi) intravenously
Time between injection and acquisition: ^{99m}Tc-PYP/DPD/HMDP	2–3 h
Position	Supine
Energy window	140 keV, 15–20%
Collimators	Low energy, high resolution
Whole-body planar imaging	
Views	Anterior (or anterior-and-posterior)
Image duration	Maximum 20 cm per minute
Matrix size	256 × 1024
Planar imaging	
Number of views	Anterior and lateral
Detector configuration	90°
Image duration (count based)	750,000 counts
Matrix size	256 × 256
SPECT imaging	
Angular range/detector configuration	180°/90° or 360°/180°
Number of views/detector	minimum 32
Matrix size	128 × 128
Time per stop	20 s/25 s (may be corrected according to the administered activity)

DPD — 3.3-diphosphono-1.2-propanodicarboxylic acid; h — hour; HMDP — hydroxymethylene diphosphonate; keV — kiloelectronvolt, MBq — megabecquerel; mCi — millicurie; PYP — pyrophosphate; s — second; SPECT — single-photon emission computed tomography

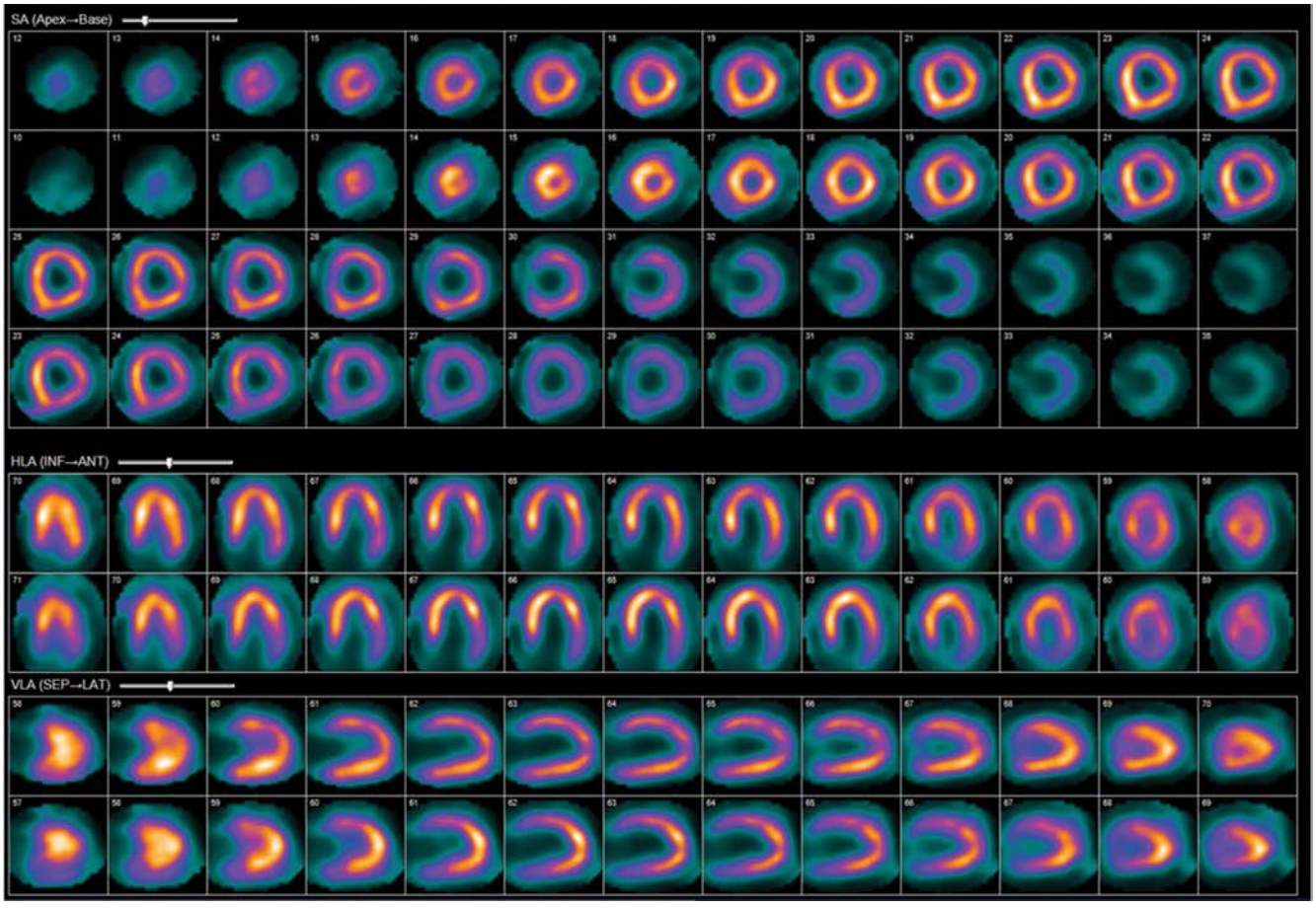

Figure 2. Results of SPECT imaging with [^{99m}Tc]Tc-DPD consistent with cardiac amyloidosis in a patient with hATTR (the upper rows in a given series are shown without attenuation correction, and the lower ones present results after attenuation correction); John Paul II Hospital, Department of Nuclear Medicine, Krakow, Poland

Table 2. Recommendations for interpretation of scintigraphy with [^{99m}Tc]Tc-PYP/DPD/HMDP for cardiac amyloidosis

[^{99m}Tc]Tc-PYP/DPD/HMDP uptake grading	
Grade 0	No myocardial uptake and normal bone uptake
Grade 1	Myocardial uptake less than rib uptake
Grade 2	Myocardial uptake equal to rib uptake
Grade 3	Myocardial uptake greater than rib uptake with mild/absent rib uptake
Heart/contralateral lung (H/CL) uptake ratio (the fraction of heart ROI mean counts to contralateral lung ROI mean counts) assessment for [^{99m}Tc]Tc-PYP	
H/CL ≥ 1.5	Positive (with SPECT confirmation)
H/CL 1–1.5	Neutral
H/L < 1	Negative

DPD — 3.3-diphosphono-1.2-propanodicarboxylic acid; H/CL — heart/contralateral lung; HMDP — hydroxymethylene diphosphonate; ROI — region of interest; SPECT — single-photon emission computed tomography; PYP — pyrophosphate

to stress the importance of including the description of the scintigraphy changes in soft tissues and bone structures while reporting the whole-body and planar images.

The procedure may be performed with the application of the following markers [^{99m}Tc]Tc-PYP/DPD/HMDP. According to the diagnostic algorithm of the nonbiopsy diagnosis of cardiac transthyretin amyloidosis, the results of bone scintigraphy with [^{99m}Tc]Tc-PYP/DPD/HMDP classify patients into 4 grades (0, 1, 2 and 3). The interpretation of the results is shown in Table 2. In patients suspected of CA the grade 2 or 3 [^{99m}Tc]Tc-PYP/DPD/HMDP uptake (in the absence of free immunoglobulin light chains in blood and urine) is highly specific for ATTR and the patient does not require a tissue biopsy to confirm the diagnosis. Importantly, the SPECT or SPECT/ CT scans enable a better assessment of amyloid deposits in cardiac region.

Experience and future directions

Lack of standardized procedure constitutes a barrier to disease detection in local setting. The problem may be solved by implementing the recommendations for performing scintigraphy for amyloidosis, which could be used in both hospitalized patients and during outpatient visits. It is crucial to include planar whole-body and SPECT or SPECT/CT scans, in line with the nuclear imaging guidelines. Another critical action that might positively contribute to accessing scintigraphy is raising awareness among medical professionals of the diagnostic procedures by cooperation between nuclear medics and other specialists. There is a need for cross-departmental cooperation, that would lead to a proper referral for scintigraphy, based on pretest probability assessment, including biomarkers and imaging results. Overall, establishing radionuclide imaging guidelines will translate into further enhancement of disease detection and improving prognosis in the group of patients with suspicion of CA.

Conflict of interest

The authors have no conflicts of interest to disclose.

References

1. Adam RD, Coriu D, Jercan A, et al. Progress and challenges in the treatment of cardiac amyloidosis: a review of the literature. ESC Heart Fail. 2021; 8(4): 2380–2396, doi: 10.1002/ehf2.13443, indexed in Pubmed: 34089308.
2. Yamamoto H, Yokochi T. Transthyretin cardiac amyloidosis: an update on diagnosis and treatment. ESC Heart Fail. 2019; 6(6): 1128–1139, doi: 10.1002/ehf2.12518, indexed in Pubmed: 31553132.
3. Holcman K, Kostkiewicz M, Podolec P, et al. Cardiac amyloidosis — state-of-the-art diagnosis and emerging therapies. Folia Cardiologica. 2019; 14: 616–624.
4. Gawor M, Holcman K, Franaszczyk M, et al. Spectrum of transthyretin gene mutations and clinical characteristics of Polish patients with cardiac transthyretin amyloidosis. Cardiol J. 2020 [Epub ahead of print], doi: 10.5603/CJ.a2020.0104, indexed in Pubmed: 32789836.
5. Elliott PM, Anastasakis A, Borger MA, et al. Authors/Task Force members. 2014 ESC guidelines on diagnosis and management of hypertrophic cardiomyopathy: the task force for the diagnosis and management of hypertrophic cardiomyopathy of the european society of cardiology (ESC). Eur Heart J. 2014; 35(39): 2733–2779, doi: 10.1093/eurheartj/ehu284, indexed in Pubmed: 25173338.
6. Gillmore JD, Damy T, Fontana M, et al. A new staging system for cardiac transthyretin amyloidosis. Eur Heart J. 2018; 39(30): 2799–2806, doi: 10.1093/eurheartj/ehx589, indexed in Pubmed: 29048471.
7. González-López E, Gallego-Delgado M, Guzzo-Merello G, et al. Wild-type transthyretin amyloidosis as a cause of heart failure with preserved ejection fraction. Eur Heart J. 2015; 36(38): 2585–2594, doi: 10.1093/eurheartj/ehv338, indexed in Pubmed: 26224076.
8. Damy T, Costes B, Hagège AA, et al. Prevalence and clinical phenotype of hereditary transthyretin amyloid cardiomyopathy in patients with increased left ventricular wall thickness. Eur Heart J. 2016; 37(23): 1826–1834, doi: 10.1093/eurheartj/ehv583, indexed in Pubmed: 26537620.
9. Treibel TA, Fontana M, Gilbertson JA, et al. Occult transthyretin cardiac amyloid in severe calcific aortic stenosis: prevalence and prognosis in patients undergoing surgical aortic valve replacement. Circ Cardiovasc Imaging. 2016; 9(8), doi: 10.1161/CIRCIMAGING.116.005066, indexed in Pubmed: 27511979.
10. AbouEzzeddine OF, Davies DR, Scott CG, et al. Prevalence of transthyretin amyloid cardiomyopathy in heart failure with preserved ejection fraction. JAMA Cardiol. 2021; 6(11): 1267–1274, doi: 10.1001/jamacardio.2021.3070, indexed in Pubmed: 34431962.
11. Winburn I, Ishii T, Sumikawa T, et al. Estimating the prevalence of transthyretin amyloid cardiomyopathy in a large in-hospital database in japan. Cardiol Ther. 2019; 8(2): 297–316, doi: 10.1007/s40119-019-0142-5, indexed in Pubmed: 31376091.
12. Maurer MS, Schwartz JH, Gundapaneni B, et al. ATTR-ACT Study Investigators. Tafamidis treatment for patients with transthyretin amyloid cardiomyopathy. N Engl J Med. 2018; 379(11): 1007–1016, doi: 10.1056/NEJMoa1805689, indexed in Pubmed: 30145929.
13. Garcia-Pavia P, Rapezzi C, Adler Y, et al. Diagnosis and treatment of cardiac amyloidosis: a position statement of the ESC Working Group on Myocardial and Pericardial Diseases. Eur Heart J. 2021; 42(16): 1554–1568, doi: 10.1093/eurheartj/ehab072, indexed in Pubmed: 33825853.
14. Phelan D, Collier P, Thavendiranathan P, et al. Relative apical sparing of longitudinal strain using two-dimensional speckle-tracking echocardiography is both sensitive and specific for the diagnosis of cardiac amyloidosis. Heart. 2012; 98(19): 1442–1448, doi: 10.1136/heartjnl-2012-302353, indexed in Pubmed: 22865865.
15. Rubiś P, Dziewięcka E, Holcman K, et al. Nowe metody diagnostyki amyloidozy serca. Seria przypadków amyloidozy transtyretynowej. Hematologia. 2018; 9(3): 254–264, doi: 10.5603/hem.2018.0032.

16. Ruberg FL, Berk JL. Transthyretin (TTR) cardiac amyloidosis. Circulation. 2012; 126(10): 1286–1300, doi: 10.1161/CIRCULATIONAHA.111.078915, indexed in Pubmed: 22949539.
17. Kristen AV, Scherer K, Buss S, et al. Noninvasive risk stratification of patients with transthyretin amyloidosis. JACC Cardiovasc Imaging. 2014; 7(5): 502–510, doi: 10.1016/j.jcmg.2014.03.002, indexed in Pubmed: 24726252.
18. Dorbala S, Ando Y, Bokhari S, et al. ASNC/AHA/ASE/EANM/HFSA/ /ISA/SCMR/SNMMI expert consensus recommendations for multimodality imaging in cardiac amyloidosis: Part 1 of 2-evidence base and standardized methods of imaging. J Nucl Cardiol. 2019; 26(6): 2065–2123, doi: 10.1007/s12350-019-01760-6, indexed in Pubmed: 31468376.
19. Gillmore JD, Maurer MS, Falk RH, et al. Nonbiopsy Diagnosis of Cardiac Transthyretin Amyloidosis. Circulation. 2016; 133(24): 2404–2412, doi: 10.1161/CIRCULATIONAHA.116.021612, indexed in Pubmed: 27143678.
20. Dorbala S, Ando Y, Bokhari S, et al. Addendum to ASNC/AHA/ASE/ /EANM/HFSA/ISA/SCMR/SNMMI expert consensus recommendations for multimodality imaging in cardiac amyloidosis: Part 1 of 2-evidence base and standardized methods of imaging. J Nucl Cardiol. 2021; 28(4): 1769–1774, doi: 10.1007/s12350-020-02455-z, indexed in Pubmed: 34196911.
21. Perugini E, Guidalotti PL, Salvi F, et al. Noninvasive etiologic diagnosis of cardiac amyloidosis using 99mTc-3,3-diphosphono-1,2-propanodicarboxylic acid scintigraphy. J Am Coll Cardiol. 2005; 46(6): 1076–1084, doi: 10.1016/j.jacc.2005.05.073, indexed in Pubmed: 16168294.
22. Hutt DF, Fontana M, Burniston M, et al. Prognostic utility of the Perugini grading of 99mTc-DPD scintigraphy in transthyretin (ATTR) amyloidosis and its relationship with skeletal muscle and soft tissue amyloid. Eur Heart J Cardiovasc Imaging. 2017; 18(12): 1344–1350, doi: 10.1093/ehjci/jew325, indexed in Pubmed: 28159995.